Novel Methods for Internal Profiling of Industrial Pipework

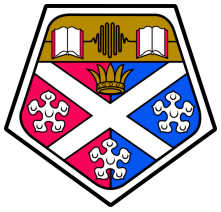

William Jackson

Department of Electronic and Electrical Engineering

University of Strathclyde

A thesis submitted for the degree of

Doctor of Engineering

2021

Copyright

Date:

Signed:

Acknowledgements

Foremost, I would like to thank my supervisors, Gordon Dobie, Charles MacLeod, Cailean Forrester & Fergus Caldwell for their advice, encouragement and continued patience.

My thanks extend to all I have worked with throughout this study, in particular Liam McDonald, Rahul Summan, Dayi Zhang, Graeme West, & Sal Hosseinzadeh. The members of the Centre for Ultrasonic Engineering & Inspectahire™ have made my time as an EngD student both enjoyable and fulfilling. Further thanks go to all members of the MAPS consortium.

I would like to thank Inspectahire™ once again for supporting this EngD via the Research Council for Non-Destructive Evaluation and the Engineering and Physical Sciences Research Council.

Abstract

Integrity of industrial pipework is ensured through routine inspection. Internal visual inspection tools are capable of characterising degradation in the form of corrosion, pitting, erosion and cracking. The outcomes of inspections on pipework have a direct impact on decisions regarding the remaining lifetime of the asset. This thesis considers a pipe-profiling system consisting of a laser-profiler and fisheye camera that produces high-resolution stitched images and point clouds giving geometric information.

The advantage of the system presented include odometry information obtained through visual odometry, a clear unwrapped 360° overview of the pipe interior and accurate 3D information obtained through the laser-profiler. The accuracy of such a laser-profiler is defined by the ability to extract laser projections from an image as it travels down the pipe, and project these extractions to 3D. A novel calibration routine has been established to reduce the error caused by misalignment and tolerances during fabrication of the system. In addition to the study and calibration of the laser-profiler an extensive simulated review of alternative designs, and a study of the profiler in its current configuration was undertaken. This provided insights into its capabilities and range of pipe sizes the system is, and would be capable of inspecting with design adaptations which are also noted. Finally, to make the use of the pipe-profiler and its features accessible to industry a plug and play real-time software interface was created, with live fisheye image unwrapping and stitching, as well as laser overlay and 3D projections, providing a rich feature set for inspection and technology demonstrations.

Contents

List of Figures

List of Tables

List of Acronyms

BBF Best-Bin-First

BRIEF Binary Robust Independent Elementary Features

CCD Charge-Coupled Device

DLL Dynamic Link Library

DoG Difference of Gaussian

FAST Features from Accelerated Segment Test

FOV Field of View

FPS Frames per Second

GigE Gigabit Ethernet

IMU Inertial Measurement Unit

LIDAR Light Detection and Ranging

NDE Non-Destructive Evaluation

NNL National Nuclear Laboratory

ORB Oriented FAST and Rotated BRIEF

PnP Perspective N-Points

rBRIEF Rotation-Aware Binary Robust Independent Elementary Features

RMS Root Mean Square

RVI Remote Visual Inspection

SBA Sparse Bundle Adjustment

SfM Structure from Motion

SIFT Scale-Invariant Feature Transform

SONAR Sound Navigation and Ranging

SURF Speeded-Up Robust Features

TRL Technology Readiness Level

Chapter 1

Introduction

1.1 Industrial Motivation

There is a vast amount of pipework in various industries such as oil & gas, petrochemical, nuclear and pharmaceutical. Inspection of this pipework is regularly carried out to ensure plant safety and efficiency, with various regulations and best practices mandated & advised [1]. Furthermore, the inspection of ageing plants which are reaching the end of their expected lifetime is becoming ever more critical, this is to validate their continued safe operation long beyond their planned service life [2], [3].

Over time pipework in such plants may develop flaws such as corrosion, pitting, cracks and product built up. Cracks can occur within pipework through multiple mechanisms such as stress corrosion cracking, this typically develops around regions of high stress such as the heat affected zone surrounding welds [4]. Cracking can also occur through other mechanisms such as fatigue, fatigue cracks may be initiated through cyclic stresses such as heating and cooling cycles [5]. Corrosion (defined by [6] as, "The spontaneous destruction of metals and alloys caused by chemical, biochemical, and electrochemical interaction between

metals and alloys and the environment.") can occur in different forms, through various mechanisms. These are given in [6]: uniform corrosion, galvanic corrosion, pitting, crevice corrosion, stress corrosion cracking, intergranular corrosion, selective leaching, erosion corrosion, hydrogen damage.

Of these forms of corrosion, pitting is of particular interest as it has been identified as a significant risk in the pipework this project was targeted for. It is extremely localised, resulting in small holes or pits in the surface. Pitting is deemed to be one of the most destructive forms of corrosion, Pitting impacts many steel alloys, aluminium & other metals [7]. This localised corrosion can lead to failure of pipework not only through perforation but can also give rise to stress corrosion cracking [4], [8]. Pitting forms most commonly but is not limited to chloride being present within the pipework [7], [8]. A formal standard for the examination and evaluation of pitting is given in [9].

To locate such defects within pipework Non-Destructive Evaluation (NDE) may be used; a rapid screening technique within the realm of Non-Destructive Evaluation (NDE) which can detect flaws such as these is known as Remote Visual Inspection (RVI). Remote Visual Inspection (RVI) as mentioned is often used as a screening technique providing information only on defects visible from the surface, this is due to its minimal preparation requirements, relatively quick rate of coverage and ease of interpretation. Thus, visual inspection is very suitable for screening for the aforementioned defects which may develop, with the exception that the cracks are surface breaking, i.e. the crack is open and visible from the surface of the sample undergoing RVI.

RVI of pipework is typically conducted with a remote camera either housed within a pan and tilt unit on the end of a push-rod or a robotic crawler, allowing access into challenging/inaccessible environments, examples of typical systems used are shown in Section 2.2.2. However, conventional RVI is limited, the inspection routine often consists of an operator reviewing live footage or a pre-recorded video feed with a narrow field of view. This can lead to a loss of known orientation within the pipework or a requirement for multiple passes to be undertaken. Furthermore, the insertion distance of the camera or probe may not be accurately known due to the use of encoders for measuring this value based on a pulley wheel connected to the umbilical of the RVI system, which are often susceptible to mis-measurements due to slippage. To solve these issues a wide-angle camera and laser profiler probe has been developed. The camera used throughout this project has a field of view of 180° enabling the operator to view the entirety of the pipe from a single central perspective. Visual odometry (Section 2.2) is used to replace or alternatively work in tandem with traditional encoders, ensuring the distance travelled down the pipe is accurately measured. This is essential for accurate repair work or for more detailed inspection of noted problem areas. As traditional monocular inspection only provides a two-dimensional image of a three-dimensional surface, defect sizing can be challenging and subjective. For these reasons a laser-profiler was added, projecting a ring of light onto the pipe surface, allowing the inference of three-dimensional information through known geometry of the probe, enabling defects to be sized in a precise and repeatable manner. On top of the hardware providing these benefits, a bespoke software package has been developed capable of providing both a live view of the unwrapped pipe for a clear view of the internal surface as well as a graph detailing

the three-dimensional information provided by the laser-profiler. The sequential images captured by the probe are also stitched together providing a clear history of the pipework inspected, which can be easily compared with prior inspections as the location is encoded within. These advances in RVI provide a much clearer overview of the pipework under inspection, aiding in decisions made in the lifetime of the assets.

1.2 Aims and Objectives

- To understand the existing technology in industrial use and ongoing state of the art research in academia for the RVI of pipework with a focus on three-dimensional reconstruction.
- To expand on and further develop the existing laser pipe profiling system developed and present optimised parameters for inspection.
- To understand the accuracy of the system and define limits of operation with reference to pipe diameter.
- To provide a robust characterisation and calibration method for said laser pipe profiler.
- To produce a software package capable of operating in real time to enable the use of the laser pipe profiler in industry.

1.3 Thesis Outline

The remainder of the thesis is structured as follows:

- Chapter 2 provides an overview of industrial methods for visual pipe inspection as well as an introduction to the fundamentals of visual inspection. It includes a review of the literature for the ongoing academic effort in increasing the state of the art.
- Chapter 3 introduces a pipe profiling tool developed by a consortium including the author, a simulation framework for evaluating expected errors based on hardware changes and a parameter optimisation for inspection.
- Chapter 4 expands on the pipe profiler from the previous chapter, introducing a method for calibration which includes a hardware approach as well as a software calibration, the results of these calibration methods are shown as an error map against a ground truth scan of a test sample.
- Chapter 5 presents a case study of the pipe profiling tool and introduces a software package for the real time unwrapping and stitching of fish eye images for industrial pipe inspection.
- Chapter 6 concludes the presented work, providing a summary of what has been presented.

1.4 Contributions to Academia and Industry

The main contributions produced during the undertaking of this doctoral degree are as detailed below:

- A significant contribution to the development of a pipe inspection system consisting of a fish eye camera and laser profiler was made. This new system was designed for 50 – 150 mm pipework. It is capable of mapping tens of metres of pipework, providing a stitched image in real time and dimensional information with accuracy of around 0.5 mm within an 80 mm diameter pipe. Along with assistance in many areas of the project the authors main contribution focused on calibration and accuracy validation as the probe progressed from the early prototype to the finalised design.
- An experimental methodology for the alignment of the laser and camera within the probe body. The alignment of the laser is critical to the accuracy of the probe, this process not only gave a way to ensure the correct alignment but gave a clear insight into the errors arising from misalignment.
- Through the work in physically realigning the laser, a software calibration was developed, this allowing correction of misalignments where physical adjustment is not feasible. This would be the case in a sealed probe or to make manufacturing in larger volumes practical.
- A software application was designed for the real time processing of the inspection data captured by the probe, providing a live unwrapped and seamless image of the pipework under inspection in a clear and concise

view, live to the operator. The software began as a collaborative effort, the author assisted with development in the early stages where the software was able to provide a live unwrapped image of the pipework. From this point the author developed new modules to process the laser data in real time and to stitch the unwrapped images together. A further benefit of stitching the images together in real time was that this allowed the location of the probe to be observed through visual odometry.

- One factor which often holds back outputs from academic work is a low Technology Readiness Level (TRL), considerable effort was placed into ensuring the probe, software and tertiary equipment satisfy a grading of level 6. This enabled Inspectahire™ to confidently ship the system to NDE suppliers for external trials.

1.5 Publications Arising from this Thesis

- **W. Jackson**, G. Dobie, C. MacLeod, G. West, C. Mineo and L. McDonald, 'Error Analysis and Calibration for a Novel Pipe Profiling Tool', *IEEE Sensors Journal*, Dec. 2019, ISSN: 1530-437X. DOI: 10.1109/JSEN.2019.2960939.
- S. Hosseinzadeh, **W. Jackson**, D. Zhang, L. McDonald, G. Dobie, G. West and C. MacLeod, 'A novel centralization method for pipe image stitching', *IEEE Sensors Journal*, pp. 1–1, 2020. DOI: 10.1109/JSEN.2020.3031637.
- R. Summan, **W. Jackson**, G. Dobie, C. MacLeod, C. Mineo, G. West, D. Offin, G. Bolton, S. Marshall and A. Lille, 'A Novel Visual Pipework Inspection System', QNDE 2017, Jul. 2017.

Chapter 2

Inspection to NDE & Visual Inspection

2.1 Overview of Non-Destructive Inspection

Non-Destructive Evaluation (NDE) has a major part to play in many sectors and industries throughout the lifetime of components, and structures. NDE is a way to characterise the properties & integrity of a component or structure through methods which do not damage them, enabling the health of the components under inspection to be determined in a non-detrimental manner. Defects within components vary depending on the component and environment it is located in, common defects to find are cracks, corrosion, pitting, and other anomalies which may be evident. Through the use of NDE the structural integrity of structures and components can be understood. For instance, aircraft wings which are both a high value component and are safety critical will be assessed at the factory and furthermore, multiple times throughout their life to ensure there are no flaws present or developing throughout its use.

There are many different NDE techniques available, each suited to the inspection of different geometries and scales. They also differ in the underlying physical phenomenon and rely on making the choice specific to the type of material you are inspecting as well as the type of defect you may be expecting to find. A way to broadly categorise inspection techniques would be to place them into two categories; volumetric and surface/near-surface. Volumetric techniques which allow for the interrogation of the interior geometry of the component include ultrasonic testing and radiography. Surface and near surface techniques include techniques such as visual inspection, eddy current testing, magnetic particle inspection. Visual inspection is one of the most abundant forms of NDE [10], [11] as in its most accessible manner it includes simply looking, often with the aid of telescopic devices over structures and components in a controlled manner to ensure there are no visible defects. One drawback however of visual inspection is that as a surface inspection technique, it is only capable of detecting defects at the surface. This is offset in some cases by the fact that in the case of erosion/-corrosion you may see the build-up of surface product & discolouration of the material which might show signs of deeper problems, which could be revisited for a more in-depth localised inspection with supplemental techniques. There are strong benefits to visual inspection, such as the accessibility and speed of the process, these factors make for an excellent screening technique to implement before considering alternative techniques perhaps for detailed investigations of areas of concern. These areas could then be inspected in isolation with techniques which provide more detailed information, such as volumetric results, through for example, ultrasound. This may however, require significant surface preparation, expertise and direct access. The next step in progressing visual inspection from

the human eye would be to take photographs of observed defects or lack of defects to create a historical record and ability to provide concise reports on the condition of the object under inspection. Remote Visual Inspection (RVI) is used when there are access restrictions or risks to health such as radiation exposure, there are also financial benefits including the lack of erection of scaffolding, the need for rope or confined space access.

2.2 Visual Inspection

2.2.1 Introduction

Visual inspection can be broken down into two main categories direct access and Remote Visual Inspection (RVI). Direct access visual inspection can be performed where there is a clear line of sight to all areas of the component which need to be inspected. RVI is used in the case where direct access is not practical due to access requirements, this may be due to multiple factors such as height, size or environmental exposure.

2.2.2 Visual Inspection of Pipework

RVI is particularly well suited to the inspection of pipework, as direct access is often restricted due to the bore size and environmental dangers which may be present.

Pipework is utilised across many sectors to transport many different products & materials across site, whether it be for cooling, process or waste removal. This pipework may develop various defects throughout its lifetime, caused by effects such as environmental exposure and accelerated corrosion due to being located in harsh environments such as the splash zone of an oil rig where aerated seawater continuously causes soaking and drying cycles. Erosion corrosion may occur due to the flow of the product through the pipework which is most likely to be found at bends or sections of changing diameter. Cracks may form at zones of concentrated stress such as the heat affected zone around welds. Another less general form of corrosion may also form - pitting; this localised form of galvanic corrosion is caused by a chemical reaction with the product and commonly occurs in stainless steels, nickel alloys, and aluminium alloys.

The main factor in determining the type of RVI used for the inspection of pipework is the diameter of the pipe under inspection, smaller pipes typically less than 50 mm videoscopes may typically be used. In the range of 50 to 150 mm pipes push rod cameras and small robotic crawlers tend to be utilised. Above this size pipe crawlers or bespoke systems may be utilised.

This information is summarised in Table 2.1.

Furthermore, this section will show the standard and most common forms of RVI in use. It is noted more advanced visual inspection techniques and commercial solutions will be presented later on (Section 2.4) and that the products shown here give an overview of what is available on the market by established companies and more options of a similar level and performance are available for general RVI.

Table 2.1: *Viability of RVI techniques with respect to dimensions of pipe diameters*

	Diameter		
Technique	Small (< 50 mm)	Medium (50–250 mm)	Large (> 250 mm)
Videoscope	Yes	Limited	No
Push-rod Camera	Limited	Yes	Limited
Crawler	Limited	Yes	Yes
In-Line Inspection	No	Limited	Yes

2.2.2.1 Overview of System Used by the Author

The probe used throughout is designed to operate in pipework between 50–150 mm in diameter, deployed by push rod or flexible cable as shown in Figure 2.1. A close up of the probe body detailing the location of the various system components is shown in Figure 2.2 and a technical drawing in Figure 2.3.

The probe uses a fisheye camera to capture the full 360° of the internal bore of the pipework under inspection. It alternates between two modes an LED illuminated image providing visual information of the surface condition and an image taken with a laser ring projected onto the pipe, providing geometric readings.

A detailed overview of the hardware and operation of the system can be found in Section 3.1.1.

Figure 2.1: *Probe alongside push-rod deployment reel and flexible cable*

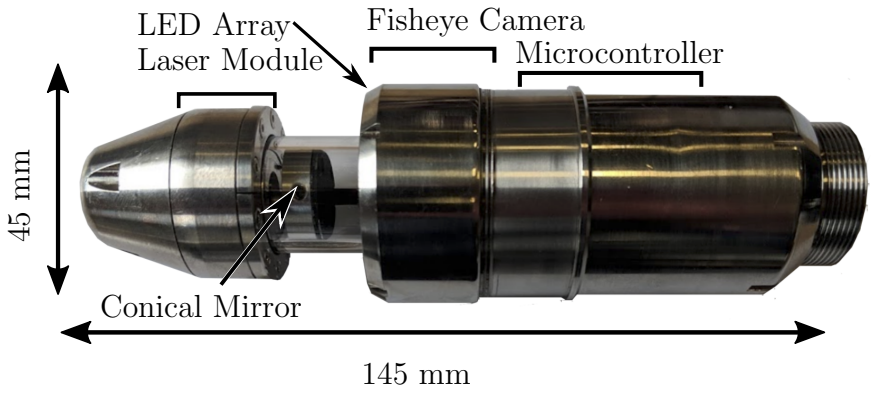

Figure 2.2: *Camera and laser profiler with subsystems highlighted*

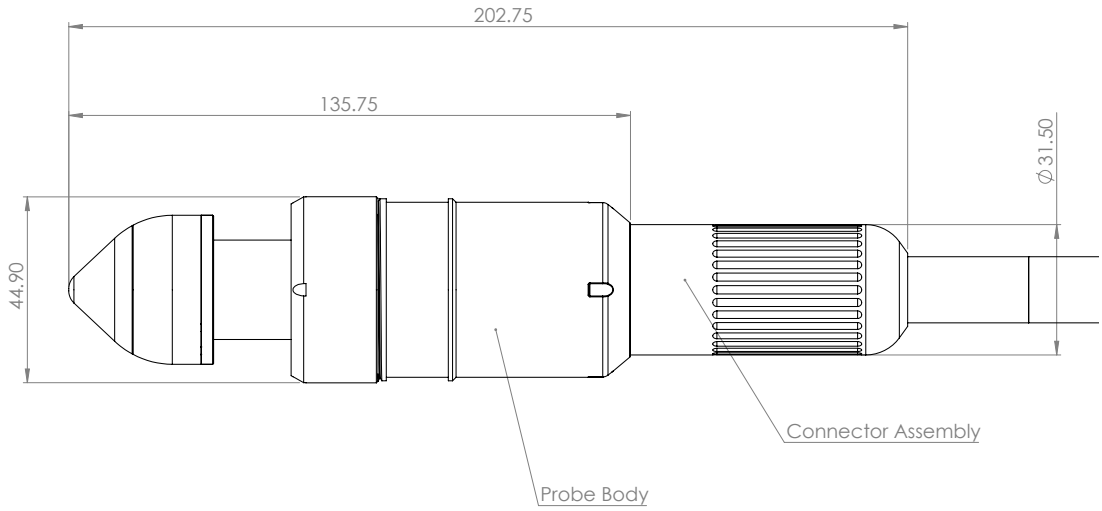

Figure 2.3: *Technical drawing of the camera and laser profiler*

2.2.2.2 Small Bore Pipes

One of the most common industrial uses for pipework below 50 mm in diameter is heat exchangers which are a critical part of many operations such as infrastructure within power plants. Due to their small size they are most suited to inspection using videoprobes, this specialised inspection equipment is capable of inspecting pipes/tube down to a diameter of 2.4 mm [12]. The two main leaders within the market space for these videoprobes are Olympus[1] and Waygate Technologies (formerly GE) a Baker Hughes Company[2]. An example of the Olympus offering is shown in Figure 2.4 The videoprobes offer deployment lengths of up to around 30 m and are equipped with an articulating head to enable the operator to position the lens to capture the region of interest with a range of movement

[1]Olympus https://www.olympus-ims.com/

[2]Baker Hughes https://www.bakerhughesds.com/inspection-ndt/remote-visual-inspection/video-borescopes/

around 130–180° [1,2]. A wide range of lenses are also available, these offer a variable field of view generally between 50–120° (the viewing angle given by the lens, see Section 2.3.1) in either forward facing or side facing options. Additionally, stereo lenses may be equipped, these provide the capability to size areas of interest accurately directly from the image as two views of the scene are captured and processed (see Section 2.3.5.1). In recent years both companies have introduced 3D imaging capabilities for a static scene within the pipe under inspection allowing the creation of a profile detailing the topography of the sample (an example of this is also detailed in Figure 2.4). The resolution of these systems is improving year on year, with hand-held units providing an image size of 756 x 576 pixels and the flagship offerings increasing to 1024 x 768 pixels.

Figure 2.4: *Olympus IPLEX NX videoprobe* [1]

2.2.2.3 Medium Bore Pipes

Medium bore pipework in the size range of 50–150 mm opens up the possibility of various different inspection systems, the videoscopes mentioned for the sub 50 mm previously may still be utilised but it is likely that to obtain useful footage the use of a centralising device may be required to keep the probe central within the pipe under inspection as to maintain the ability to inspect the entirety of the pipe's inner circumference as opposed to the bottom section. The size range opens up the use of pushrod cameras (as shown in Figure 2.5), they are similar in operation to a videoscope but on a larger scale. They often feature pan and tilt capabilities allowing for full coverage of the pipe work under inspection. An increased inspection range is offered with Pearpoint's P540c offering up to deployment lengths of 150 m with a resolution of 765 x 582 pixels[3]. An example pushrod camera reel is shown in Figure 2.5.

The increase in diameter also opens up the inspection to the use of robotic crawlers. Using robotic crawlers allows for the inspection of more complex pipe networks, pushrod cameras become increasingly difficult to insert down long distances of pipes with any moderate bends.

Inuktun, an EddyFi brand, offers a family suited to a wide range of pipe diameters; the Veratrax 50, 100, and 150[4]. They are paired with their offering of cameras the Onyx which is 25.4 mm in diameter and designed to be a slim unit for navigating small pipes with a resolution of 1080 x 720 pixels. They also have

[3]Pearpoint https://www.pearpoint.com/en/products/commercial-video-inspection/flexiprobe-p540c-pushrod-inspection-systems

Figure 2.5: *Pearpoint P540c Reel* [3]

the Spectrum rage of cameras which provide pan and tilt capabilities; they are named after the diameter of the camera body in mm, the Spectrum 45, 90 and 120 HD. Likewise they all offer a varying amount of resolution ranging from the 45 at 420 × 576 pixels to the 120HD at 1920 x 1080 pixels. Inversely the maximum deployment length decreases as resolution increases the Spectrum 45 offers up to a 500 m tether whereas the Spectrum 120HD peaks at a deployment distance of 300 m however, they do offer a long-range fibre optic tether taking this range up to 1000 m[4].

Each of these crawlers are rated for different cameras and deployment lengths, the Veratrax 50 is suitable for up to 100 m of deployment and can be equipped with the Onlyx or Spectrum 45 camera heads. The Veratrax 100 is capable of

300 m lengths of deployment and can utilise the Spectrum 45 of 90. The largest Veratrax the 150 supports deployments of up to 1000 m through the use of the fibre tether and can be paired with the Spectrum 90 or 120HD.

The Veratrax 100 and 150[4] can be deployed in two fashions inline or tractor, in inline deployment the two tracks are one in-front of the other and in tractor they are parallel to each other. It is noted that only in the inline deployment method that they are suitable for this size of pipework. Images of inline and parallel form are shown in Figure 2.6.

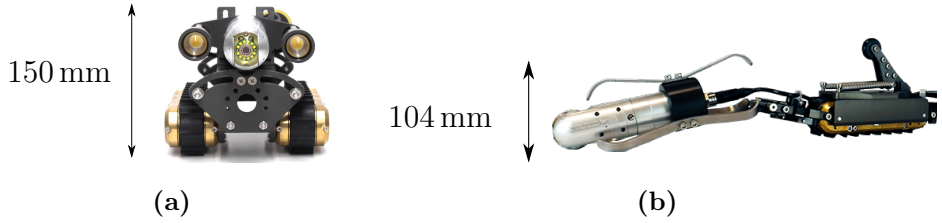

Figure 2.6: *Veratrax 100 in inline (a) and parallel (b) deployment modes*[4]

2.2.2.4 Large Bore Pipes

The inspection of pipes greater than and 150 mm and less than 2000 mm will be considered in this section. Within the oil and gas industry these pipes may be called mainlines used to transfer vast quantities of product large distances over remote areas. A common means of inspection for these pipelines, due to the large distances they span is the use of in-line inspection systems. These are large units containing an array of different sensors. Mechanical features are often added to the design such as flanges to clean the pipe as they pass through,

[4]Inuktun https://www.eddyfi.com/en/product/versatrax-100-pipe-inspection-crawler

they are propelled through the pipeline by the product over great distances with NKKs ultrasonic in-line inspection system setting a world record of 1055 km in 1977 [13]. It is worth noting often visual inspection is often not possible with this technique due to the product still flowing through the pipeline. An example inline inspection tool developed by NDT Global[5] is shown in Figure 2.7

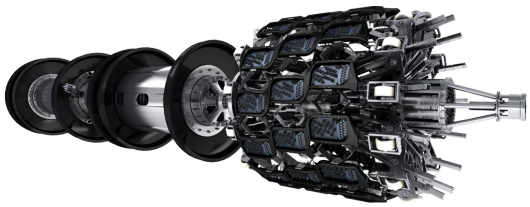

Figure 2.7: *Example ultrasonic in-line inspection system* [5]

In this size range the larger crawlers developed by Inuktun may deployed in the parallel mode offering a greater degree of control and navigation. Furthermore, they offer a configuration allowing the camera to be controlled independently of the tracks ensure centralisation and the optimal position for full coverage of the pipework as shown in Figure 2.8. As well as a vertical pipework version of the same model.

[5]NDT Global https://www.ndt-global.com/about/robots/multi-diameter-tool

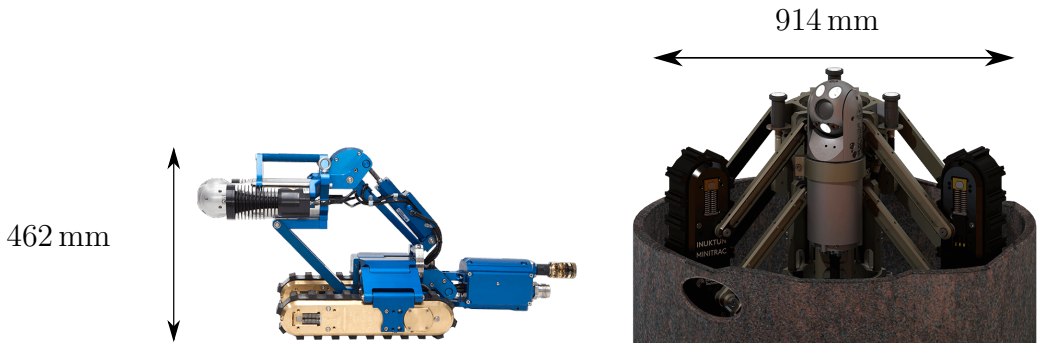

(a) **(b)**

Figure 2.8: *Veratrax 150 in parallel mode (a) and the VT150 vertical crawler (b)*[4]

Along with the wider array of robotic crawlers that these large sizes open up comes bespoke pipe inspection products such as that developed by Inspectahire™shown in Figure 2.9. It is designed to be lowered into vertical pipes such as caissons and offers visual, ultrasonic and/or pulsed eddy current data to the inspector.

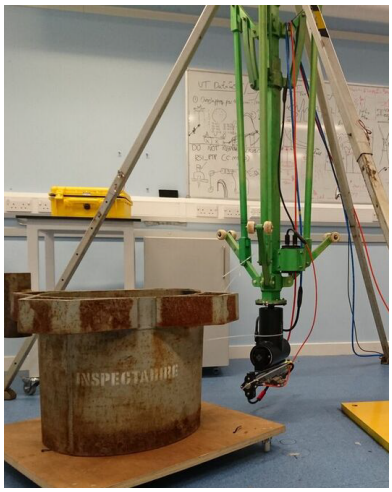

Figure 2.9: *Inspectahire caisson inspection platform, fitted with a camera and either an ultrasonic or pulsed eddy current payload*

2.2.3 Visual Inspection Summary

This section has provided an overview of the different inspection tools available to provide basic visual inspection within a range of pipe sizes. In terms of providing visual inspection for the smallest range of pipes up to 50 mm this generally requires the use of videoscopes especially if that pipework contains any significant bends, as many of the alternative solutions are much larger. In the mid-size range of 50–150 mm more options become available to be deployed, the use of videoscopes still remains a viable option with the use of a centralising device but standard pushrod cameras become available, additionally small robotic crawlers may be used to navigate more complex pipe networks. Finally, in the pipes ranging from 150–2000 mm diameter, can often be inspected in wide-ranging ways, from in-line inspection system which may carry multiple sensing modalities capable of spanning vast distances of pipework, to pushrod cameras and larger crawlers.

2.3 3D Reconstruction in Remote Visual Inspection

In this section the fundamentals building blocks of 3D Reconstruction will be covered, the camera models for both the pin hole and fisheye camera will be given. An overview of the methods available to obtain a three-dimensional model will be presented and finally the academic research projects and commercial offerings are introduced.

A large amount of this section is provided for context for the reader and is not revisited beyond this chapter. The key concepts however are as follows:

- The omnidirectional camera model used throughout: Section 2.3.1.2.
- The camera calibration to obtain the parameters of the camera model: Section 2.3.1.3.
- A brief description of active stereo for 3D reconstruction: Section 2.3.5.2.
- Visual odometry provides a description of how the pose of the probe can be determined through pipework under inspection: Section 2.3.5.5.
- Feature extraction with a focus on the Scale-Invariant Feature Transform (SIFT) algorithm used extensively in this work: Section 2.3.6.

2.3.1 Camera Models

Camera models underpin the ability to create accurate reconstructions, simulations of the camera and the ability to project points into 3D space from the 2D image and vice versa.

2.3.1.1 Pin Hole Camera Model

This model describes the majority of camera and lens combinations that can be described accurately with the pin hole camera model.

Throughout this work in practical examples the pin hole model is not used, only that of Scaramuzza's model detailed in the following section is utilised. This section is given to provide an overview of the concepts of imaging & to give a basis of understanding the more complex omnidirectional model given by Scaramuzza.

The pin hole model describes the way a 3D scene will be imaged onto a 2D plane, as shown by the diagram in Figure 2.10.

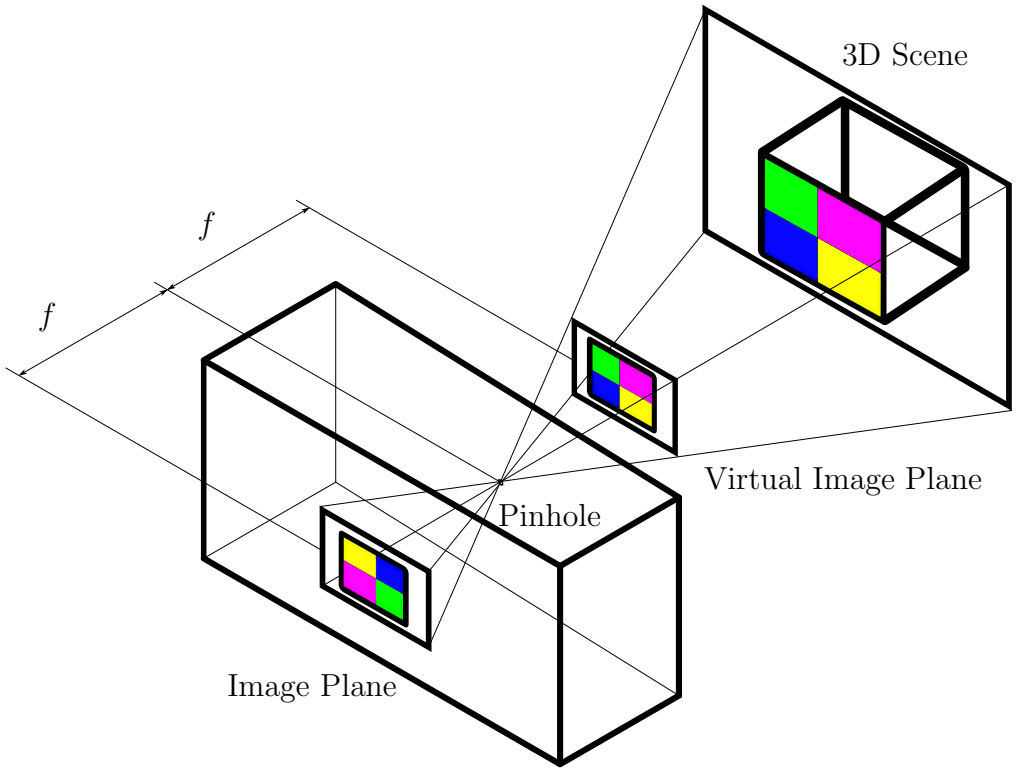

Figure 2.10: *Graphic illustrating the projection of a cube in 3D-space onto the image plane of a pinhole camera*

This can be shown in as detailed by Hartley and Zisserman [14] in Figure 2.11, they go on to describe the mapping of point $\mathbf{X} = (\mathrm{X}, \mathrm{Y}, \mathrm{Z})^{\mathrm{T}}$ onto point $\mathbf{x}$ on the image plane (where the plane is located at a distance of f, along the prin-

cipal axis (notated as the Virtual Image plane in Figure 2.10)). Detailing that through similar triangles it is observed point (X, Y, Z)$^{\mathrm{T}}$ is mapped to the point $(f\mathrm{X}/Z, f\mathrm{Y}/\mathrm{Z}, f)^{\mathrm{T}}$. This can be expressed as a matrix multiplication:

$$\begin{pmatrix} \mathbf{X} \\ \mathbf{Y} \\ \mathbf{Z} \\ 1 \end{pmatrix} \mapsto \begin{pmatrix} f\mathbf{X} \\ f\mathbf{Y} \\ \mathbf{Z} \end{pmatrix} = \begin{bmatrix} f & & & 0 \\ & f & & 0 \\ & & 1 & 0 \end{bmatrix} \begin{pmatrix} \mathbf{X} \\ \mathbf{Y} \\ \mathbf{Z} \\ 1 \end{pmatrix} \tag{2.1}$$

This matrix is further defined as being composed of the diagonal $(f, f, 1)[\mathbf{I}|0]$ creating the 3x4 homogeneous camera projection matrix donated by $\mathbf{P}$. Resulting in the short form notation $\mathbf{x} = \mathbf{PX}$

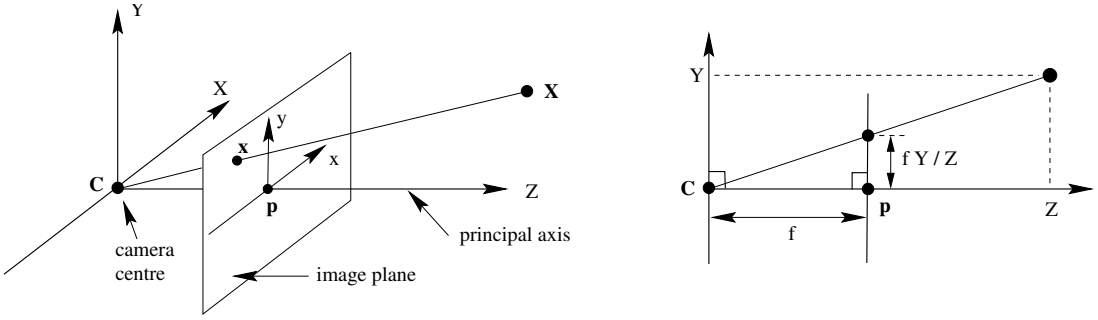

Figure 2.11: *Pinhole camera geometry.* **C** *is the camera centre and* **p** *the principal point. The camera centre is here placed at the coordinate origin. Note the image plane is placed in front of the camera centre [14]*

The perfect pinhole camera transformation has been shown, however this does not capture all of the parameters observed with a camera used practically. These additional parameters are given in the camera calibration matrix **K**:

$$K = \begin{bmatrix} f & & p_x \\ & f & p_y \\ & & 1 \end{bmatrix} \tag{2.2}$$

The parameters are as follows:

Focal length: f

The focal length of the camera is the distance between the image plane and the pinhole measured in pixels. This is shown as by f in Figure 2.10. A greater focal length will result in a reduced field of view and a smaller focal length will result in a greater field of view. This is shown in Figure 2.12. The field of view is calculated as follows where α represents the horizontal field of view assuming the focal length (f) and sensor height (h) are both measured in pixels.

$$\alpha_h = 2 \arctan \frac{h}{2f} \tag{2.3}$$

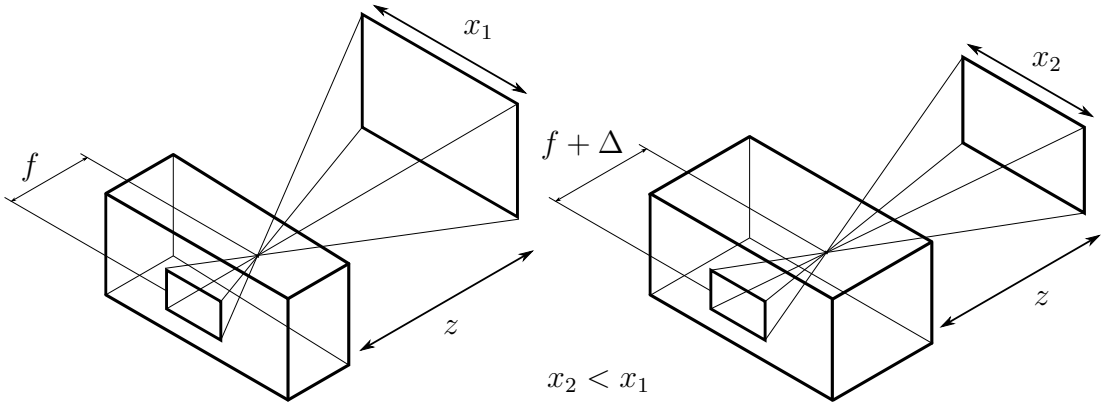

Figure 2.12: *Graphic detailing the effect of increasing the focal length*

Principal Point Offset: p_x, p_y

The principal point is defined as the point where the principal axis which is the line which passes through the pinhole perpendicularly to the image plane intersects the image plane. The offset describes the distance from the origin of the image plane to the intersection point. This may occur due to misalignments of the imaging elements, an example of this is shown in Figure 2.13 as well as the principal point and principal axis or principal ray.

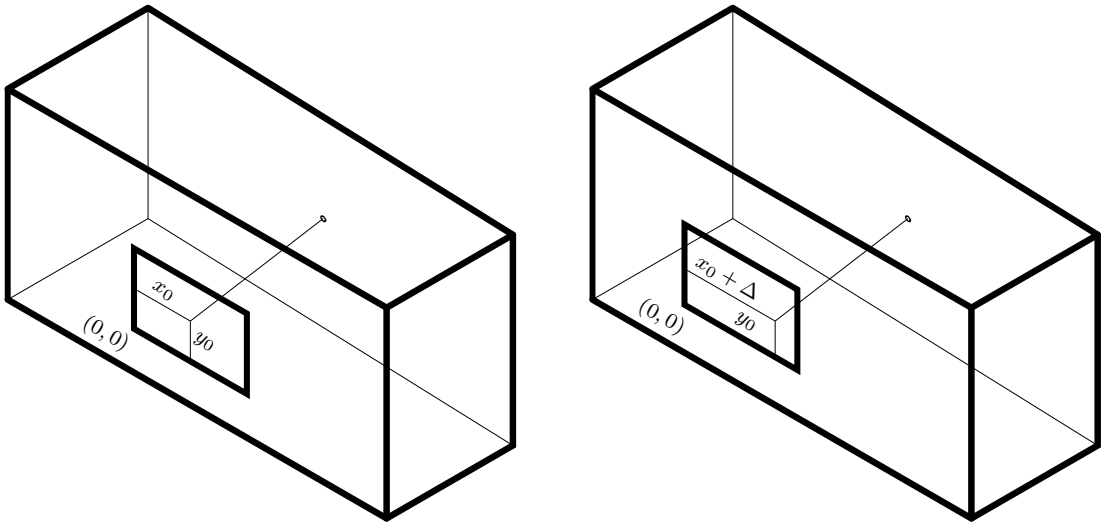

Figure 2.13: *Graphic detailing the principal point*

CCD Cameras

In the case of a Charge-Coupled Device (CCD) camera the pixels may not be square, therefore the scale in the x and y axial directions will no longer be equal. If the number of pixels per unit distance are defined as m_x and m_y in the x and y directions the scaling due to pixels aspect ratio can be incorporated into the transform from world to pixel coordinates by multiplying (2.2) by an extra factor diag. $(m_x, m_y, 1)$. Giving the resulting calibration matrix for the camera:

$$K = \begin{bmatrix} \alpha_x & s & x_0 \\ & \alpha_y & y_0 \\ & & 1 \end{bmatrix} \tag{2.4}$$

Where $\alpha_x = fm_x$ and $\alpha_y = fm_y$ in the x and y directions, likewise the principal point becomes $x_0 = m_x p_x$ & $y_0 = m_y p_y$. The additional component introduced, s is a shear distortion on the projected image. This is represented in Figure 2.14 and the value of s is calculated as follows in Equation (2.5).

$$s = \alpha_x \tan\theta \tag{2.5}$$

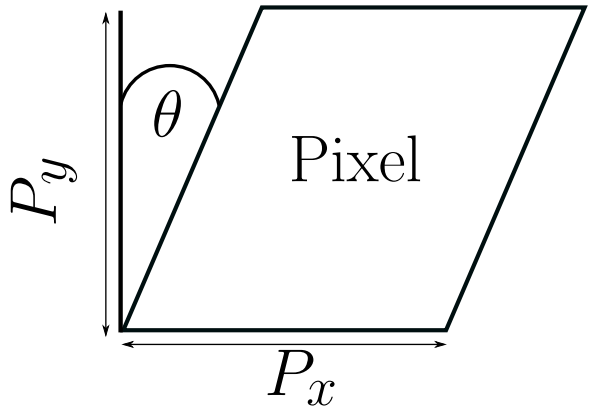

Figure 2.14: *Graphic detailing skew*

The intrinsic matrix describes how 3D points are projected onto the 2D image plane but it does not represent the relation between the points and the camera in 3D space, this information is contained within the extrinsic matrix which is detailed in the following.

$$\mathbf{K} = \begin{bmatrix} \alpha_x & s & x_0 \\ 0 & \alpha_y & y_0 \\ 0 & 0 & 1 \end{bmatrix} \tag{2.6}$$

3D points in space can then be described on the image plane the following Equation (2.7):

$$\mathbf{x} = \mathbf{K}\,[\mathbf{I}|0]\,\mathbf{X}_{\text{cam}} \tag{2.7}$$

The 3D point to be transformed to the 2D imaging plane ($\mathbf{X}_{\text{cam}}$), (X, Y, Z, 1)$^{\text{T}}$ is given in camera coordinates, where the camera is assumed to be at the origin of a Euclidean coordinate system with the principal axis of the camera pointing down the Z-Axis of said coordinate system.

However, it may be practical to define the points in space with respect to a world coordinate frame as opposed to the camera. The camera coordinate frame and world coordinate frame can be related via a rotation and translation. As described by Hartley [14] if X is a 3-vector representing a point in space relative to the world coordinate frame and $\widetilde{\mathbf{X}}_{\text{cam}}$ represents the point relative to the camera coordinate frame: $\widetilde{\mathbf{X}}_{\text{cam}}$ can be found by $\widetilde{\mathbf{X}}_{\text{cam}} = \mathbf{R}(\widetilde{\mathbf{X}} - \widetilde{\mathbf{C}})$, where C represents the camera centre in relation to the world coordinate frame and R is a 3x3 rotation matrix describing the orientation of the camera coordinate frame. Therefore, in combination with (2.3) the point on the image plane can be given as:

$$\mathbf{x} = \mathbf{KR}[\mathbf{I}| - \widetilde{\mathbf{C}}]\mathbf{X} \tag{2.8}$$

A redefinition is the following: $\widetilde{\mathbf{X}}_{\text{cam}} = \mathbf{R}\mathbf{X} + \mathbf{t}$ where $\mathbf{t} = -\mathbf{R}\widetilde{\mathbf{C}}$ thus the camera can be defined as:

$$\mathbf{P} = \mathbf{K}[\mathbf{R}|\mathbf{t}] \tag{2.9}$$

A summary and decomposition of each of the calibration matrix and extrinsic matrix (camera position in world) are shown below:

$$P = \overbrace{K}^{\text{Calibration Matrix}} \quad \overbrace{[R \mid \mathbf{t}]}^{\text{Extrinsic Matrix}} \tag{2.10}$$

$$= \overbrace{\underbrace{\begin{bmatrix} 1 & 0 & x_0 \\ 0 & 1 & y_0 \\ 0 & 0 & 1 \end{bmatrix}}_{\text{2D Translation}} \underbrace{\begin{bmatrix} f_x & 0 & 0 \\ 0 & f_y & 0 \\ 0 & 0 & 1 \end{bmatrix}}_{\text{2D Scaling}} \underbrace{\begin{bmatrix} 1 & s/f_x & 0 \\ 0 & 1 & 0 \\ 0 & 0 & 1 \end{bmatrix}}_{\text{2D Shear}}}^{\text{Calibration Matrix}} \overbrace{\underbrace{\left[\begin{array}{c|c} I & \mathbf{t} \end{array}\right]}_{\text{3D Translation}} \underbrace{\left[\begin{array}{c|c} R & 0 \\ \hline 0 & 1 \end{array}\right]}_{\text{3D Rotation}}}^{\text{Extrinsic Matrix}} \tag{2.11}$$

So far everything discussed has related to the pinhole camera model, in this case there is a linear model governing the transformation between the world point and the point on the image plane. This is no longer valid when lens distortion occurs. The most important distortion to consider is radial distortion [14]. These are distortions which are radially symmetric and are generally encountered in three forms, each of which is illustrated in Figure 2.15:

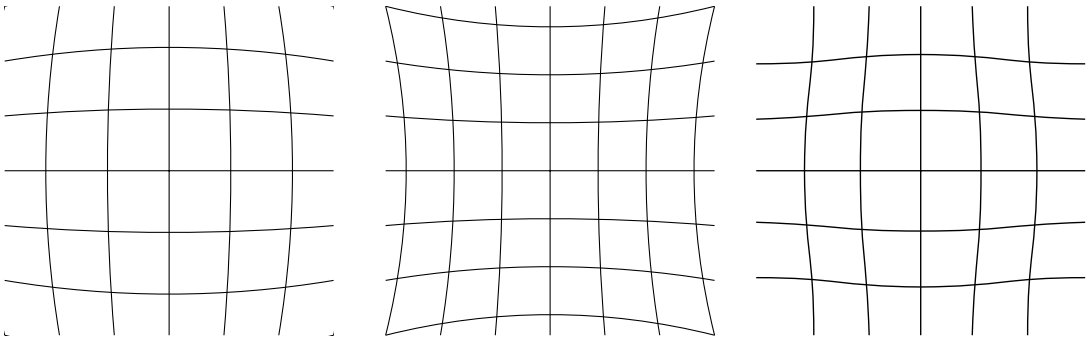

(a) **(b)** **(c)**

Figure 2.15: *Various forms of radial distortion (a): barrel, (b): pincushion & (c): moustache*

In this case the point on the image plane may be given as [14]:

$$\begin{pmatrix} x_d \\ y_d \end{pmatrix} = L(\tilde{r}) \begin{pmatrix} \tilde{x} \\ \tilde{y} \end{pmatrix} \tag{2.12}$$

$(\tilde{x}, \tilde{y})$ is the ideal image position under no distortion (linear projection)

(x_d, y_d) is the image position in the case with radial distortion (non-linear projection)

$\tilde{r}$ is the radial distortion $\sqrt{\tilde{x}^2 + \tilde{y}^2}$ from the centre of the radial distortion $L(\tilde{r})$ is the distortion factor, which is a function of the radius $\tilde{r}$

This factor is calculated during the calibration procedure, often a Taylor series expansion is used [14] to represent the distortion $L(\tilde{r})$.

2.3.1.1.1 Summary of the Pin-Hole Camera Model

In this section we have covered the pin-hole camera model which provides a linear projection between scene points onto the imaging plane. The key components of this model are shown in (Section 2.3.1.1), this presents the following components of the calibration matrix and their practical outcomes:

- x_o, y_o, the camera centre in pixels, determines 2D translation arising from any offset between the pinhole and the centre of the imaging plane (principal point offset).
- f_x, f_y, the focal length of the camera in pixels, determines 2D scaling.
- $\frac{s}{f_x}$, defines the 2D shear, which is related to the focal length and any amount of skew in the camera pixels (2.5).

In reality most cameras do not conform to linear projection, a distortion factor was presented in (2.12). This enables the correction of distortion found to occur with the use of wide-angle lenses for example.

In the following section the omnidirectional camera model will be presented, this is required as the pin-hole model is not suitable for cameras with a significant field of view such as the fisheye camera used throughout these works.

2.3.1.2 Omnidirectional Camera Model

The omnidirectional camera model encompasses a range camera types, of which the fisheye camera belongs, this category of cameras provide a large Field of View (FOV) up to a full 360° [15]. In the case of the results presented in this thesis a fisheye lens was used with a viewing angle of 187°. A schematic of a fisheye lens is shown in Figure 2.16. Example images for comparative purposes, of a pipe flange and internal bore were taken with a fisheye camera with the viewing angle of 187°, and a camera conforming to the pin-hole model with a focal length of 27 mm at the same distance from the flange are shown in Figure 2.17.

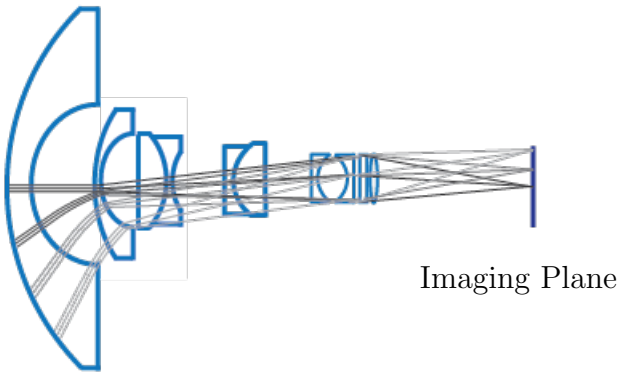

Figure 2.16: *Schematic of a fisheye camera showing the rays of light entering the series of lenses through to the imaging plane [16]*

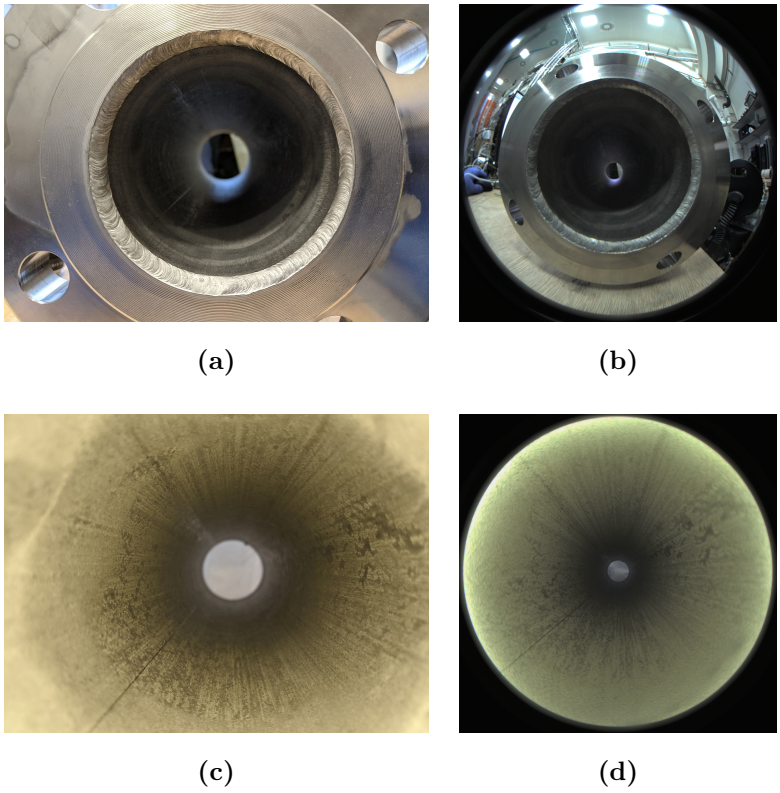

(a) **(b)**

(c) **(d)**

Figure 2.17: *Images taken from the same position relative to the pipe flange, (a) shows an image taken of the pipe flange with a camera with a focal length of* 27 mm*, conforming to the pin-hole model, (b) is the flange taken with a* 187° *fisheye camera, (c) shows the internal bore taken with the pin-hole model camera and (d) likewise with the fisheye camera*

These lenses however, have large amounts of distortion and as such are not compatible with the pinhole model shown in Section 2.3.1.1. The camera model used throughout this work was developed by Scaramuzza and is presented in [17], [18]. The model generalises both the catadioptric cameras (a standard camera imaging a parabolic mirror for example) and dioptric (fisheye cameras) which use a series of lenses to achieve the high Field of View (FOV). The key point of this model is that it accurately represents the camera and provides a description which sat-

isfies the single effective viewpoint criteria - that for each pixel on the sensor there exists a unique vector describing the directionality of the ray of light which illuminated it. Further benefits of this model are that no a priori knowledge of the sensor is required, only that it can be effectively described by a Taylor series expansion [17]. A diagram showing a graphical representation of the model is shown in the mirror effective viewpoint form in Figure 2.18.

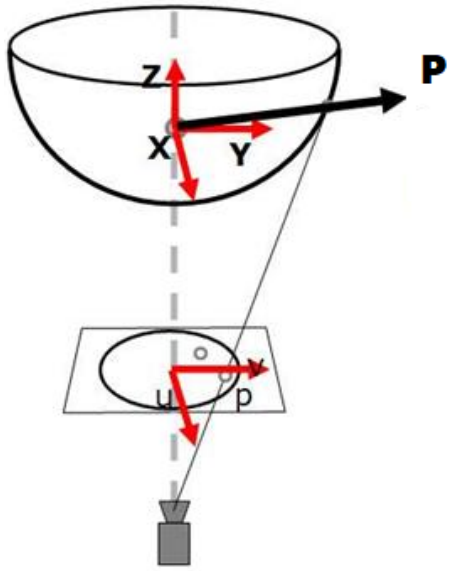

Figure 2.18: *Graphic detailing the omnidirectional camera model [19]*

It is shown by Scaramuzza that we can observe 3D point **P** projected onto the image plane through the following:

$$\mathbf{P} = \begin{bmatrix} x \\ y \\ z \end{bmatrix} = \begin{bmatrix} u \\ v \\ f(u,v) \end{bmatrix} \tag{2.13}$$

Scaramuzza makes a series of assumptions for the model [19]:

1. The model is central and there exists a point in the mirror where every reflected ray intersects - this point is considered the axis origin as shown in Figure 2.18.

2. The camera and mirror axes are well aligned, thus only small deviations in rotation are considered.

3. The mirror is rotationally symmetric.

4. The lens distortion is not considered, for fisheye cameras as this is integrated in the projection function f.

With these assumptions it is possible to relate x, y and u, v with a scaling factor α:

$$\begin{bmatrix} x \\ y \end{bmatrix} = \alpha \begin{bmatrix} u \\ v \end{bmatrix}, \quad \alpha > 0 \tag{2.14}$$

The desired outcome is to map the 3D point $\mathbf{P}$ to the 2D point $\mathbf{p}$ on the image plane. Equation (2.13) can be simplified firstly by the fact that P is a vector thus α can be factored into the function f, secondly that due to assumption 3 f is only dependant on the distance from the image centre $\rho = \sqrt{u^2 + v^2}$. Therefore:

$$\mathbf{P} = \begin{bmatrix} x \\ y \\ z \end{bmatrix} = \begin{bmatrix} u \\ v \\ f(\rho) \end{bmatrix} \tag{2.15}$$

The function chosen by Scaramuzza to represent this function f is a Taylor series expansion:

$$f(\rho) = a_0 + a_1\rho + a_2^2\rho + a_3^3\rho + a_4^4\rho + ... \tag{2.16}$$

In order to mediate assumptions, such as tolerating error in the alignment errors or digitisation errors (skewed pixels), Scaramuzza introduces an affine transformation between the ideal coordinates u, v $(\mathbf{u})$ and the real distorted coordinates u', v':

$$\begin{bmatrix} u' \\ v' \end{bmatrix} = \overbrace{\begin{bmatrix} c & d \\ e & 1 \end{bmatrix}}^{\mathbf{A}} \overbrace{\begin{bmatrix} u \\ v \end{bmatrix}}^{\mathbf{u}} + \overbrace{\begin{bmatrix} x_c \\ y_c \end{bmatrix}}^{\mathbf{t}} \tag{2.17}$$

Where additional parameters x_c, y_c are the centre of distortion forming the matrix $\mathbf{t}$. The affine transformation matrix $\mathbf{A}$ is has the parameters c, d, e.

When combing Equation (2.17) with Equation (2.13) the mapping between a 3D point in space and the point on the sensor plane/mirror is given by:

$$\lambda \begin{bmatrix} (\mathbf{Au} + \mathbf{t}) \\ f(\rho) \end{bmatrix} = \mathbf{PX}, \quad \lambda > 0 \tag{2.18}$$

where $\mathbf{P}$ is the projection matrix, $\mathbf{X}$ is a scene point and λ is the depth or scale factor.

Therefore, at this point, as with the pinhole model, the relation between a point in space and its resulting pixel location on the camera sensor is well defined.

This section has been adapted from [19], for a more in-depth review of the specific model used refer to [15], [18]. Supporting works also include [20]–[23].

2.3.1.3 Camera Calibration

As shown in the previous two sections a camera model and associated projection matrix has been presented for both the standard pinhole camera model and the fisheye camera model. However, the parameters of these matrices must be determined. The process of determining these camera parameters is that of camera calibration. This section will take a practical approach as the goal of the calibration is to define the parameters which minimise the calibration function error as the camera parameters are solved for.

Both calibration methods use a chequerboard calibration pattern; example images are shown in Figure 2.19 of a standard chequerboard taken with an 8 mm lens and a fisheye lens:

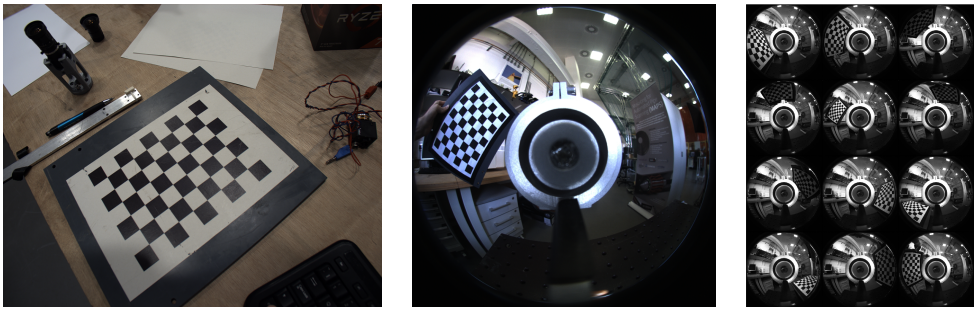

(a) (b) (c)

Figure 2.19: *(a) shows a chequerboard image taken with a* 8 mm *lens, (b) likewise with a* 187° *fisheye camera (note the central region is obscured by the laser module), (c) the complete set taken for the calibration)*

A number of these images are taken, ideally covering the entire area of the image plane. In both cases the first step performed by the calibration is the extraction of the corner points at the intersections of the chequered grid points.

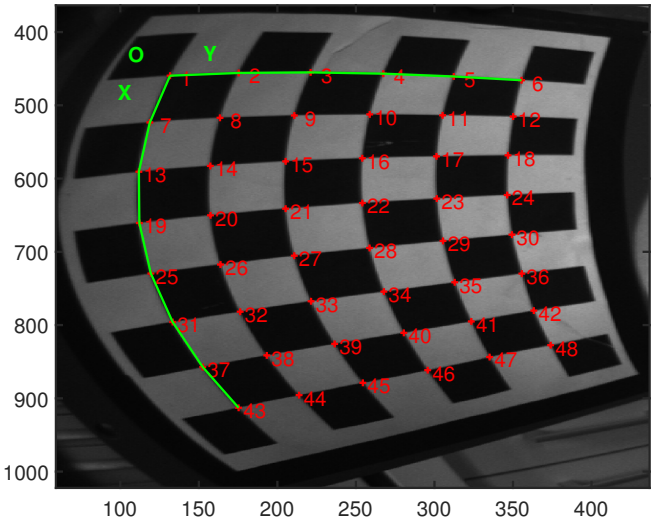

Figure 2.20: *Corner extraction performed on a chequerboard image*

These corner points are known to lie on a plane with a fixed distance between them i.e. they are known 3D coordinates relative to their origin in each image.

Therefore, a series of known series of correspondent points; the pixel location at each corner point and the 3D coordinates on a plane relative to the origin shown in Figure 2.20.

This leaves the problem of the remaining unknowns to solved; in each case these are the cameras extrinsic and intrinsic parameters, which are possible to solve for, generally in an iterative manner minimising the reproduction error across each chequerboard image. The calibration procedure used in this work for the fisheye camera is that of Urban [24] which is an improvement on the work presented by Scaramuzza [18]. For pinhole cameras with lens distortion, the inbuilt toolbox provided by MathWorks is used [25]. It is noted that MathWorks provide an implementation of the omnidirectional calibration method by [24], the pinhole calibration methods referenced by MathWorks are [26], [27]. Furthermore, a review of omnidirectional calibration methods (which pre-dates the work of Urban but includes that of Scaramuzza) is given in [28].

2.3.2 Multiple-View Geometry

In the previous section camera models and calibration methods to obtain said camera model parameters were discussed. In the following section we will discuss multiple-view geometries beginning with a scene imaged by a pair of cameras or

a static scene imaged from two views. The relationship between the two cameras imaging the scene can be expressed in epipolar geometry, and this is why it was emphasised as being of such importance during the discussion of camera models.

2.3.3 Epipolar Geometry

The definition of epipolar geometry given by Hartley and Zisserman [14] is as follows:

> The epipolar geometry is the intrinsic projective geometry between two views. It is independent of scene structure, and only depends on the cameras' internal parameters and relative pose.

This geometry is captured in the fundamental matrix $\mathbf{F}$:

$$x'^{\mathrm{T}}\mathbf{F}x = 0 \tag{2.19}$$

Where x & x' are the imaged 3D point $\mathbf{X}$ in view one and view two respectively.

This is shown graphically for a cameras $\mathbf{C}$ and $\mathbf{C}'$ in Figure 2.21.

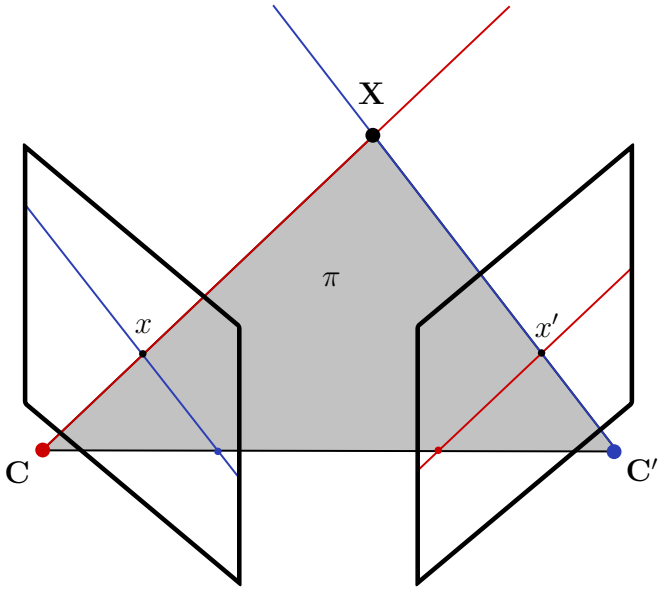

Figure 2.21: *Epipolar diagram where,* **C** *and* **C**′ *are the centres of two cameras viewing the point* X*,* x *&* x' *are the respective points* **X** *is imaged onto the image plane of each camera. The rays to the point* **X** *from the camera centres and the line joining the centres (the baseline) form the image plane* π

The line joining the camera centres is known as the baseline, this along with the two rays leading to the imaged point **X** forms the epipolar plane π. For different points in the scene there are numerous epipolar planes which rotate around the baseline as shown in Figure 2.22.

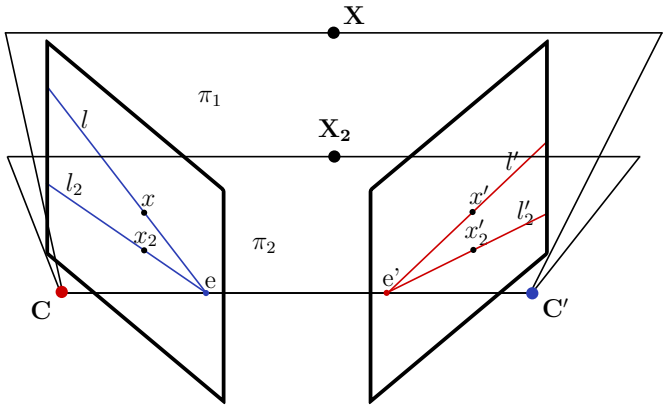

Figure 2.22: *Epipolar planes rotate around the baseline for varying points in space*

These planes collectively are known as the epipolar pencil. The intersection of these planes and the imaging plane forms a series of epipolar lines, these lines intersect at the point where the baseline passes through the imaging plane, this intersection point is known as the epipole e. Each epipolar line is the secondary view of a ray, for example l' is the imaged ray from $\mathbf{X}$ to $\mathbf{C}$ corresponding to x. As $\mathbf{C}$, $\mathbf{C}'$ and $\mathbf{X}$ are coplanar, it can be observed that both x & x' also exist on this plane. This can be used to simplify finding correspondences in stereo image pairs, as if for example we know where x lies on the image plane and we are looking to locate x', we can constrain the search to a single line l'. This line l' is the intersection of the plane π and the image plane of C'.

As mentioned, the epipolar geometry is applicable to omnidirectional cameras using the model shown in the previous section, as shown in Figure 2.23. In this case the 3×1 vectors p_1 & p_2 describing the ray from point $\mathbf{X}$ conform to:

$$p_2^{\mathrm{T}} \mathbf{E} p_1 = 0 \tag{2.20}$$

Where **E** is the essential matrix, the essential matrix is a specialisation of the fundamental matrix where normalised image coordinates are used, this carries with it the requirement that the calibration matrix **K** is known for the cameras.

The relation between the essential matrix and the fundamental matrix is given in [14] :

$$\mathbf{E} = \mathbf{K}'^{T}\mathbf{F}\mathbf{K} \tag{2.21}$$

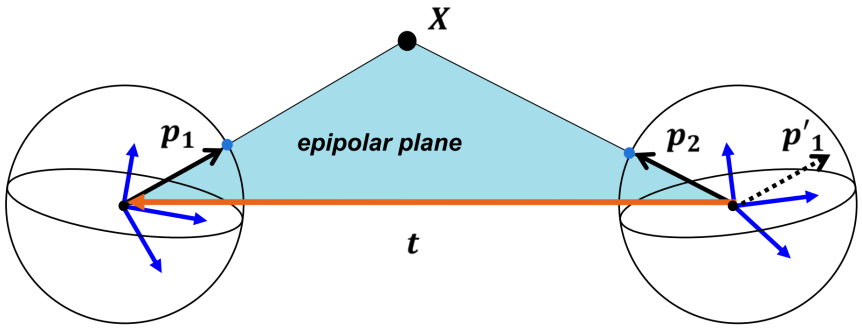

Figure 2.23: *Epipolar diagram for a pair of omnidirectional cameras [29]*

An example of an image pair taken of a building with a rotation and translation applied to the camera is shown in Figure 2.24. Here the fundamental matrix was calculated for an un-calibrated camera using the normalised eight-point method given in the MATLAB toolbox [30]. Thus, eight corresponding points were manually selected in each image. From this point it was then possible to calculated the corresponding epipolar lines for any point in each of the image pairs. This was done for three points in the image, in the left image of Figure 2.24 points are marked with a red circle leading the red epipolar line in the right image. The

same process is observed for creating epipolar lines in the right image with blue markers and blue epipolar lines in the left image. As expected the features are observed to lie on the line as described previously.

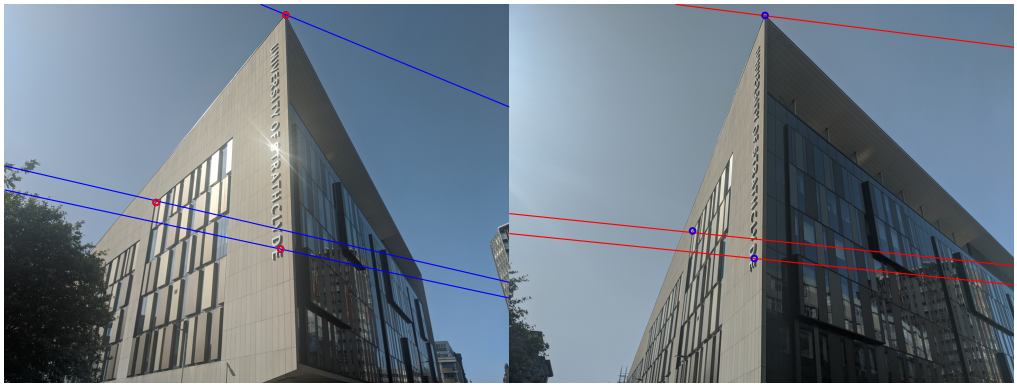

Figure 2.24: *Epipolar lines shown for corresponding points on an image pair red points give red epipolar lines in the image adjacent and vice versa for blue points and lines*

A useful step to take in stereo pair imaging and correspondence locating is to apply a projective transformation to each image such that the epipolar lines are horizontal i.e. $p_y = p_y\prime$, known as rectification [31]. Rectification involves computing a pair of homography matrices to map the epipole to a point of choice: $\begin{bmatrix} 0 & 0 & 0 \end{bmatrix}^\mathsf{T}$ (a point at ∞), thus leading to the fundamental matrix relating the two images $\mathbf{F}^*$ as given in (2.22).

This transform $\mathbf{H}_1$ & $\mathbf{H}_2$ can be applied to create the rectified images $\hat{\mathbf{I}}_1$ & $\hat{\mathbf{I}}_2$ respectively, these are then related by $\mathbf{F}^*$ given in the following equations:

$$\mathbf{F}^* = \begin{bmatrix} 0 & 0 & 0 \\ 0 & 0 & 1 \\ 0 & -1 & 0 \end{bmatrix} \tag{2.22}$$

$$\begin{aligned} \begin{bmatrix} x' \\ y' \\ 1 \end{bmatrix}^{\mathsf{T}} \begin{bmatrix} 0 & 0 & 0 \\ 0 & 0 & 1 \\ 0 & -1 & 0 \end{bmatrix} \begin{bmatrix} x \\ y \\ 1 \end{bmatrix} &= 0 \\ \begin{bmatrix} x' \\ y' \\ 1 \end{bmatrix}^{\mathsf{T}} \begin{bmatrix} 0 \\ 1 \\ -y \end{bmatrix} &= 0 \\ y' - y &= 0 \\ y' &= y \end{aligned} \tag{2.23}$$

Another way to describe the process is that $\mathbf{H}_1$ & $\mathbf{H}_2$ transform the image as if they were taken on a pair of parallel cameras, thus placing the epipoles at infinity and leading to the observed horizontal epilines. This is shown graphically in the following Figure 2.25

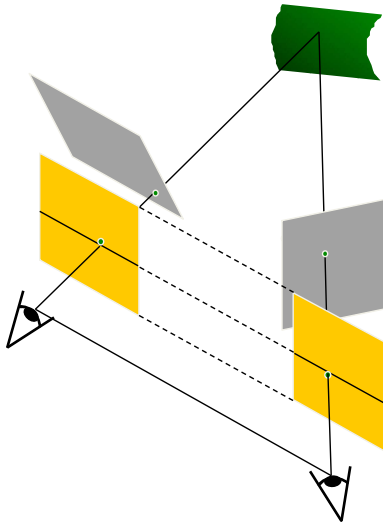

Figure 2.25: *Stereo image rectification process [32]*

The resulting rectified image pair after $\mathbf{H}_1$ & $\mathbf{H}_2$ has been applied is shown in Figure 2.26

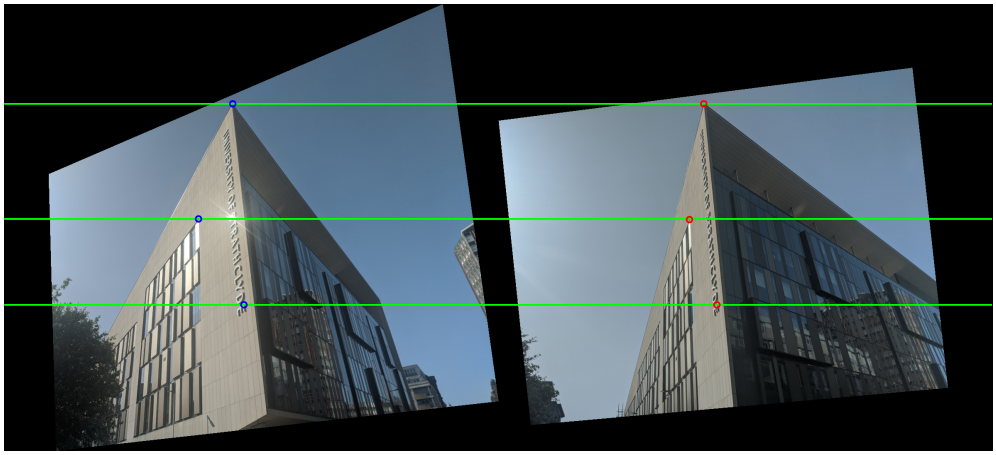

Figure 2.26: *Rectified images with horizontal epipolar lines*

2.3.4 3D Reconstruction

In this section the topic of recovering 3D information from a scene, as imaged by a pair of cameras, in a manner as shown in Figure 2.21 will be covered.

From this diagram it is clear that we can use triangulation from the two points $\mathbf{x}$ and $\mathbf{x}'$ which conform to the epipolar constraint $\mathbf{x}'^{\mathsf{T}}\mathbf{F}\mathbf{x} = 0$ to calculate the 3D-point $\mathbf{X}$. Similarity this holds true for all scene correspondences:

$$\mathbf{x}_i = \mathbf{P}\mathbf{X}_i \quad \mathbf{x}'_i = \mathbf{P}'\mathbf{X}_i$$

For a scene which includes no known geometry including the positions of the cameras relative to one and other and no prior camera calibration you may calculate the Fundamental matrix from scene correspondences and reconstruct a scene up to a projective ambiguity [33]. However, if you have a calibration for all cameras used to capture the scene it would be normal to use the Essential Matrix, this will allow for the reconstruction of the scene up to a similarity ambiguity i.e. only the overall scale, rotation & translation within the world coordinate frame are unknown. These two ambiguities are given illustrated by [14] as shown in Figure 2.27.

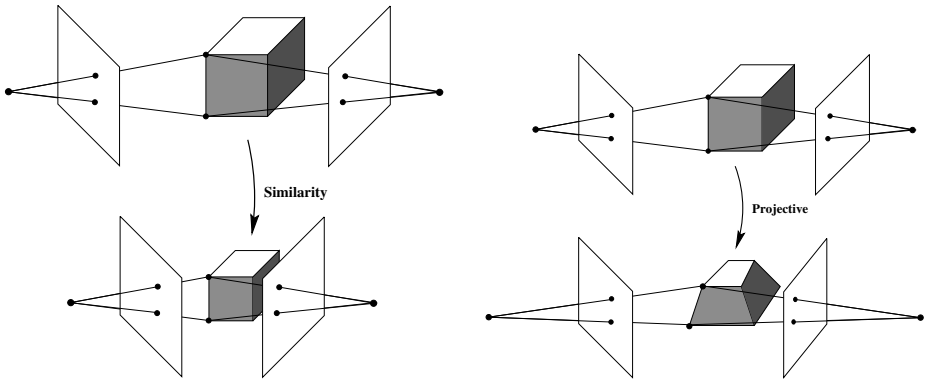

Figure 2.27: *Reconstruction ambiguity. (a) If the cameras are calibrated then any reconstruction must respect the angle between rays measured in the image. A similarity transformation of the structure and camera positions does not change the measured angle. The angle between rays and the baseline (epipoles) is also unchanged. (b) If the cameras are uncalibrated then reconstructions must only respect the image points (the intersection of the rays with the image plane). A projective transformation of the structure and camera positions does not change the measured points, although the angle between rays is altered. The epipoles are also unchanged (intersection with baseline). [14]*

[14] lists many routes to a full metric reconstruction from both a projective and similarity reconstruction for the interested reader. However, in all cases relevant to this work, inspection of the scene will be undertaken with a well calibrated camera and access to some ground truth control points. Therefore, direct reconstruction may be utilised as shown in the following,

$$\mathbf{X}_{\mathrm{E}i} = \mathbf{H}\mathbf{X}_i$$

Where $\mathbf{X}_{Ei}$ represent the ground truth points in the world coordinate frame, $\mathbf{X}_i$ is the corresponding point in the reconstruction and $\mathbf{H}$ represents the homography between the two, which has a total of 15 degrees of freedom, with five known points in the scene, and the condition that four of which are non-coplanar, it is possible to go from a projective matrix to a metric solution. For a similarity reconstruction, only two points are required.

Scaling is common step simplified using software such as MeshLab [34] for scaling reconstructions produced by Structure from Motion (SfM) (see Section 2.3.5.4) software and commercial solutions such as Agisoft [35]. The output from these are normally known to a similarity where the scale is given by the distance between the first two cameras in the sequence. In the case of a pipe the overall model may be scaled by a known diameter i.e. two points on a known pipe circumference of the reconstruction.

In terms of calculating the 3D points $\mathbf{X}_i$, there are many methods and approaches to calculation and minimisation of the error, due to the fact that in reality you face noise in your image correspondences, calculated Fundamental/Essential Matrices. For a review of the methods available and implementations, the interested reader is advised to refer to [36].

A key point is the uncertainty of the reconstruction, for a single image pair this is largely dependent on the baseline between the cameras. A small baseline will lead to an increased error/uncertainty and for a large baseline this comes at the cost of an increased difficulty in locating the correspondences i.e. the search problem difficulty has increased. These regions of uncertainty are illustrated

in the following Figure 2.28. This figure is particularly poignant for the work presented within this thesis as the camera generally travels centrally along a pipe section thus the images frames are nearly parallel.

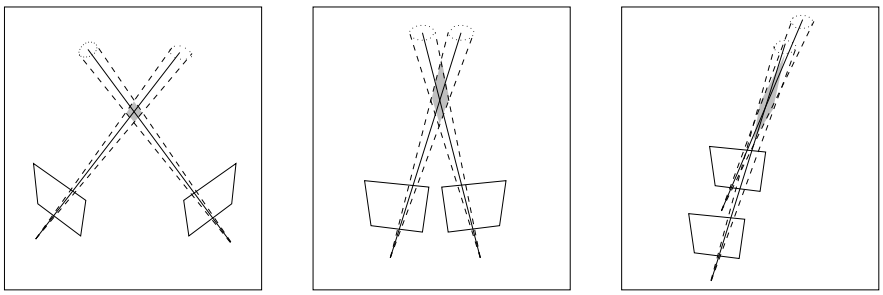

Figure 2.28: *Uncertainty of reconstruction. The shaded region in each case illustrates the shape of the uncertainty region, which depends on the angle between the rays. Points are less precisely localized along the ray as the rays become more parallel. Forward motion in particular can give poor reconstructions since rays are almost parallel for much of the field of view. [36]*

Thus far we have only considered two-view geometry, in increasing the number of viewpoints to three a new concept is introduced known as the trifocal tensor. The trifocal tensor can be considered the equivalent of the Fundamental Matrix for the two-view case, the three-view case however leads to the creation of a projective reconstruction with the use of un-calibrated cameras [37].

2.3.5 3D Reconstruction Methods

In this section a selection of methods for obtaining three-dimensional information from images will be presented including stereo vision, active stereo, structured light & SfM.

2.3.5.1 Stereo Vision

Stereo vision was covered in the previous section with the introduction to epipolar geometry and 3D reconstruction from two views. However, here the term will be used to refer to a well calibrated stereo rig comprised of two cameras where one is deemed to be the origin and the translation and rotation relative to this of the second camera is very well known.

This enables in a single image the generation of what is often called a 2.5D image or a depth map. This is shown for a simple case where the cameras are both aligned on the same plane towards a central target in Figure 2.21.

2.3.5.2 Active Stereo

Active stereo is similar to that of stereo vision, except instead of imaging the ray from another viewpoint and needing to find matching correspondences a light source is projected which can be easily extracted, thus solving the correspondence problem or other design limitations such as enabling a smaller design.

The probe used within this project falls under the category with a single omni-directional camera obtaining geometrical information through the triangulation of a well-known laser ring projection. A full description and error analysis of this method is given in Chapter 4.

A typical-triangulation based stripe solution is shown in Figure 2.29 which was state of the art in 2000. It was designed with a resolution of 0.25 mm to preserve fine details (chisel marks) but not have the dataset become too large to manage for scanning large statues/structures [38].

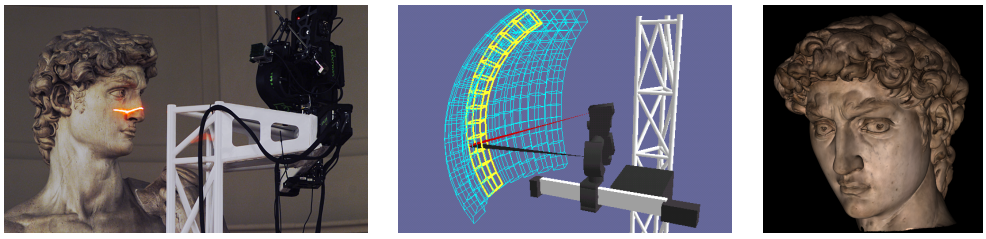

(a) **(b)** **(c)**

Figure 2.29: *(a) in-situ laser stripe scanning of David by Michelangelo, (b) working volume of the sensor in use showing the capturing range and triangulation, (c) render of the captured data [38]*

Many variants of this technique exist generally all aiming to solve the correspondence problem while increasing coverage and accuracy such as those shown in Figure 2.30, the technique developed in [39], the example shown is a demonstration of their one-shot technique with multiple shots leading to higher resolution reconstructions.

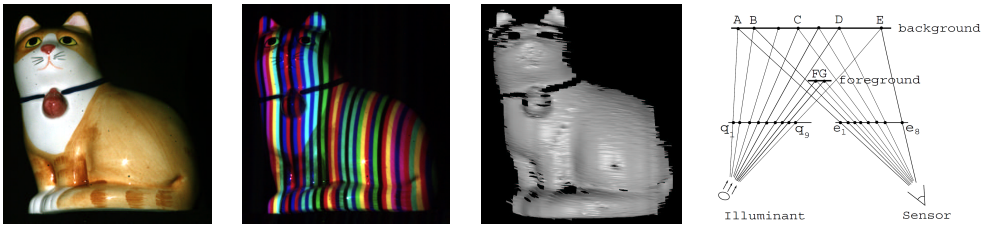

(a) (b) (c) (d)

Figure 2.30: *Images taken showing the tolerance to surface reflections: (a) Photo of original porcelain cat model. (b) Stripe image used for one-shot reconstruction. (c) Shaded rendering of the DP reconstruction, (d) stripes in schematic view detailing foreground occlusion as part of the algorithm development, with further information given in the source material: [39]*

2.3.5.3 Time of Flight

Another method to generate depth images from a single viewpoint is to utilise a time of flight measurement, the depth is taken from the time of a projected light source to travel to the scene elements and back to the sensor. One of the most prevalent implementations of this technology is the Kinect V2 [40] which is capable of operating at 30 Hz with a depth image resolution of 512 × 214 pixels and an RGB image of 1920 × 1080 pixels. Being affordable and having a well-established ecosystem and SDK led to prevalent use throughout the studies in its accuracy and use for 3D reconstruction & robotics [41]–[49].

The specifics of the sensor, and many like it within the class are that; it consists of an RGB camera to detect the visible spectrum and an IR camera to capture the depth information by measuring the time of flight of an IR pattern projection on the scene.

A key advantage of this technique over the stereo methods including active stereo and passive stereo is that there is no separation required between the emitter and receiver i.e. a baseline and the robustness that comes with this [50].

2.3.5.4 Structure from Motion

Structure from Motion (SfM) is the most complex and unbound solution which may utilise elements as the input data from the aforementioned methods to build a reconstruction.

The outline of structure from motion is that from a set of unordered images the camera positions and structure can be reconstructed.

This method was introduced to the literature as early as 1979 by S. Ullman in 'The Interpretation of Structure from Motion' [51].

A lot of work has since gone into developing the technique since that point in time with breakthrough work such as the reconstruction of the Rome Coliseum & other locations from 2097 tourist photographs introduced in [52]. The resulting coloured point cloud and camera views are shown in Figure 2.31. This led to future works such as 'Reconstructing the World* in Six Days' [53].

Figure 2.31: *Point cloud of a reconstruction of Rome Coliseum generated from tourist photographs [54]*

The process of incremental SfM is illustrated in the following from the process in use by [55]

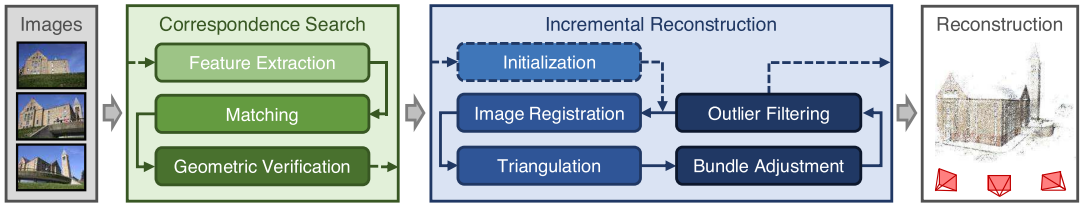

Figure 2.32: *Incremental Structure from Motion pipeline [55]*

Each of these steps is key to the process and largely similar enough through each SfM process to act as a standard.

Feature extraction involves identifies features within the image. These features are then stored as a descriptor which can be used for Matching which is the next step in the process, feature extraction & descriptors will be covered in more detail in the following section.

Geometric verification utilises epipolar geometry as covered in the previous section to verify potential image pairs. If a transformation of the camera in rotation and translation is found, which may map one set of image features onto the other with a significant number of inliers, the image pair is verified as an overlapping scene.

At this point in this particular process, the reconstruction phase begins with the input of a scene graph (see [53], [56]–[58]) with verified image pairs (from the geometric verification) as the edges and images as the nodes. The first step of this process is the initialisation of the model. It is initialised from reconstruction of a from an initial pair of images, i.e. a two-view reconstruction as covered in Section 2.3.3. The choice of the image pair comes down to a choice between computation time and robustness/accuracy [58]. An initial seed in a dense location tends itself to the robust/accurate case whereas an initial image pair from a sparse location in terms of image overlap will lead to a quicker reconstruction due to the nature of bundle adjustment.

Following initialisation, new views are registered to the model through the process of image registration. From a reconstruction the views are introduced by utilising the Perspective N-Points (PnP) (as used in Chapter 4). This allows for an estimation of the camera pose and intrinsic parameters (the amount of information obtainable from the scene was detailed in Section 2.3.3 and further details are given in the reference material on the subject [14]).

The next step in the SfM process is to perform triangulation, the newly registered image is in observation of existing points (a requirement of PnP). It may also observe and introduce new scene points, with a minimum of two views of a point in the scene, these new points may be triangulated as discussed prior. Through this step more 2D to 3D correspondences are introduced into the model, allowing for the possibility of an introduction of new image registrations in the consequent loops as shown in Figure 2.32.

Bundle Adjustment [59] is then applied to the set, the name originates from the bundles of light rays leaving each 3D feature and travelling to the camera centres. These bundles are adjusted together, in one geometric parameter estimation which is adjusting the: 3D feature coordinates, camera poses and calibrations in one single problem Lastly, outliers are removed from the set.

This overview of SfM has focussed on the methodology given in [58] known as COLMAP. Other prominent solutions include Bundler [60] (part of the Rome in a Day project) and VisualSFM [61]–[63]. Following on from these academic endeavours there has been a rise in commercial solutions offering a streamlined solution for end users wanting to utilise photogrammetry (many new entries in the market space focussing efforts the rise of UAV visual inspection enabling reconstruction of large or remote sites [64]) such as Agisoft (generic) [35], Pix 4D (aeirial) [65], ReCap Pro (generic) [66] & Reality Capture (generic) [67] among many others offer turnkey solutions making photogrammetry more accessible than ever.

2.3.5.5 Visual Odometry

Visual odometry is a less general process compared to SfM, the goal of visual odometry is to estimate the camera pose in 3D and not the structure or scene. Images are captured in an ordered manner as oppose to the unordered examples shown in the previous section. The pose is calculated from frame to frame by matching features between the two frames and computing the transformation which relates them in a similar manner to the image registration step described in the SfM process. However, by operating between sequential frames, the error between poses grows overs over time with the introduction of each frame causing drift, the error can however be reduced by applying Bundle Adjustment to the entire dataset, this is shown graphically in Figure 2.33. This is generally not the case when performing real time localisation of the camera such as in the later section of work presented.

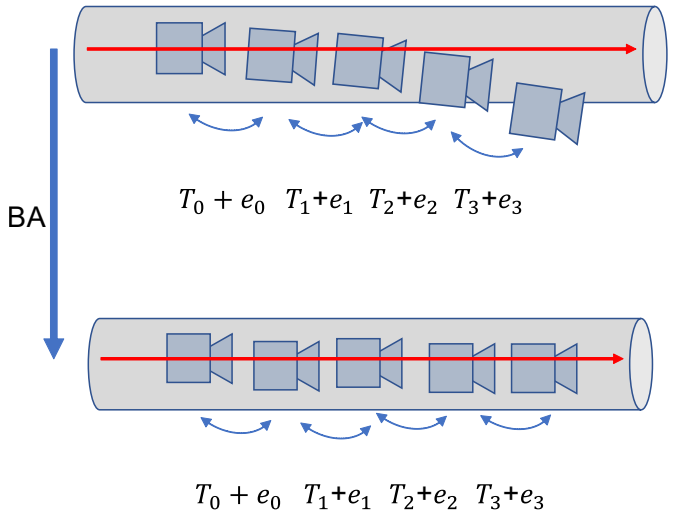

Figure 2.33: *Example of Visual Odometry drift and compensation by Bundle Adjustment*

2.3.6 Feature Extraction

Thus far in examples such as stereo vision and SfM, we have assumed correspondences between points in an image to be known, this is largely not the case as the relationship between corresponding points in a scene imaged from differing views is unknown at the time of capture, they must be determined through a process. This process, known as feature extraction and matching, enables an automated method of correspondence matching between images.

For this reason, we will be focusing on what are known as low-level features, such as edges, corners and patch-based detectors (SIFT etc.).

Within this subset of low-level feature detectors, we will briefly cover corner detection (peaks of local curvature where curvature may be defined as the rate of change in edge direction [68]) but the main focus will be the patch-based feature detectors which are most commonly used within the realm of 3D-Reconstruction.

There are many methods for edge detection with one of the most popular methods being [69] with an example usage shown in Figure 2.34b. Another method which is utilised is the Laplacian of Gaussian i.e. a second derivative edge operator of an image which has been smoothed by a gaussian to make it less susceptible to noise in the image as used in [70].

As mentioned corner detection captures the rate of change in edge direction, an example of this is shown in Figure 2.34.

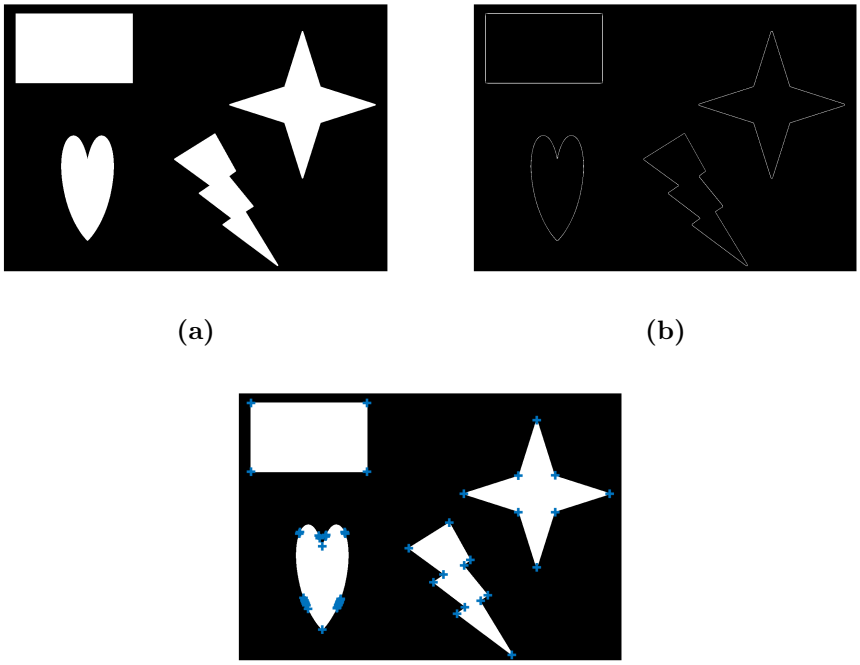

(a) **(b)**

(c)

Figure 2.34: *Example of corner detection (a): input image, (b): result of Canny Edge Detection & (c): 50 Strongest Corners from Harris Corner Detection*

In the example shown in Figure 2.34b, the Canny Edge detection method [69] is used to highlight the edges of the image and the Harris method [71] for corner detection, with the 50 strongest corners shown. The corners are generally in the locations as expected when considering changes of edge direction. This method of corner detection is used for extracting targets in Chapter 4.

These early methods of feature extraction are not robust to changes in scale, that is where the use of SIFT and its counterparts may provide a suitable method which are generally robust to variations in scale, rotation & some illumination changes.

We will first consider and provide an in-depth description of the SIFT algorithm for feature extraction and description as described by Lowe in [72], [73]. This is undertaken as SIFT is generally used as a benchmark to compare other methods to. Multiple scales within SIFT are achieved through successive gaussian blurring, each scale is separated by a multiplicative factor k applied to a smoothing factor σ. These scales are then subtracted from their neighbours to create a Difference of Gaussian (DoG). The DoG is the first step in detecting the features and is a computationally efficient method for approximating the Laplacian of Gaussian [74] across the scale space the algebraic form in Equation (2.27) and pictorially in Figure 2.35. Each set of scaled images is known as an octave, successive image sets are scaled down by half to form consecutive octaves. The recommendation is for the use of four octaves each containing five different scales with expanded reasoning to follow.

$$L(x, y, \sigma) = G(x, y, \sigma) * I(x, y) \tag{2.24}$$

$$G(x, y, \sigma) = \frac{1}{2\pi\sigma^2}\epsilon^{-(x^2+y^2)/2\sigma^2} \tag{2.25}$$

$$D(x, y, \sigma) = (G(x, y, k\sigma) - G(x, y, \sigma)) * I(x, y) \tag{2.26}$$

$$= L(x, y, k\sigma) - L(x, y, \sigma) \tag{2.27}$$

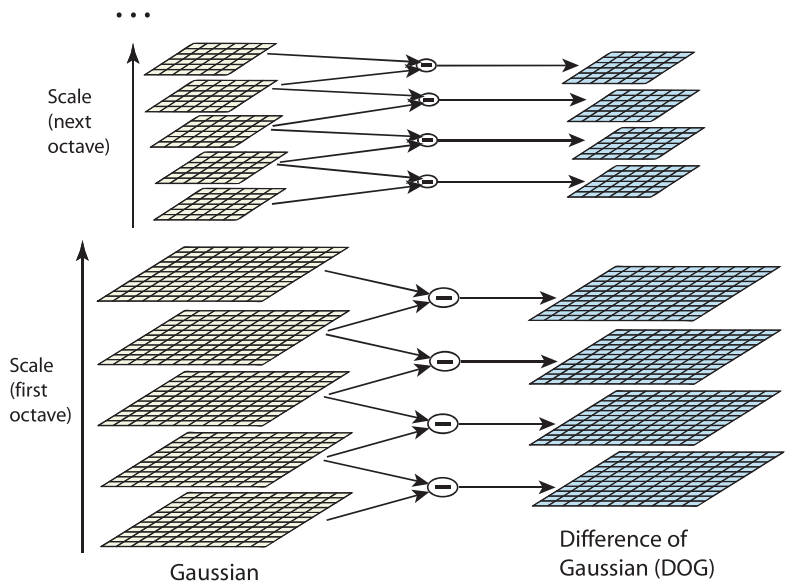

Figure 2.35: *For each octave of scale space, the initial image is repeatedly convolved with a Gaussian to produce the set of scale space images shown on the left. Adjacent Gaussian images are subtracted to produce the DoG images on the right. After each octave, the Gaussian image is down-sampled by a factor of 2, and the process repeated. [72]*

At this point there now exists a series of DoG images - an approximation of the Laplacian of Gaussian which is robust to scale changes, providing corners and edges within the image which will be used to create keypoints.

The next step of this process is to detect minima and maxima within the the DoG images. The comparison to determine if a point in the image is a minima or a maxima takes place in 3x3 grids for at three consecutive scale levels (thus excluding the search based on the scales at the extrema of the octave as there is only one neighbour to compare with) as shown in Figure 2.36.

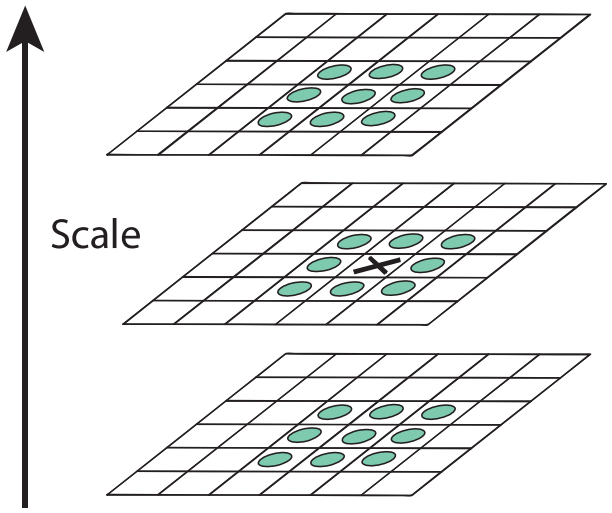

Figure 2.36: *Maxima and minima of the difference-of-Gaussian images are detected by comparing a pixel (marked with X) to its 26 neighbours in 3x3 regions at the current and adjacent scales (marked with circles) [72]*

The point is only taken if it is greater than all the neighbours or less than all the neighbours. More information is given in the source material [72] on the impact of the sampling frequency with respect to determining the scale & spatial sampling frequency which locates the extrema in the most stable fashion. Following the location of the maxima and minima within the pixel grid, the next step in Lowe's process, is to determine the sub-pixel peak obtained by fitting a 3D quadratic function to the local sample points first presented in [75]. The method used is that of a Taylor expansion on the scale-space function, $D(x, y, \sigma)$ given in Equation (2.27), where the function is shifted so the origin is at the point being sampled. Resulting in:

$$D(x) = D + \frac{D^T}{X} \tag{2.28}$$

A key outcome of understanding this process is that the value of $|D(\hat{x})|$ is the value used to define the contrast threshold to remove features with low contrast.

Furthermore, along with removing features with a low contrast is to remove edge responses which are features which naturally result from the DoG's strong response along edges. To determine if it is a low-quality feature arising from this, effect the authors investigate if it is a poorly defined peak within the DoG. This can be determined by the fact, as stated by the authors, that it will have a large principal curvature across the edge but a small one in the perpendicular direction.

This can be computed from a Hessian matrix **H** computed at the location and scale of the keypoint.

$$H = \begin{bmatrix} D_{xx} & D_{yy} \\ D_{xy} & D_{yy} \end{bmatrix} \tag{2.29}$$

The eigen values of **H** are proportional to the principal curvature of D. Lowe utilises an approach from [71], to bypass having to compute the eigenvalues as it is only the ratio which is of interest. If α is the eigenvalue with the largest magnitude and β that with the smaller one then the sum of the eigenvalues from the trace of H can be computed and their product from the determinant.

$$\mathrm{Tr}(\mathbf{H}) = D_{xx} + D_{yy} = \alpha + \beta \tag{2.30}$$

$$\mathrm{Det}(\mathbf{H}) D_{xx} D_{yy} - D_{xy}^2 = \alpha\beta \tag{2.31}$$

If Det($\mathbf{H}$) is negative the point is discarded. The following step is to calculate the ratio r between the largest magnitude eigenvalue and the smaller one such that $\alpha = r\beta$. It is this ratio which determines the edge threshold, the value of $(r+1)^2/r$ is a minimum when the eigen values are equal and increases as r increases; thus, the value of r is given to set the threshold which relates to the ratio of principal curvatures.

$$\frac{\mathrm{Tr}(\mathbf{H})^2}{\mathrm{Det}(\mathbf{H}} = \frac{(\alpha+\beta)^2}{\alpha\beta} = \frac{(r\beta+\beta)^2}{r\beta^2} = \frac{(r+1)^2}{r} \tag{2.32}$$

At this point a set of keypoints exists which have been calculated based on the DoG from multiple scales of the image and have been filtered to remove weak features on edges and those with a lack of contrast. The next step in the process is to assign an orientation to the keypoint to add invariance to image rotation.

To do this for each keypoint a local orientation is generated. To do this the Gaussian smoothed image L is taken from the scale the keypoint's maxima/minima was extracted from. Within this image around the keypoint a gradient magnitude $m(x, y)$ is calculated:

$$m(x,y) = \sqrt{(L(x+1,y)) - L(x-1,y))^2 + (L(x,y+1) - L(x,y-1))^2} \quad (2.33)$$

Also an orientation $\theta(x, y)$:

$$\theta(x,y) = \arctan \frac{L(x,y+1) - L(x,y-1)}{L(x+1,y) - L(x-1,y)} \quad (2.34)$$

From this information a histogram of orientations is formed in a region around the keypoint, the orientation histogram has a total of 36 bins covering the 360 degrees of orientation possible. Each sample added to the histogram is weighted by the gradient magnitude at that sample point as well as a Gaussian-weighted circular window with σ value 1.5 times the scale of the keypoint. The peaks of the histogram represent the dominant gradient directions of the local gradients within the image. Those within 80 % of the maximum peak & the maximum peak itself are taken as used to create keypoints. This results in keypoints at the same location but with different orientations, Lowe states however that only around 15 % of keypoints were found to result in multiple orientations in this way, however, those that did contributed strongly to the stability of feature matching.

A two-dimensional descriptor now needs to be created which describes the patch of the image we wish to match robustly in a manner that remains as invariant as possible to changes in the image. The descriptor consists of a 4x4 grid of gradient orientations around they keypoint (aligned using the orientation previously calculated to add rotational invariance). A reduced for clarity 2x2 example is shown as created and captioned by Lowe in Figure 2.37. To calculate these gradient orientations each of the grids is divided into a sub grid of size 16x16, for each of these a gradient is known (from the prior calculation from the orientation assignment). These gradients are then weighted by a circular Gaussian window again as illustrated in Figure 2.37. This will increase the weight of those closer to the keypoint, alleviating large changes in the descriptor based in small movements away from this centre point. The orientations are then binned into eight bins, via the method of trilinear interpolation, again to make the descriptor more robust to minor changes in the sampled orientation. This results in a 4x4 grid each containing a histogram with 8 orientation bins, forming the 128-element feature vector describing the keypoint. The final two steps provide robustness to changes in illumination, the first of these is to normalise the vector, thus if in an image brightness is increased uniformly, there will have no impact on the descriptor. Secondly the influence of large gradient magnitudes is reduced by setting a threshold for each unit vector of 0.2, and re normalising after this has been applied. This is beneficial as the distribution of orientations is of greater value than contribution from a large gradient. The authors provide reasoning for their choice of this vector with respect to the number of orientations r and the width of the array n leading the vector size rn^2. The main outcome is a balance

between uniqueness within a large database, and not becoming overly sensitive to shape distortion and occlusion. A study of these parameters is given in [72] with respect to sensitivity to viewpoint angle change.

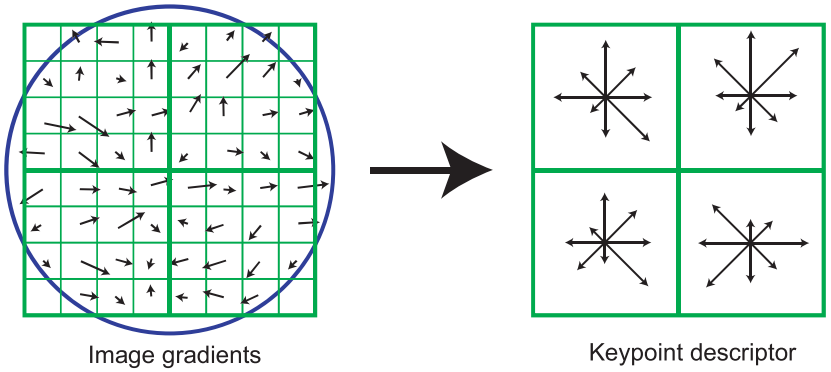

Figure 2.37: *A keypoint descriptor is created by first computing the gradient magnitude and orientation at each image sample point in a region around the keypoint location, as shown on the left. These are weighted by a Gaussian window, indicated by the overlaid circle. These samples are then accumulated into orientation histograms summarizing the contents over* 4×4 *subregions, as shown on the right, with the length of each arrow corresponding to the sum of the gradient magnitudes near that direction within the region. This figure shows a* 2×2 *descriptor array computed from an* 8×8 *set of samples, whereas the experiments in this paper use* 4×4 *descriptors computed from a 16x16 sample array. [72]*

To match the features between images, Lowe states that the best candidate is found by identifying its nearest neighbour within the database of features. This is the feature with the minimum Euclidean distance between the 128 elements of the description vector. An exhaustive search would find such a candidate, but would be computationally expensive to implement therefore Lowe utilised an approximate algorithm Best-Bin-First (BBF) [76]. In their tests on a database of 100k keypoints, over the exhaustive search it performed 2 orders of magnitude quicker with only a loss of 5 % in the number of correct matches.

2.3.6.1 SIFT Alternatives

One area where many other keypoint detector and descriptors in the literature aim to improve on SIFT is the time taken to create the descriptors, and to match them. One such example is Speeded-Up Robust Features (SURF) [77], [78]. SURF achieves this in a number of ways. Firstly, the approach taken to create the Gaussian blurred images where SIFT applies a Gaussian smoothing operator (Equation (2.27)) and then resampling, SURF uses an approximation for the Laplacian of Gaussian. The template of the operation for $\sigma = 1.2$ (the lowest scale used) convolved with the image is shown in Figure 2.38. The approximation is given in [77] as:

$$\det(H_{\text{approx}}) = D_{xx}D_{yy} - (wD_{xy})^2 \tag{2.35}$$

Where H is the Hessian matrix w is the relative weight of the filter and D_{xx}, D_{yy}, Dxy are the box filters/templates as shown in Figure 2.38.

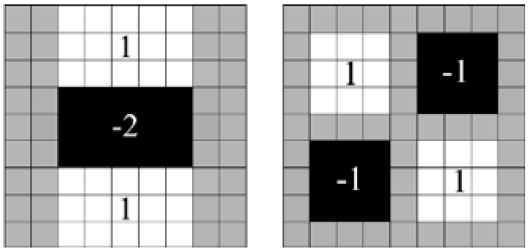

Figure 2.38: *Left, vertical second order approximation. Right, diagonal second order approximation [77]*

To compute different scales with this method, the template is scaled as shown in Figure 2.39. The scale space remains divided into octaves where an octave contains a scaling factor of two. The template widths for three octaves are shown in Figure 2.40.

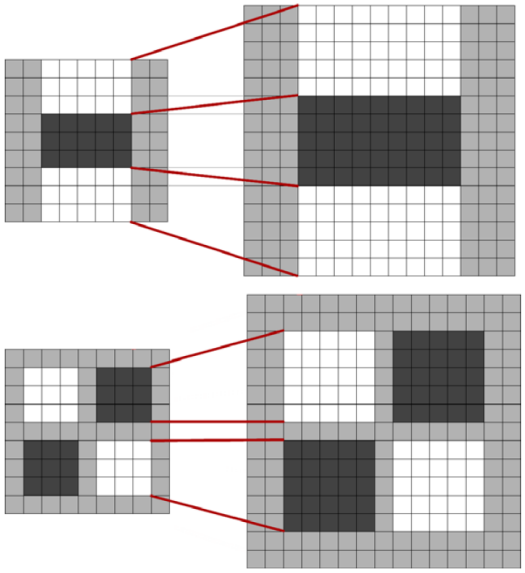

Figure 2.39: *Templates for vertical and diagonal second order approximation for two successive scales [77]*

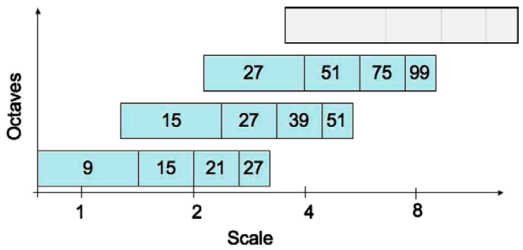

Figure 2.40: *Graphical representation of the filter side lengths for three different octaves. The logarithmic horizontal axis represents the scales. Note that the octaves are overlapping in order to cover all possible scales seamlessly [77]*

To determine the keypoints within these images, a non-maximum suppression on a 3 x 3 x3 neighbourhood is applied as given in [79]. To accurately locate maxima from (Section 2.3.6.1) the authors use the same interpolation method as in SIFT.

Orientation of the keypoint is determined through the use of two Haar wavelet responses which are binary wavelets, one is used in the x, direction, the other in the y direction. Shown in Figure 2.41.

A circular region is established around the keypoint based with a radius six times the scale size (s) with a sampling step also of s. The wavelet size is also set to a length based on the scale ($4s$). A gaussian is applied centred at the keypoint with a σ value of $2s$. To determine the dominant direction, a sliding orientation window of size $\frac{\pi}{3}$ is used to sum the horizontal and vertical responses. The longest vector determines the orientation of the keypoint, the process is shown graphically & as captioned by Bay in Figure 2.42.

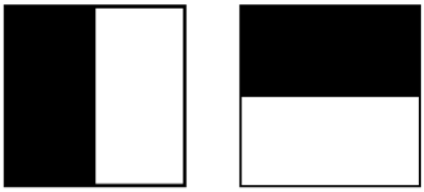

Figure 2.41: *Haar wavelet filters to compute the responses in x (left) and y direction (right). The dark parts have the weight +1 and the light parts -1 [77]*

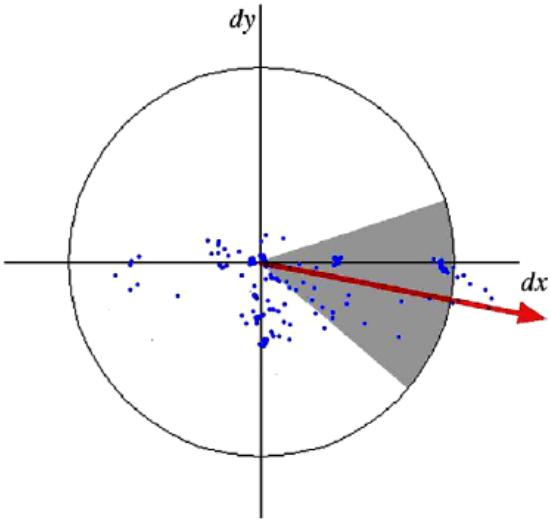

Figure 2.42: *Orientation assignment: a sliding orientation window of size* $\frac{\pi}{3}$ *detects the dominant orientation of the Gaussian weighted Haar wavelet responses at every sample point within a circular neighbourhood around the interest point [77]*

To create a descriptor, a rectangular grid is used to sample an area of $20s$ centred on the keypoint with an orientation given by the keypoint orientation divided up into a 4x4 sub grid. This is subdivided further and a horizontal (d_x) and vertical (d_y) response to a Haar wavelet again with a gaussian weighting taken. The sum of these are taken for each sub-grid grid and the absolute sum, resulting in a 4x4x4 descriptor which is transformed into a vector of length 64 and normalised. This is again shown graphically by Bay in Figure 2.43.

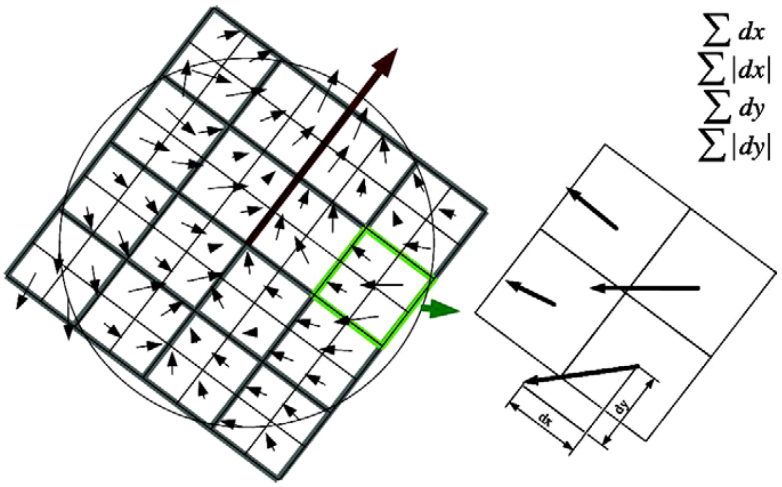

Figure 2.43: *To build the descriptor, an oriented quadratic grid with* 4×4 *square sub-regions is laid over the interest point (left). For each square, the wavelet responses are computed from* $5\times$ *samples (for illustrative purposes, we show only* 2×2 *sub-divisions here). For each field, we collect the sums* $d_x, |d_x|; d_y, and |d_y|$*, computed relatively to the orientation of the grid (right) [77]*

Furthermore, to the approximations and template-based methods, SURF aims to improve computation time within the matching phase of descriptors as well. This is achieved through what the authors of SURF call fast indexing for matching, during the computation of the keypoints the sign of the Laplacian (trace of the Hessian matrix) is obtained. This defines if the feature is a bright blob on a dark background or a dark blob on a bright background. Therefore, only keypoints with the same signs are considered for matching speeding up the process. Through these methods, the authors claim a five times improvement in computation time over SIFT when the SIFT thresholding (contrast & edge) parameters set to result in an equal number of keypoints detected by SURF.

In some real-time applications which require even more efficient methods for determining keypoints and matching them. These often fall under the category of binary descriptors. One of the most prevalent of these is Oriented FAST and Rotated BRIEF (ORB). As the name suggests it utilises and extends upon Features from Accelerated Segment Test (FAST) [80] a keypoint detector and Binary Robust Independent Elementary Features (BRIEF) [81] as a descriptor. FAST determines a keypoint based on a method of taking a central pixel and comparing it to its surrounding neighbours the authors of ORB utilise a radius of 9 known as FAST-9. A graphical example of this comparison is given in Figure 2.44.

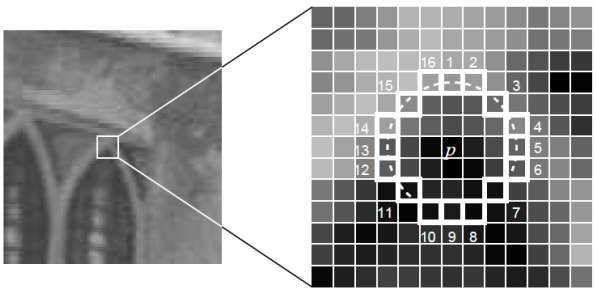

Figure 2.44: *Example central pixel threshold comparison [80]*

The authors of ORB make two key improvements to improve the performance of FAST, firstly they state that FAST is susceptible to large responses along edges. To alleviate this, they utilise a Harris corner measure to rank the keypoints detected, with a target of N keypoints the top keypoints as ranked by this measure are selected. Secondly to provide FAST features at multiple scales, the process is repeated in a scale pyramid of the image similar to that of SIFT. Finally, with

reference to the FAST keypoint they implement an orientation using the intensity centroid method given in [82]. As mentioned for the descriptor, a modified form of BRIEF is used, BRIEF utilises binary strings to describe the features within an image. This leads to both fast construction and matching performance. BRIEF is built up by performing binary tests between pixels in smoothed image patches. In its standard form it is not invariant to in-plane rotational changes. To add invariance to the BRIEF descriptor Rublee et. al. implemented Steered BRIEF. This is done through modifying the BRIEF operator with the orientation of the keypoint detected previously (discretised into 12-degree increments). This however led to a reduction of variance which caused a reduction performance. This was overcome in Rotation-Aware Binary Robust Independent Elementary Features (rBRIEF) which was constructed by learning which features from a large data set led to high variance with uncorrelated tests. The key outcome of [83] is however the performance increase it offers on SIFT and SURF which it compares itself to. To validate the matching performance, they performed a known transformation to a test images and determined the number of matching inliers. These images contained a similar number of keypoints, ORB was found to outperform SIFT and SURF by 10 %. The main point of this method however is the performance and it was noted that the per frame time for detection was an order of magnitude faster than SURF and for SIFT two orders of magnitude faster. Although in the experience of the author of this thesis is that the computation time for all methods has fallen drastically in the nine years since publication of the paper.

There are indeed many more methods available to detect keypoints, provide descriptors and implement efficient matching regimes. These have been covered in a number of reviews [84], [85]. [86] provides a recent review of matching using local descriptors including recent trends such as deep descriptors and data-driven descriptors.

Within this project a large number of methods were considered for feature matching within pipes to enable SfM & Visual Odometry. These are summarised in the following table.

SIFT was chosen for use throughout the wider project and was thoroughly investigated by the wider team with an overview of feature descriptors shown in Table 2.2.

Feature Extraction Algorithm	Type	Strength	Weakness	Applications	Implementation	Citations
SIFT	Detector + Descriptor (Floating Point)	Used in prior work at UoS/Used pervasively in literature	Speed for realtime, although maybe mitigated by SiftGPU	Broad spectrum of computer vision systems	Matlab/C++	31756
SURF	Detector + Descriptor (Floating Point)	Commonly used in the literature as faster alternative to SIFT	Speed for realtime	Visual SLAM/Odometry	Matlab/C++	6038
ORB	Detector + Descriptor (Binary)	Small descriptor/Speed	Reliability and robustness when the image undergoes in plane rotations	Visual SLAM	OpenCV	1261
BRISK	Detector + Descriptor (Binary)	Small descriptor/Speed	Reported to be less accurate than SIFT in [1]	Visual SLAM /Relevant industrial inspection "A UAV System for Inspection of Industrial Facilities"	Matlab	819
FREAK	Descriptor (Binary)	Small descriptor/Speed	Not clear from literature	Visual SLAM	OpenCV	561
CENSURE	Detector	Accuracy	Not widely used/Slow	Visual SLAM	OpenCV	357
KAZE	Detector + Descriptor (Floating Point)	Good results on lower texture surfaces in (on medical example)	Speed comparable to SIFT	Medical Examinations	C++	61
MSER	Detector	Speed, detects homogeneous regions unlike other algorithms. Very good for wide baseline matching	Not used too much in literature in tracking		Matlab	3112
SMD	Descriptor(floating point)	Outperforms(marginal) SIFT on a standard comp vision datasets	Not widely used	N/A (Tested on Mikolajczyk dataset)	N/A	25
CS-LBP	Descriptor (binary)	Small descriptor/Speed, on a subset of cases outperforms (significant) SIFT	Not widely used	Several references to face recognition	Matlab	635
OSID	Descriptor(floating point)	Outperfoms (significant) SIFT for case of illumination changes	Not widely used	References relate to the development of other descriptors	N/A	72
BiCE	Descriptor (binary)	Outperforms(marginal) SIFT on a standard comp vision datasets	Not widely used	References relate to the development of other descriptors	EXE available	44
HRI-CSLTP	Descriptor(floating point)	Outperforms (marginal) SIFT on a standard comp vision datasets	Not widely used	References relate to the development of other descriptors	N/A	57
MROGH	Descriptor(floating point)	Outperfoms (significant) SIFT for some cases	Not widely used	References relate to the development of other descriptors	C++	55
LIOP	Descriptor (floating point)	Outperforms SIFT on a standard comp vision dataset	Not widely used	Standard comp vision dataset	Matlab	104
SYM	Detector + Descriptor (Floating Point)	Urban images containing symmetry	Symmetry requirement may not be valid in our application	Architectural	Matlab	48
Line Context	Detector + Descriptor (Floating Point)	In some cases it outperfoms SIFT	Not widely used	Architectural	N/A	1
PCA-SIFT	Detector + Descriptor (Floating Point)	Shown to be more discrimintative than standard SIFT	Not as widely used as standard SIFT/doesn't work on colour images	Broad spectrum of computer vision systems	Matlab	2769
LDE	Descriptor (floating point)	Small descriptor/ Speed	Not widely used/ Training may not be relevant to pipe imagery	Various computer vision systems	N/A	127
Best DAISY	Descriptor (binary)	Small descriptor/ Speed	Training may not be relevant to pipe imagery	References relate to the development of other descriptors	C++	204
LDAHash	Descriptor (binary)	Small descriptor/ Speed	Training may not be relevant to pipe imagery	SFM	N/A	225
BGM/LBGM	Descriptor (floating point)	Outperforms (marginal) SIFT on a standard comp vision datasets	Training may not be relevant to pipe imagery/Not widely used	References relate to the development of other descriptors	N/A	26
D-BRIEF	Descriptor (binary)	Outperforms (marginal) SIFT on a standard comp vision datasets in some cases	Training may not be relevant to pipe imagery	VIsual SLAM/Odometry	C++	236
SQ-SIFT	Descriptor (binary)	Outperforms (marginal) SIFT on a standard comp vision datasets in some cases	Training may not be relevant to pipe imagery/Not widely used	References relate to the development of other descriptors	N/A	9
BinBoost	Descriptor (binary)	Outperforms (marginal) SIFT on a standard comp vision datasets	Training may not be relevant to pipe imagery/Not widely used	References relate to the development of other descriptors	C++	6

Table 2.2: *Feature Descriptor Comparison*

SIFT was ultimately chosen to be used throughout and a study of its performance and an optimisation of the parameters can be found in Chapter 3.

2.4 Review of Advanced Visual Inspection

In Section 2.2, an overview of visual inspection was given with respect to standard industrial systems collecting mainly just video footage. In this section we will review industrial solutions for 3D mapping and panoramas of pipework as well as those developed within academia.

2.4.1 Commercial Inspection Systems

Systems for pipe inspection and sizing are well established in industrial deployment for a variety of pipe inspection scenarios, this section will highlight some example typical systems.

2.4.1.1 RedZone Snap-On

RedZone Robotics [87] provide pipe inspection systems, mainly designed for inspection of sewer systems/large bore pipes. The system produced by RedZone which will be focused on is the Snap-On Laser system as shown in operation in Figure 2.45.

Figure 2.45: *RedZone Snap-On System mounted on a crawler prepared to inspect a* 300 mm *diameter pipe section*

The system provides ovality measurements of pipes by projecting a laser ring from the attachment. This projection is recorded by the standard CCTV system on the crawler it is being deployed from. The calibration method which provides scale from the extracted pixel values involves attaching a chequerboard ruler to the device, following this the user then manually selects a corner point and enters the corresponding length. The footage is then processed offline producing many metrics about the pipe which has been scanned. An example of the ovality measurement output is shown in Figure 2.46.

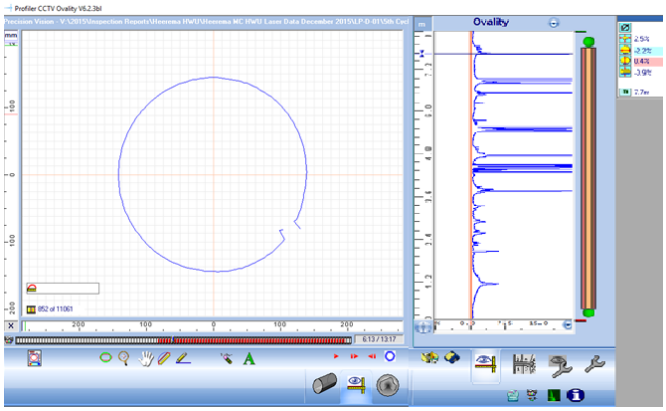

Figure 2.46: *RedZone ovality output, screenshot detailing the measured profile of the pipe and the deviation from a fitted circle*

The work behind the product appears to have arisen from research carried out in [88]. The paper involves imaging of a laser projected in a circle round the interior of a pipe and then constructing this into a 3D model in OpenGL.

The hardware used is a standard robotic crawler with a clip-on carbon fibre laser projector. A video frame captured by the early development is shown in Figure 2.47.

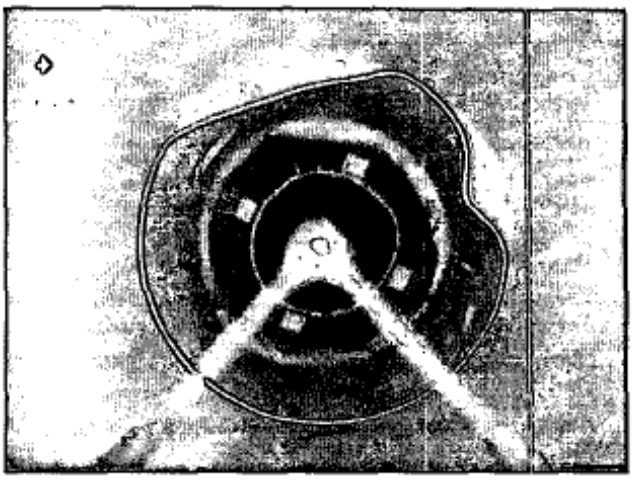

Figure 2.47: *Robotic pipe profiler frame [88]*

The authors utilise the width of the laser beam as the main method of feature extraction, as the intensity peaks in the image caused by the laser are unlikely to have same width as those caused by pipe joins and reflections. An example output is shown in Figure 2.48.

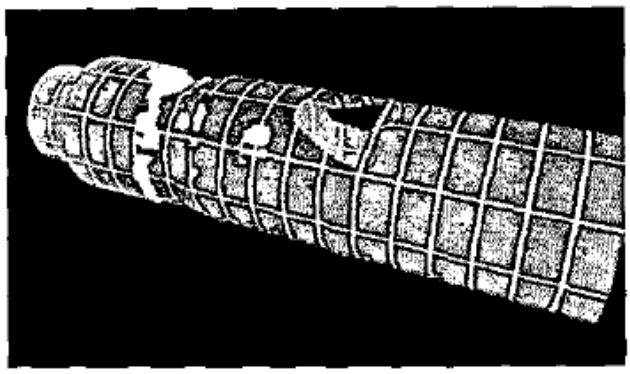

(a)

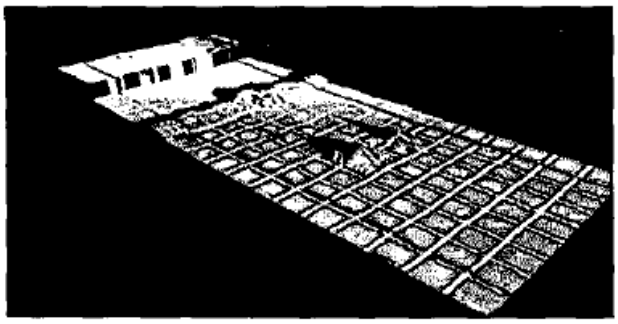

(b)

Figure 2.48: *3D Models of pipe section, (a) shows the model in original geometric form (b) shown the pipe unwrapped [88]*

2.4.1.2 Pure Robotics

Pure robotics [89] are a commercial manufacturer and inspector of large bore pipes and sewer systems (pipes greater than 600 mm in diameter). They have developed a multi-modal modular deployment system which can perform scanning by Light Detection and Ranging (LIDAR), Sound Navigation and Ranging (SONAR) and a laser profiler attachment similar in operation to that shown in Figure 2.45. Renders of the different modular configurations are shown in Figure 2.49.

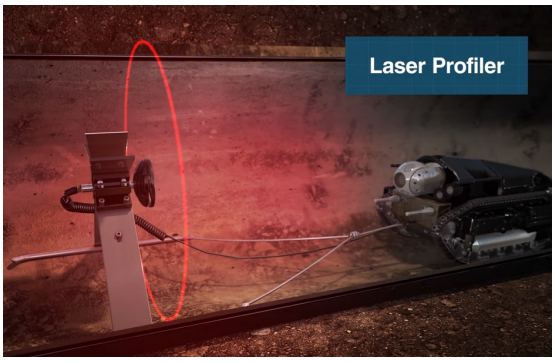

(a)

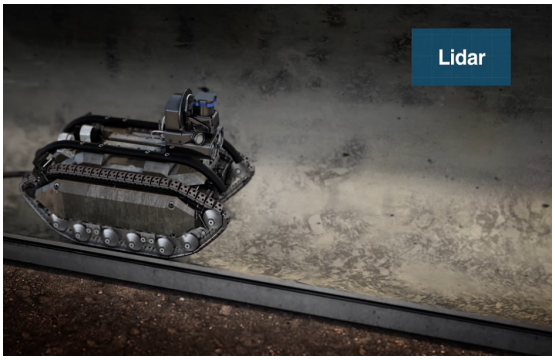

(b)

Figure 2.49: *Pure robotics pipe profiler, (a) configuration for 2D laser profiling with a towed sled attached with a* 360° *laser projector attached (b) configuration for LIDAR [89]*

2.4.1.3 Inspector Systems

Inspector Systems provide a platform capable of providing laser profiling at a smaller diameter than the previous two systems shown with their robotic platform shown in Figure 2.50 and its variants capable of inspecting pipes from 130 mm in internal diameter up to 1200 mm with bends up to 1.5 D. It is stated to have an accuracy of 0.1 mm and capable of sizing defects greater than 2 mm [90].

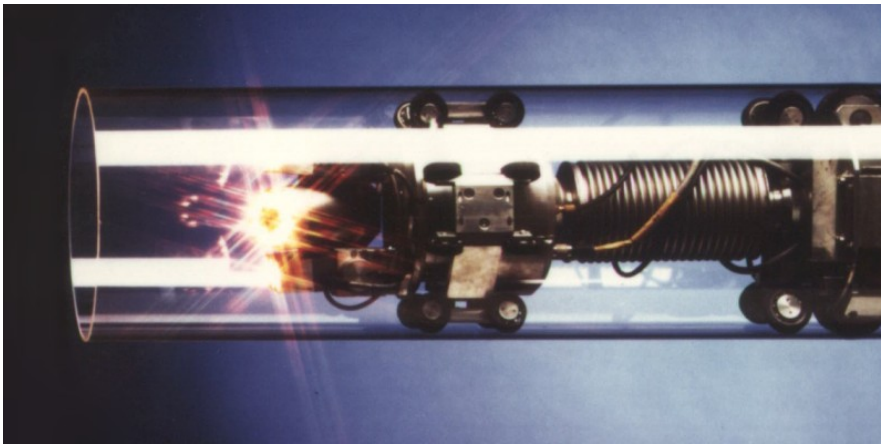

Figure 2.50: *Inspector Systems robot with laser profiler [90]*

2.4.2 Academic Inspection Systems

Projects exist in the academic realm to inspect the interior geometry of pipework at a much smaller diameter than that of products which have made their way into industrial use. The inspection solutions in this category can be split into a number of categories:

- Systems which create high-resolution panoramas to display the internal condition in two dimensions.

- Use of SfM alone to determine the pipe geometry.
- Use of a laser profiler to provide pipe geometry.

2.4.2.1 Panoramic Inspection

By confining a reconstruction to a 2D plane of the inspection surface very high-resolution images can be obtained. These are intuitive to interpret and act as a very effective screening method for surface breaking defects.

In [91] a method for automatically creating 360° panoramic images from RVI footage of gas cooled reactor fuel channels is presented. The inspection is performed by six cameras moving through the channel. These six video feeds are stitched together to form the entire image for the channel. The camera moves at a constant speed enabling a fixed window to be taken from each frame and stitched sequentially. A benefit of this is that it does not require the images to have reliable features which are often in-common within the channels being inspected. Furthermore, the authors leverage the benefits of having multiple cameras viewing the same region of the channels and are able to create stereoscopic images enabling the inspectors to view cracks and features in three dimensions. They are also able to create panoramic images from varying viewpoints which enable the operator to pivot around a point of interest particularity useful to investigate cracks. An example image from their works is shown in Figure 2.51.

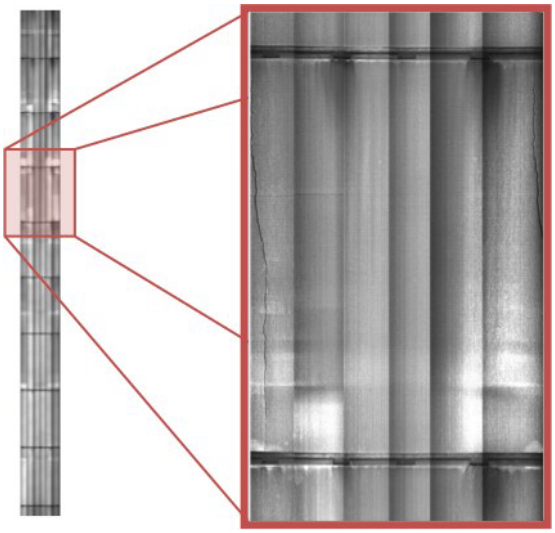

Figure 2.51: *Example panoramic image of a fuel channel [91]*

In a similar methodology the authors of [92] use eight cameras to create what they refer to as "hyper resolution image mosaics" of mine shafts. The authors projected the images taken from each camera onto a cylinder enabling the stitching process, aided by the use of an Inertial Measurement Unit (IMU) to provide a transformation between the local and world coordinates for the camera system. The output provided was again a 360° image of the mine shaft as well as a range image providing depth information. Additionally, the authors provide a review of creating panoramas within the field of mine shaft inspection which appears to be more prevalent to that of pipe inspection.

2.4.2.2 SFM Systems

In a step up of complexity, these systems all use SfM to recreate the geometry of the interior pipe surface to identify defects and localise results from other scanning modalities.

Researchers from the University of Technology, Sydney present a body of work for pipe inspection under a project known as Advanced Condition Assessment and Failure Prediction Technologies for Optimal Management of Critical Pipes with a body of material published covering various modalities of NDE techniques for pipe inspection [93]–[96].

The main research output of interest from the group is [97]. In this work the authors utilise visual odometry which is a method of tracking the position of the crawler through visual markers within the pipework and visual imagery captured by a standard robotic CCTV system (shown in Figure 2.52) to combined with eddy current techniques to provide an in-depth report of a pipes health.

Figure 2.52: *CCTV tool used by Centre of Autonomous Systems [97]*

Extensive work on the topic of SfM was completed by Hansen et al. in 'Visual Mapping for Natural Gas Pipe Inspection'[98]. Their custom platform is shown in Figure 2.53. As shown it consists of a camera with a fish eye lens, computer, LED lighting and motor units for propulsion. Structured lighting was also added to the system in the form of two laser spot projectors to aid in the image re-projection process. The system was trialled on a 400 mm diameter pipe network consisting of straight sections, T-junctions and 90° bends. The authors use a technique known as Sparse Bundle Adjustment (SBA) in combination with priori knowledge of the geometries they expect to locate to generate dense 3D point clouds of the pipe network. The models were all measured to within 1 % of the laser distance estimates.

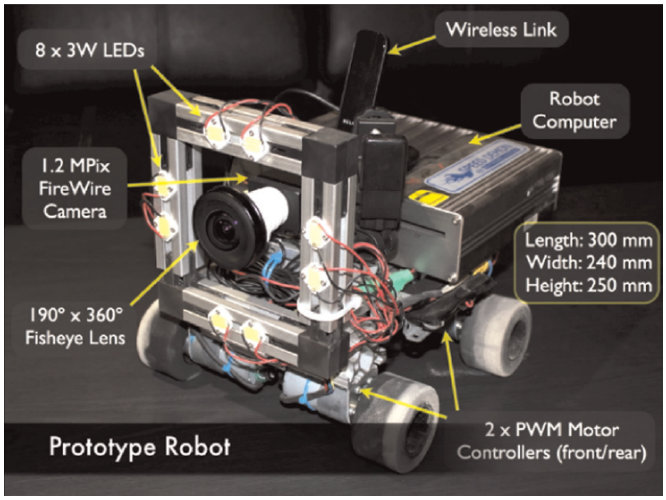

Figure 2.53: *Prototype pipe inspection robot used by Hansen et al. [98]*

It is worth noting that Hansen et al. also experimented with different camera arrangements. The author of this thesis also explores this topic in Section 3.2. The first of their two experimental designs implemented a traditional stereo camera set up shown in Figure 2.54. This gives the authors note that significant periodic

offline calibration would be required to maintain the accuracy of the system and that it would not be suitable with changing inner diameter of the pipes as the field of view would be adjusted. These negatives outweigh the benefits of a fixed image correspondence that the system would bring.

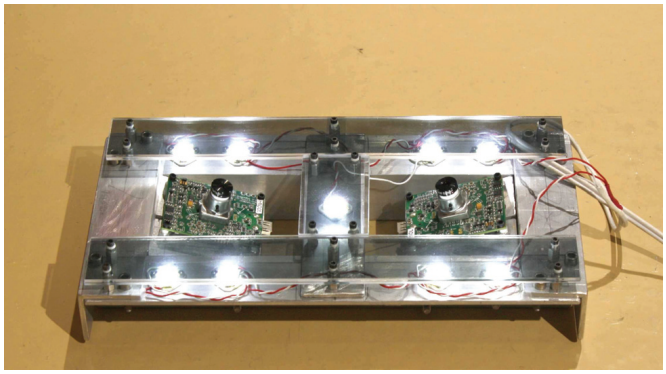

Figure 2.54: *Stereo perspective system designed by Hansen et al. [98]*

The second camera arrangement that was introduced by Hansen et al. was that of a multi camera array with the cameras facing outwards to the pipe wall referred to as a multi stereo capture system. A diagram of this is shown in Figure 2.55, with the benefit of this being that it would be able to image the entirety of the pipe as well as providing fixed stereo correspondence. However, this increases the cost and size of the system greatly. It also increases the challenges of calibration with multiple opportunities for error in each of the intrinsic and extrinsic calibrations. Hansen concludes by noting that the single wide-angle fish eye camera provides the ability to provide full pipe coverage while remaining compact and not requiring relative extrinsic camera calibrations.

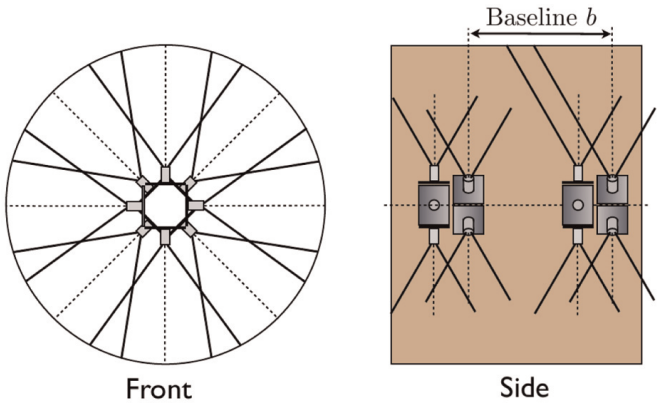

Figure 2.55: *Multi camera stereo perspective system designed by Hansen et al. [98]*

Acosta et al. present a work on 3D pipe inspection designed for sewer pipes between 8 and 32" '3D Pipe Reconstruction Employing Video Information from Mobile Robots' [99]. Their work focuses on two main areas a new motion controller for image capture which was designed to keep the robot travelling in a straight line when encountering sludge and other obstacles. This was achieved with the use of an IMU. For the 3D reconstruction of the pipeline the authors used a SIFT descriptor. The authors performed a study of various different feature detectors and chose to use a combination of Difference of Gaussian and Harris Laplace as it gave the best combination of performance (computation time) and number of matches between images. a sample reconstruction of pipe shows the effectiveness of combining these two detectors in Figure 2.56. Furthermore, pre-processing of the image was undertaken as it was divided into circular regions for sub analysis, each region must contain more than three corresponding points and outliers were eliminated, allowing the authors to overcome poor lighting conditions and feature sparse areas.

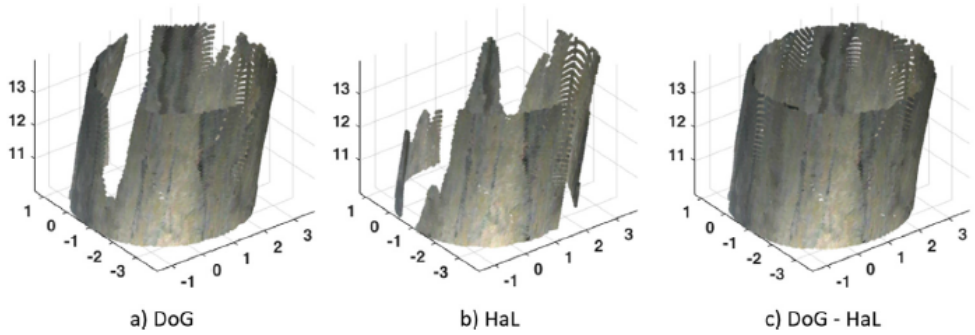

Figure 2.56: *Feature detection impact on reconstruction by Acosta et al [99]*

The authors conclude by comparing their work to available 3D reconstruction software. It is notable that Agisoft [6] has not been included, Agisoft has been shown to be highly effective at reconstructing industrial assets with limited reference points previously [64]. The authors have also often not given a comparable pose of the reconstructed object. Their comparison is shown in Figure 2.57, it is observed that their method significantly outperforms those it was compared to. All of the tools were able to provide a partial reconstruction of the first sample, with Autodesk ReMake and the authors proposed method performing similarly. A similar observation is drawn for the chequerboard sample, although this time the authors method appears to show a more complete reconstruction although the perspective shown differs. The final sample which seems to be sparse in features is shown to have been reconstructed in a much more complete manner than the nearest competing software which was again Autodesk ReMake.

[6] Agistoft https://www.agisoft.com/

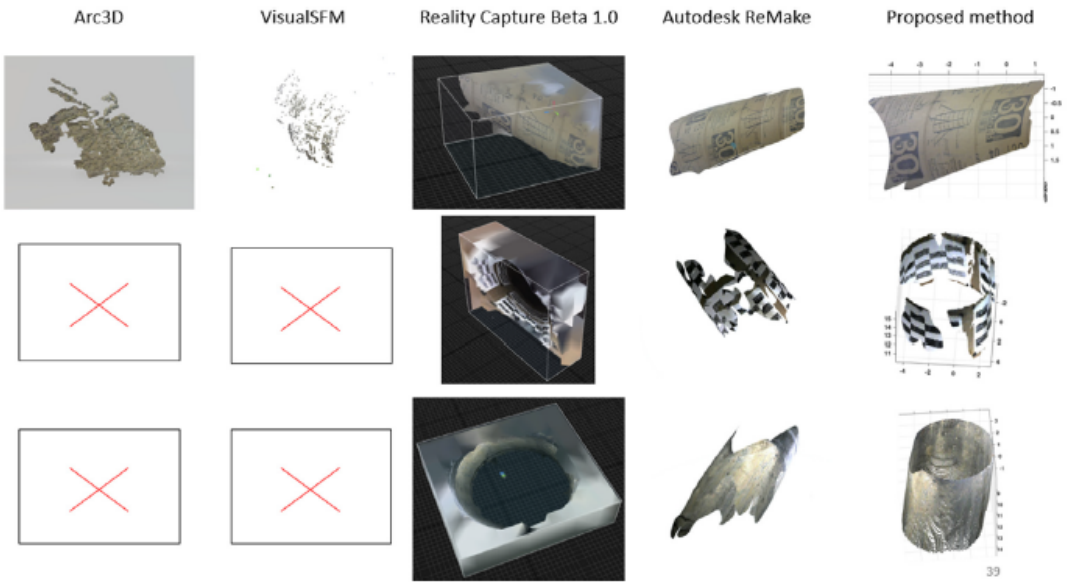

Figure 2.57: *Commercial reconstruction comparison by Acosta et al. [99]*

2.4.2.3 Laser Based Systems

In addition to systems using SfM to determine pipe geometry, there also exists a field of research where a laser profiler is combined to provide accurate measurements of the circumference of the pipe. This is the type of system used by the author so it is useful to understand the differences. It is noted that the calibration of each of these systems covered here will be detailed in Chapter 4.

In 2010 Matsui et al. published '3-D Shape Measurement of Pipe by Range Finder Constructed with Omni-Directional Laser and Omni-Directional Camera'[100]. This was a full 3D measurement system combining aspects detailed in the previous section with a laser profiler. They utilised a traditional camera with a parabolic mirror to capture the full 360° of the pipe under inspection in combination with

an omni directional laser module. The authors used a plane intersection approach to determine the 3D geometry and achieved tolerances of around 3 mm on 285 mm square samples with a standard deviation of around 1 mm. Matsui et al. also utilise SfM to be able to position the laser rings in space thus combining the scale and accuracy that laser profiling provides with the ability to provide 3D measurements of large sections of pipe.

Another use for a laser profiling system was introduced by Tazerjani et al. in 2015, they used a fish eye camera and omni directional laser to determine the pose of a pipe crawling robot in [101]. They were able to determine the pose of the robot in four degrees of freedom. Thus, allowing the authors to provide precise measurement of the defects under inspection as they would be able to use the pose to undistort the 2D fish eye images correctly for. However, the solution requires an initial guess which impacts the accuracy throughout although this may not be a challenge if you have access to the probe at the deployment stage.

In the same year Buschinelli et al. published 'Laser Triangulation Profilometer for Inner Surface Inspection of 100 Millimeters (4") Nominal Diameter'. It uses the same hardware configuration as that which will be presented by the author of this thesis. This configuration consists of a fish eye camera, laser module and conical mirror projecting the laser line onto a pipe surface which it is facing. A considerable advantage of the system presented by Buschinelli et al. is that they utilise a clear joint between the camera and laser module as well as wire with a diameter of 0.08 mm meaning that the image has very little area obscured. This is shown in Figure 2.58, the resulting images which are captured by the system are shown in Figure 2.59.

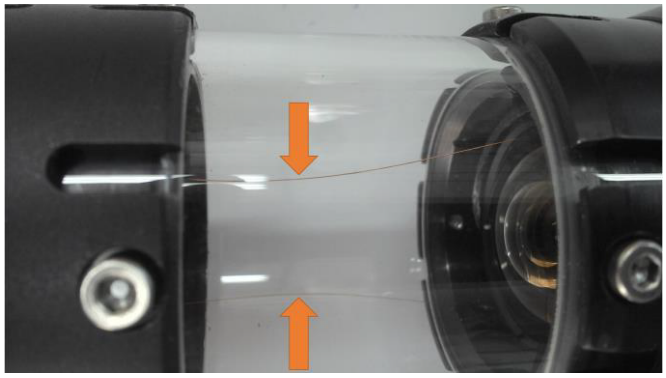

Figure 2.58: *Wiring (*0.08 mm *diameter) and casing utilised by Buschinelli et al. [102]*

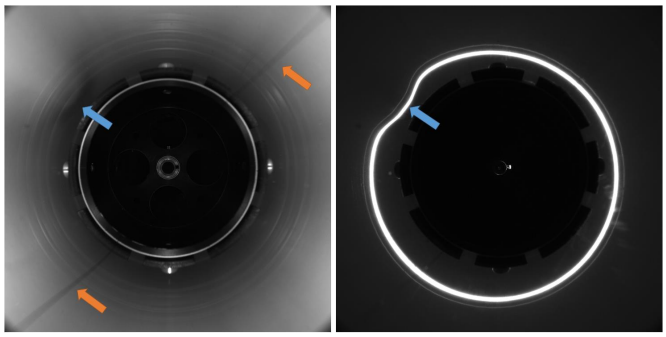

Figure 2.59: *Images captured by laser profiler created by Buschinelli at al [102]*

Work on sewer pipe inspection is introduced by Stanic et al. in [103], [104]. The system was tested on oblong pipes with the large dimension being 600 mm in diameter. The maximum error they noted for these measurements was 7 mm. Their system is rather unique in design in that it consists of the standard camera and laser profiler combination but on the back of the unit exists another camera and board used in conjunction with a static laser unit to determine the position of the system within the sewer, this is shown in Figure 2.60.

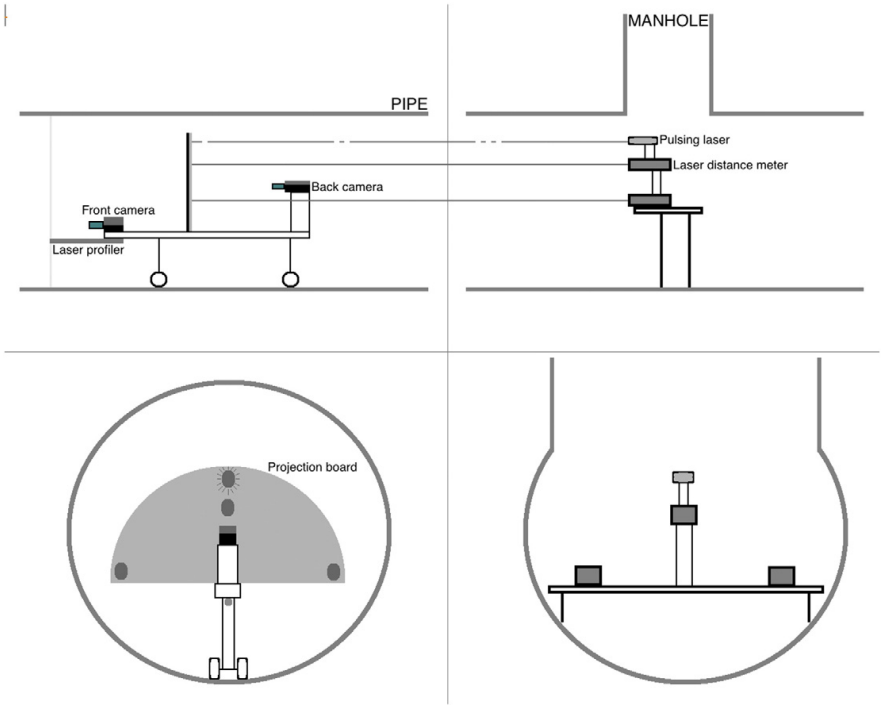

Figure 2.60: *Schematics of the system used by Stanic et al. [104]*

Jin et al. [105] developed a system for measuring the diameter of pipes as a non-contact metrology method, it used the standard camera, laser and mirror combination. They detailed methods for finding the intersection of the laser plane and object under inspection which if not in line with the probe would result in an ellipse. The method would then calculate the semi major and minor axis of the ellipse and resolve the equivalent circle as the system was designed to work on perfect cylinders. They conducted tests on two pipe samples with diameters of 44.07 and 50.07 mm. Their system was able to measure these as 44.06 and 50.90 mm respectively.

Many of these systems include a glass or plastic tube linking the camera module to laser projector. He et al. introduces a method for calibrating the system to take account of the refraction that will occur to improve the accuracy of the system in 'Measurement Model of the Omnidirectional Structured-Light Vision and Its Calibration Method' [106]. They provide a diagram of this refraction, shown in Figure 2.61. The correction they applied was able to reduce the Root Mean Square (RMS) errors on a 286 mm diameter pipe from 2.04 mm to 0.23 mm.

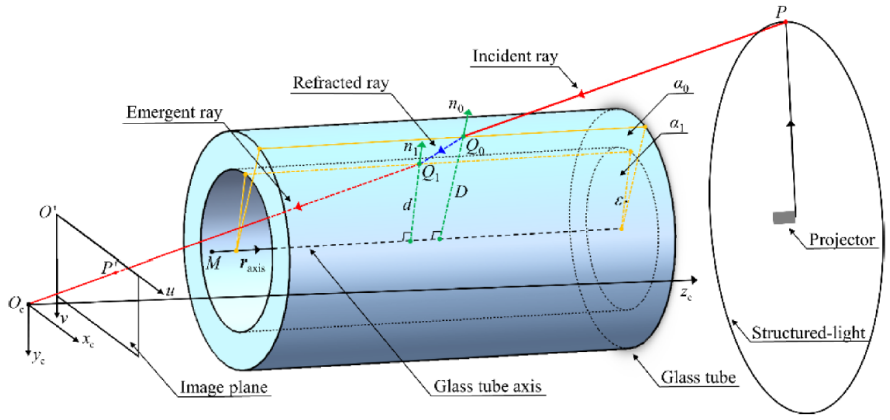

Figure 2.61: *Model of laser profiler detailing refraction by He et al. [106]*

2.4.3 Summary of Advanced Visual Inspection

In this section we reviewed various methods for providing additional information from inspections carried out by RVI.

These were divided into three categories, stitched image panoramas, SfM based reconstructions and laser-based reconstructions. These each comes with their advantages and disadvantages, greatly determined by the level the problem is constrained to. This varies greatly across these three methods which impacts their

ability to be applied in varying conditions. For instance, the panoramic image stitching solutions presented provide arguably the highest resolution images for visual inspection as well as offering three-dimensional information, in the cases where they have utilised multiple cameras as in [91], [92]. They were however bound to straight cylindrical inspections. This in the case of [91] allowed for the inspection to carry out accurate stitching of the images in the absence of feature rich environment. For the use of SfM for pipe work inspection [98] provides extensive information, they however introduced the constraint of a cylinder to refine their results. [99] highlights the difficulties of unconstrained SfM for internal pipework inspection using commercial software in Figure 2.57. This may be down to a large number of factors encountered such as the views being largely parallel to each other along the axis of the pipe leading to poor reconstruction as illustrated in Figure 2.28. As well as the previously mentioned issue of feature sparse environments. To allow for accurate 3D reconstruction which are generally agnostic to the challenges of varying environmental conditions (lighting, surface finish etc.), laser-based systems may be utilised. These systems were shown to be available within industry with a preference for larger diameter pipe as well as a range of solutions presented within in academia. Most of the challenge moves from the environment to the calibration and design of the laser system which presents one of the greatest factors in the determination of the accuracy from the laser reconstruction.

For these reasons the wider project utilising the probe used throughout this thesis uses a combination of sensor modalities to constrain the problem and provide an optimum result in a compact form factor. With the use of a laser profiler 3-

Dimensional information is able to be captured accurately in varying conditions with a proven calibration technique detailed in Chapter 4 and a constrained panoramic image stitching method optimised in Chapter 3 and presented as a fully developed industrial demonstrator in Chapter 5.

Chapter 3

Hardware and Inspection Parameter Development

3.1 Introduction

A number of systems to inspect pipework have been presented in in Chapter 2. This chapter will focus on defining the system used by the author for their research and the benefits it provides when compared to traditional Remote Visual Inspection (RVI). Following on from the overview of the probe, a section is presented on the optimisation of the camera lens and the camera laser geometry within a simulation framework. The accuracy of the system over a wider range of pipe sizes was observed to increase as the baseline increased, and the accuracy also improved with a theoretical arrangement of multiple pinhole cameras. The advantages and disadvantages these changes would bring to the system are discussed in detail such as the reduced bend radius the probe could navigate with a larger baseline distance. Concluding the chapter prior to the summary is a practical

study of the camera parameters and Scale-Invariant Feature Transform (SIFT) parameters. Each of the parameters is studied and optimised to provide the ideal settings for inspections.

3.1.0.1 Laser Profiling

To obtain a dimension for the pipe wall, a laser profiler is used which consists of the fisheye camera, and a laser ring created by projecting a laser diode onto a conical mirror, originating from a fixed distance away for the camera centre. Triangulation is then used to calculate the position of the observed laser ring in three-dimensional space.

The geometry of laser projector and camera is shown in Figure 3.1. Where, r is the pipe radius, θ describes the angle between the central axis and the imaged ray, $\mathbf{P_w}$ is the point in space where the laser intersects the pipe wall, $\mathbf{P_m}$ is the point on the unit sphere (a representation of vectors entering the camera centre at one unit distance) where this point is imaged and α which is the opening angle of the laser reflected by the conical mirror. The baseline is the distance between the origin $\mathbf{O}$ and the point of reflection. It can be observed from the model that once the values of the baseline and opening angle (α) are known for a given point on the unit sphere ($\mathbf{P_m}$), the corresponding point $\mathbf{P_w}$ can be calculated through triangulation. This is in more detail in Chapter 4 Section 4.7. Furthermore, in Chapter 4 Section 4.3 alignment error of the conical mirror will be discussed - i.e.

for the case where the opening angle $\alpha \neq 90°$. To calculate $\mathbf{P_m}$ from a given pixel on the image the camera model which is described in Chapter 2 Section 2.3.1.2 is used.

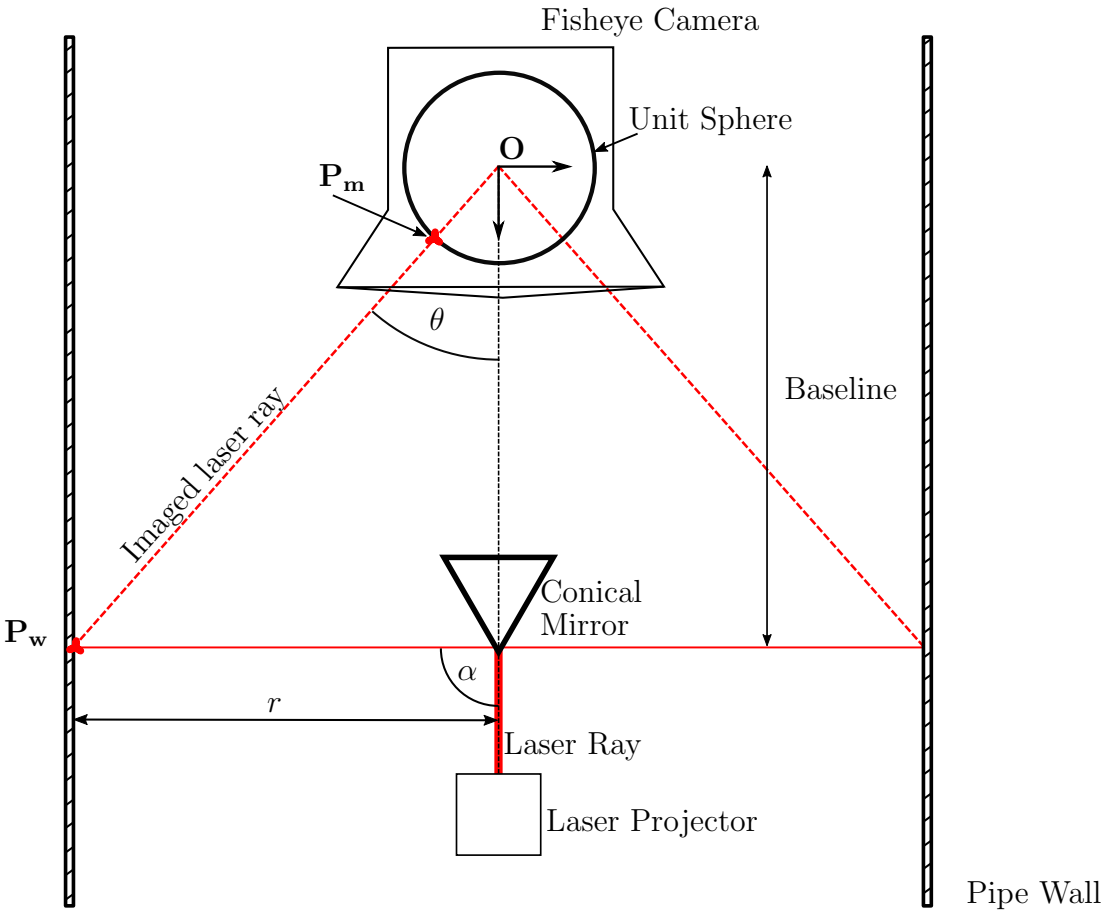

Figure 3.1: *Camera and laser profiler geometry*

3.1.1 Image Stitching & Pipe Profiling Tool

The RVI system consists of a laser profiler and omni-directional camera unit arranged as the schematic shows in Figure 3.1. A photo of the probe and semi rigid deployment reel and flexible deployment cable are shown in Figure 3.2.

Figure 3.2: *Image stitching & pipe profiling tool for pipe inspection alongside deployment reel and flexible cable*

A labelled image of the probe and schematic are shown in Figure 3.3 and Figure 3.4 respectively.

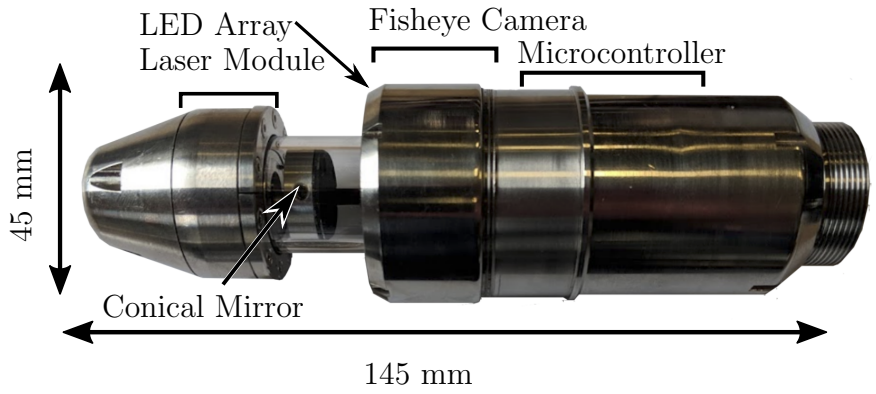

Figure 3.3: *Camera and laser profiler with subsystems highlighted*

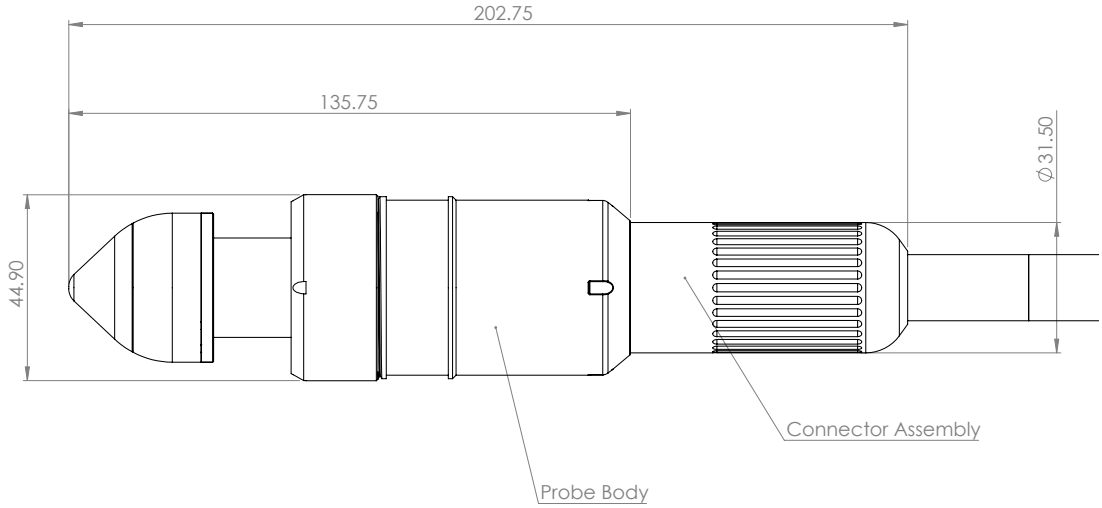

Figure 3.4: *Technical drawing of the camera and laser profiler*

It combines laser profiling with visual reconstruction, using Visual Odometry (a method for obtaining relative pose from a series of images) for probe localisation and the captured images to provide high resolution stitched images of the interior. The laser profiler is utilised for accurate geometric reconstruction in challenging conditions. The combination of these two elements provide great insight into the asset under inspection.

The probe was initially designed to meet the IP67 [107] rating, this rating ensures the system is protected against dust ingress and the effects of temporary immersion between 150 mm and 1000 mm for a minimum duration of 30 minutes. As part of meeting this requirement the probe had a sapphire window enclosing between the nose cone and body shown in Figure 3.3 and Figure 3.4. However, this window reduced the quality of the images due to multiple factors such as reflections from the LED Array onto the window. Therefore, for the majority of this work the probe was used without this sapphire window, in its place was an aluminium linkage to attach the nose cone to the probe body. A section covering the results obtained with the sapphire window is shown in Section 5.2.

This system was developed during a collaborative Innovate UK project [108]. During this project there was a focus on a Structure from Motion (SfM) (which can infer both the camera pose and structure from the images) based approach for reconstruction which whereas the work presented by the author simplifies this down to Visual Odometry for speed and robustness in feature sparse inspection environments. The topics of SfM & Visual Odometry are covered in more detail in Chapter 2. Previous published work under the project which may be of interest to the reader includes: 'The Influence of the Spatial Distribution of 2-D Features on Pose Estimation for a Visual Pipe Mapping Sensor'[109], which as the title suggest studies the influence of the distribution of features within the pipework under inspection and the impact this plays on pose estimation and therefore, reconstruction accuracy. Furthermore, a series of conference papers were presented [110]–[112] which provide an overview of the system, its role, functionality and an error model which is expanded in Chapter 4.

The work presented in the following sections of the thesis (beginning with the simulation environment) were led by the author but wouldn't have been possible without the collaboration of partners within the Innovate UK project, areas of work where significant collaboration took place are made clear in the text.

3.1.1.1 Overview of Operation and Benefits

During inspection of internal pipework, the probe alternates between an LED image and a laser image. The illuminated LED image captures the texture and features, which are used for tracking the position of the probe within the pipework. The laser images provide direct geometric information, example images captured by the probe are shown in Figure 3.5.

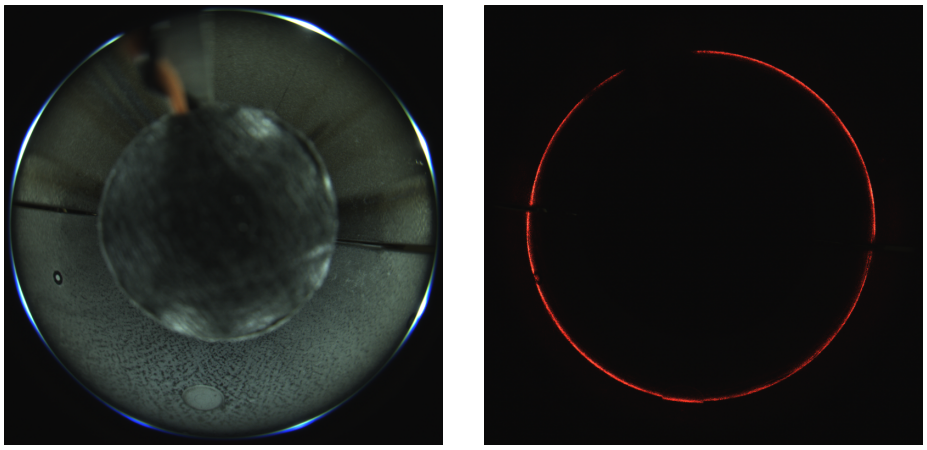

(a) **(b)**

Figure 3.5: *Example images taken with the probe in a split pipe sample with a flat bottom hole: (a) shows the images under LED illumination and (b) shows the projected laser line*

The laser image is used to profile the interior of the pipe under inspection, while the probe projects a laser line onto the circumference of the inner pipe wall and images this while being driven through the pipe. These images are then used to determine the geometry of the pipe and thus detect surface defects such as surface breaking cracks and pitting as well as providing information on geometric defects such as large areas of corrosion. In a single image 360° of the pipework is imaged, for 75 mm radius pipe around 100 mm along the axis of the pipe is visible. This leads to quicker inspections, as traditional video probe footage may need to be repeated with the probe at multiple orientations within the pipe to ensure full coverage.

3.1.1.2 Hardware Overview

The hardware was developed during the Innovate UK project by Wideblue Ltd. The final prototype is shown in Figure 3.3. It consists of three main components:

1. Gigabit Ethernet (GigE) camera unit manufactured by Flir with the following specifications:
   Camera Model Number: BFLY-PGE-50A2C [113]
   Resolution: 1700 x 1700 pixels (cropped from usable resolution with lens used)
   Frames per Second (FPS): 13
   Shutter: Global
   Lens: Sunex DSL216 Fisheye 187° Field of View (FOV) [114]

2. A microcontroller (MSP430G2553 [115]) is used to control the operation of the camera modes and provide synchronicity between the image capture and the LEDs & laser line projector. Allowing for three modes of data capture: LED illuminated, laser line or alternating LED & laser line illumination. On-board Inertial Measurement Unit (IMU) data is also streamed from the microcontroller providing orientation information.

3. The laser module and conical mirror which projects the laser line onto the object under inspection. The conical mirror is machined precisely to project the laser at 90° which when illuminated by the laser module projects the laser into a plane thus when inside a pipe creates a 360° ring.

3.2 Simulation Environment

To analyse the probe in a simulated environment, a MATLAB interface was created, to allow various parameters of the camera and laser profiler configuration to be studied precisely and in complete isolation. Thus, insight will be gained on the impact of various design parameters on the laser line re-projection accuracy of the system. The initial framework of this providing a camera, cylinder and laser projector were previously developed and built upon extensively to enable the work presented in this section. This is used to examine three main design parameters of a laser profiling system:

1. The length of the baseline i.e. the separation from the camera centre to the laser projector.

2. The lens used to image the ring for example, fisheye vs wide angle lenses with varying focal length.

3. The use of multiple cameras to image the laser ring.

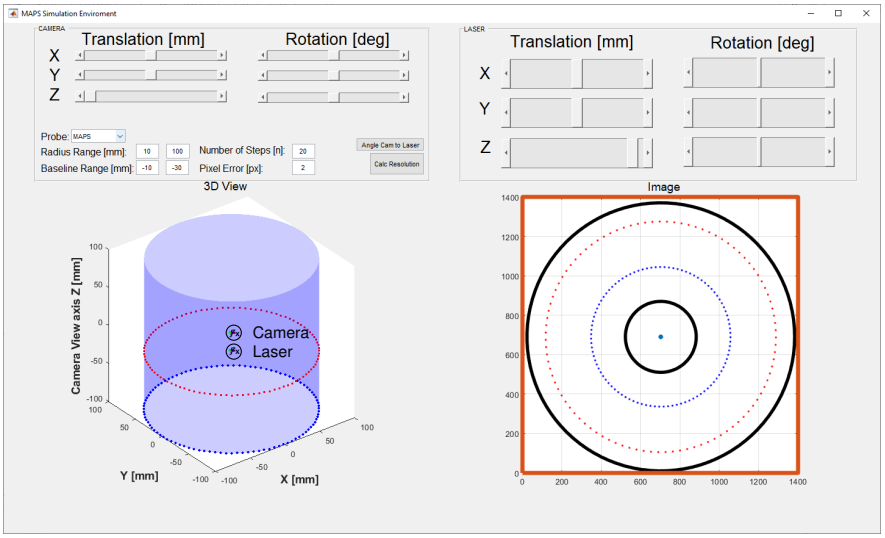

Figure 3.6: *MATLAB based camera and laser profiler simulation environment*

The simulation allows the user to move the camera & laser module within 3D space relative to points of interest, in the case shown a pipe with a radius of 100 mm. The intersection of the projected laser ring and pipe can be calculated and imaged with a known camera model. Currently the simulation allows for the use of fisheye models utilising the Scaramuzza tool box [17] and the standard pin hole model with the use of the MATLAB computer vision tool box [116].

There are differences in the pin hole model and fisheye model that have a simple solution but these differences should be clarified. The description of these are aided by the model given by Scaramuzza in Figure 3.7.

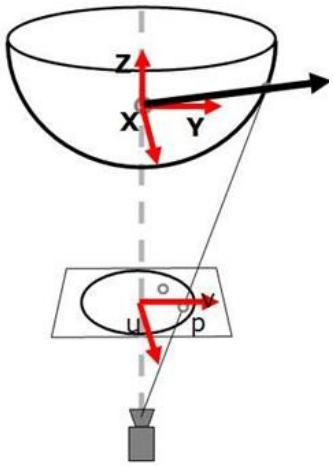

Figure 3.7: *Ocam camera model schematic [17]*

From this it is clear that although the camera is looking forwards in the Z axis it images a mirror thus it is in fact looking behind it. For this reason, the laser ring is positioned below the camera. This solution was found to work well for the Ocam fisheye model [18]. When using the MATLAB pinhole model however, the camera is not imaging a mirror so it is not able to image laser ring. To compensate for this a transformation is applied to the MATLAB camera position such that it is imaging the scene the same way as the OCam fisheye camera.

It is noted that the Y-Axis of the camera will now be reversed (this is stated in [17] when using a fisheye camera) but all changes to the system are only applied to the Z & X-Axis so this will have no impact on the results.

The process for simulating the laser profiling is described in the following steps:

1. Create a transformation matrix representing the camera in space:

$$[\mathbf{R}_{\text{Cam}}|\mathbf{t}_{\text{Cam}}] = \left[\begin{array}{ccc|c} r_{1,1} & r_{1,2} & r_{1,3} & t_1 \\ r_{2,1} & r_{2,2} & r_{1,3} & t_2 \\ r_{3,1} & r_{3,2} & r_{3,3} & t_3 \end{array}\right]$$

2. Create a transformation matrix representing the laser module in space:

$$\mathbf{R}_{\text{Laser}} = \text{diag}\,(1, 1, 1)$$

$$\mathbf{t}_{\text{Laser}} = \mathbf{t}_{\text{Cam}} - [0, 0, \text{Baseline}]^{\mathsf{T}}$$

3. Create a cylinder aligned with the Z axis of the world coordinate frame within this space, defined by two $\mathbb{R}_{3x1}$ vectors representing the cylinder start and end as well as the radius r.

4. Project a number of lines at 90° from the laser module (i.e. along the $x - y$ plane), calculate the intersection points between these lines and the cylinder).

5. Multiply these extracted points by the inverse of the camera translation matrix ($\left[\begin{array}{c|c} \mathbf{R} & \mathbf{t} \\ \hline \mathbf{0} & 1 \end{array}\right]^{-1}$) to move them into the cameras reference frame.

6. Use the appropriate camera model to project the 3D coordinates onto an image as overviewed in Section 3.1.0.1 and detailed in Chapter 4.

There are many advantages of being able to simulate the camera, laser and environment, for instance the prototyping of the method used to determine the precise camera pose shown in Chapter 4 and the ability to determine the accuracy of a system.

Throughout the study, a measurement error of two pixels was used as a reference value. This value was calculated as double the median error (for errors rounded up to the nearest integer value) between the pixel distances of a fitted circle on a calibration image from Chapter 4. This image was known to be a perfect circle. The method to determine the laser pixel to extract and point on the fitted circle is shown graphically in Figure 3.8. It is noted that the error is likely to vary with changes in camera resolution and also be impacted by radii much larger or smaller than the 30 mm radii it was derived from, however for the purposes of this study it is fixed to allow direct comparison of changes in other aspects of the system, mainly the baseline and lens/lenses used in the system.

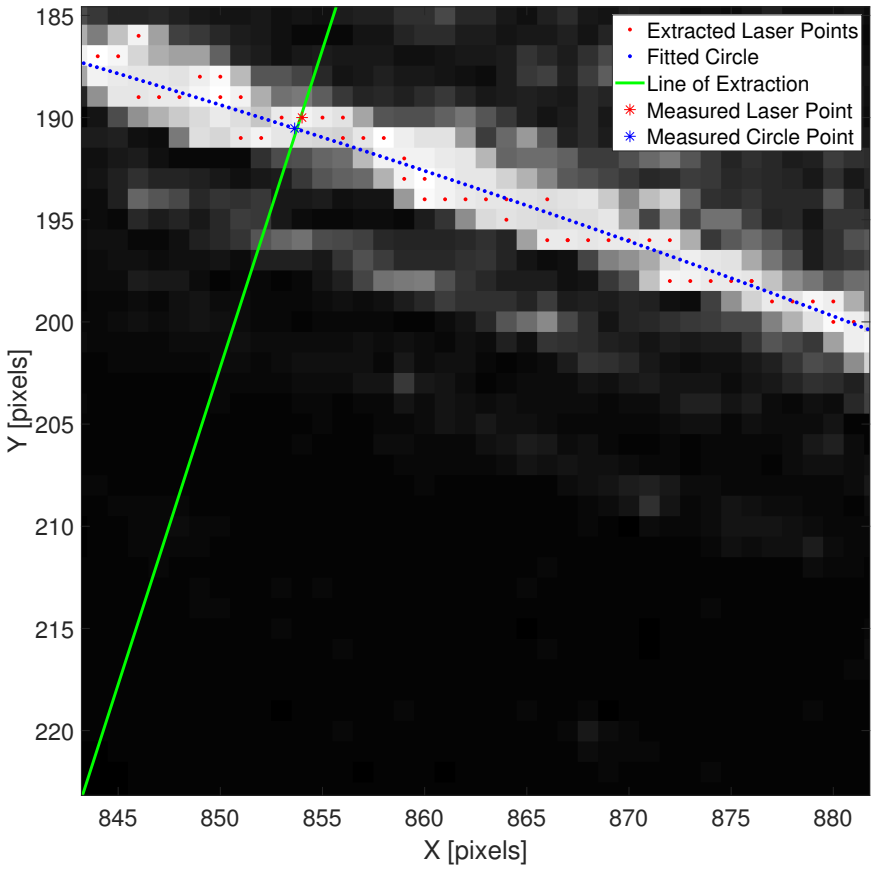

Figure 3.8: *Measurement of pixel extraction error*

3.2.1 Baseline Length Study

A study of the baseline was undertaken to determine the impact which it has on the accuracy of the system with a known error in the reading of the location detected laser point on the image plane. I.e. $p_{\text{error}} = p_x + e_x$ where the p_x is the exact 2D coordinate of the pixel imaging the reflected laser and e_x is the desired amount of mis-measurement to add to the system. The investigation of

the system shown in Figure 3.3 is carried out with an error in reading of 2 pixels. The error is shown for a single point on the laser, and the simulation was carried out on a range of the pipe radii from 10 - 150 mm.

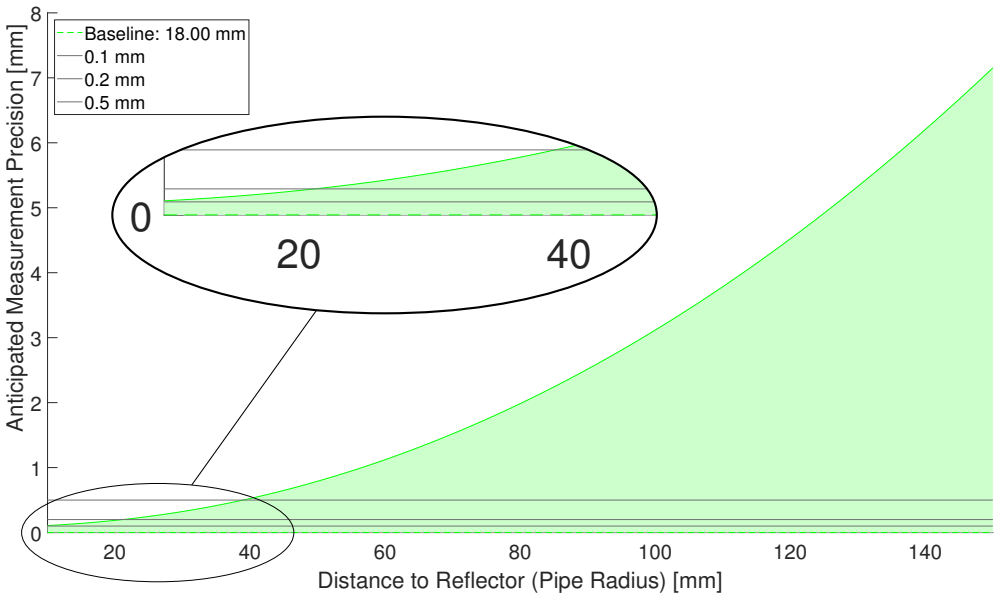

It is observed that the probe meets the criteria of achieving 0.5 mm accuracy for its designed pipe radius of around 45 mm. However, past this point the error increases exponentially. To use the system on larger radii pipe and maintain the accuracy within an acceptable range, future changes must be considered.

Increasing the distance between the laser module and the camera (baseline) can reduce this error as with a larger baseline the pixel related to the imaged laser ring is moved towards the camera centre. Towards the centre of the camera the relationship between the distance in pixels from the camera centre and bearing angle is more linear leading to error in this region having less impact on the result. The figure below is shown with a varying baseline of 18, 59 and 100 mm. At 100 mm the 0.5 mm error point has increased to a diameter of 4.3 inches

(110 mm). This is not without its own costs as the bend radius the probe would be able to manoeuvre would be significantly reduced as the probe length would increase by approximately two-thirds.

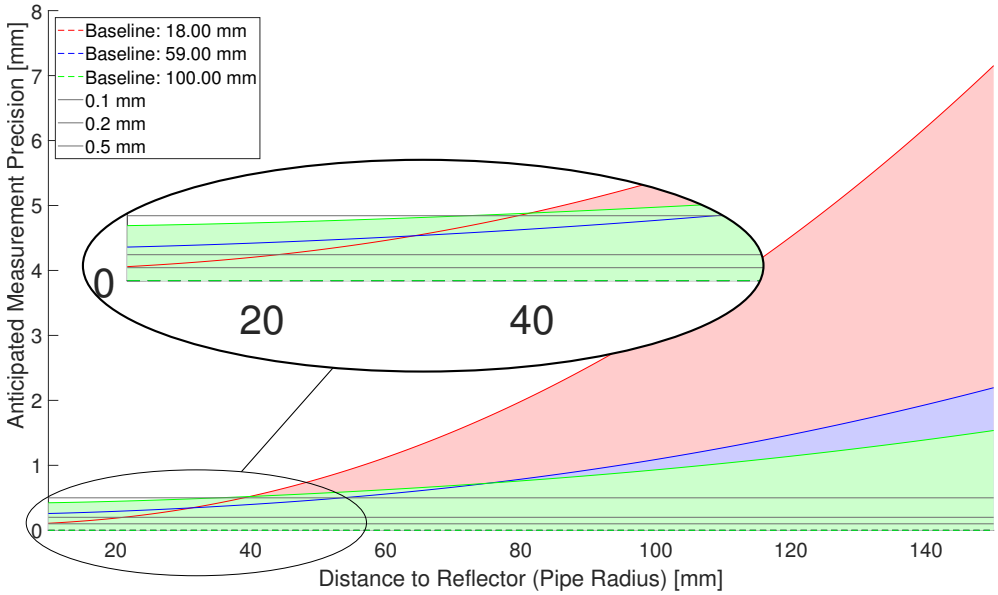

Figure 3.9: *Measured error due to a pixel extraction error of two pixels for radii of 10* - 150 mm *with baseline values of 18, 59 and* 100 mm *with fisheye lens*

3.2.2 Introducing Variation of the Camera Model

In this section, the use of lenses with a field of view much less than that of the fisheye lens used thus far will be investigated. In this first case a 3.5 mm focal length lens which when paired with the 8.8 mm x 6.6 mm sensor results in a horizontal field of view of 98° and a vertical field of view of 88°. These values are calculated from the intrinsic values given by the MATLAB camera calibration [116] and the camera sensor specifications detailed previously (Item 1). The viewing angle is drawn for the system inside a 20 mm radius pipe in Figure 3.10a.

The accompanying 2D projection onto the image is shown in Figure 3.10a. It is clear from these images however, that even at this relatively small pipe radius with a baseline of 18 mm the system cannot image the full laser ring.

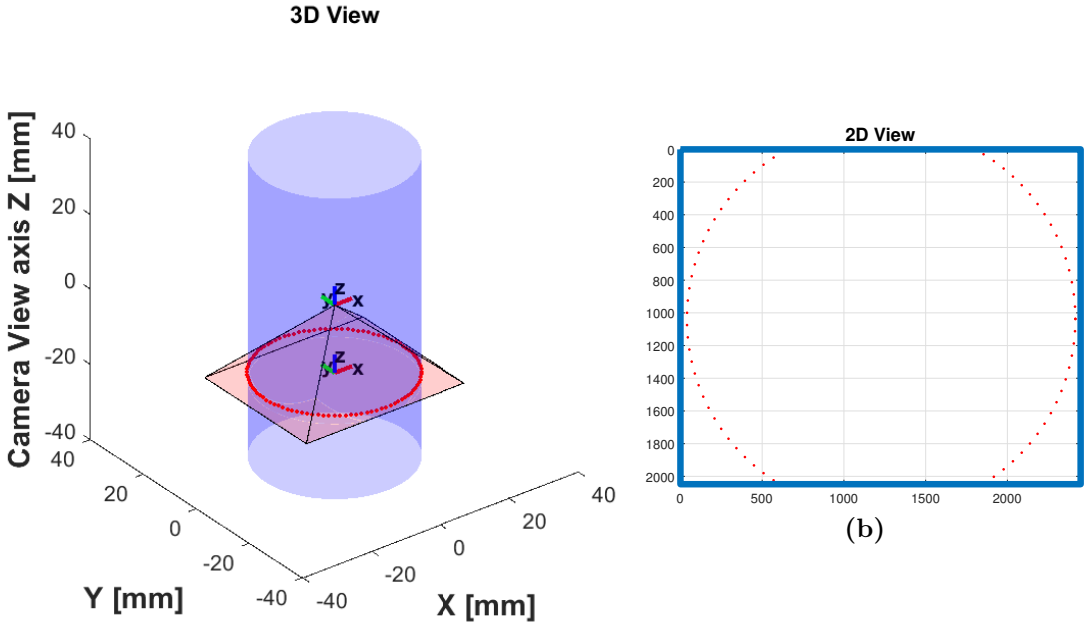

Figure 3.10: *3D (a) and 2D image (b) of the system within a* 20 mm *radius pipe with a baseline of* 18 mm *and a* 3.5 mm *focal length*

For the same ranges of baseline and radii as shown previously (18 - 100 mm & 20 - 150 mm respectively) the two-pixel error when using the 3.5 mm focal length lens is shown in Figure 3.11. Due to the linear nature of the camera model, a flat error is given throughout. However, this is not without its own downsides as the laser ring is not visible to the camera through much of the desired measurement range without increasing the baseline significantly. Similar systems such as the [87] for this reason have large baselines and extensions available for larger diameter pipes. Another downside to this is that the system, when designed with the fisheye lens

was able to provide a 360° image of the pipe wall which is essential for the image stitching and visual odometry which can be thought of as the other half of the system.

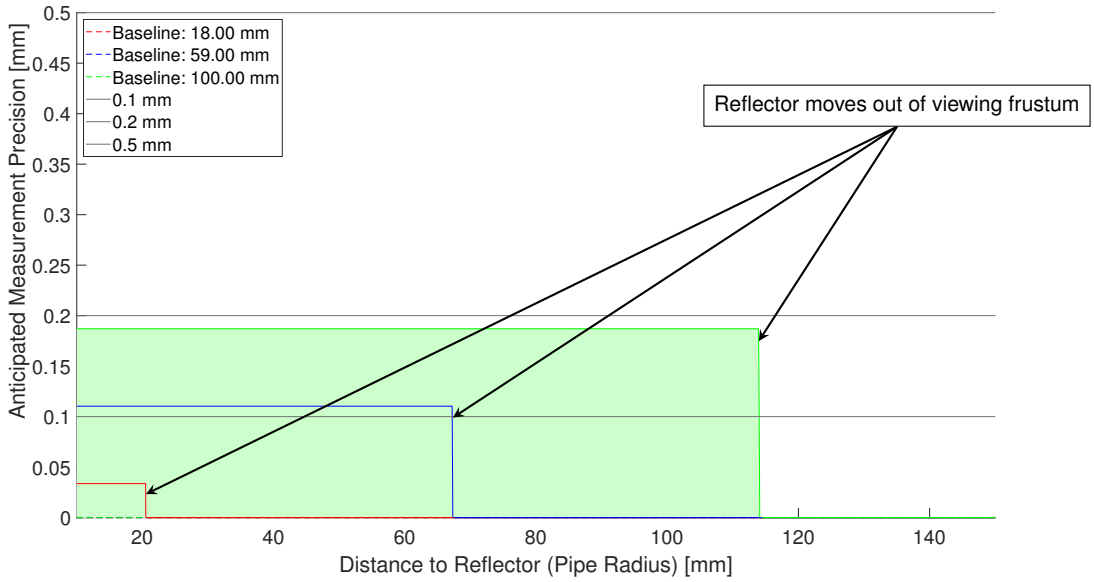

Figure 3.11: *Measured error due to a pixel extraction error of two pixels for radii of 10* - 150 mm *with baseline values of 18, 59 and* 100 mm *using a* 3.5 mm *lens*

For these reasons, another design option is presented to inspect large bore pipes while maintaining the 360° imaging capabilities. This design utilises an array of cameras each fitted with a wide-angle lens to provide the field of view required to inspect a suitable range of pipe diameters. A simplistic method of setting the angle these cameras would face from the central axis would be to specify a nominal pipe diameter that you wish to inspect, set a baseline and then angle the camera such that the laser line is imaged on the central pixel. In the simulations and models shown the physical body of the camera will not be considered, it is assumed they can all occupy the same space to simplify the simulation. An

example is shown for a baseline of 18 mm inside a pipe with a radius of 50 mm. The lens used in this example has a focal length of 3.5 mm and provides full coverage of the laser ring and pipe wall when part of an array of four cameras angled using the previously described method. This is shown in Figure 3.12.

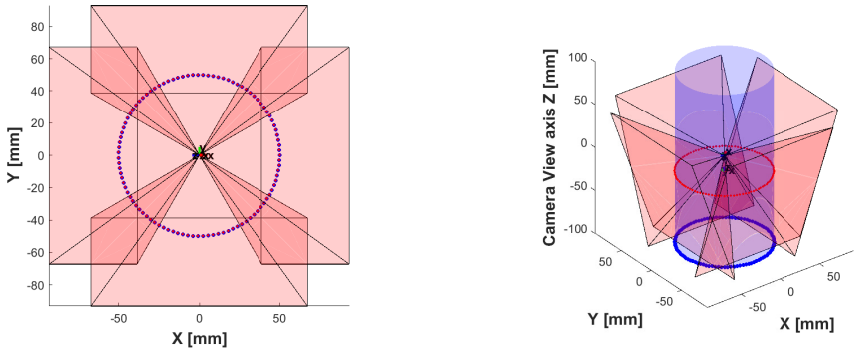

(a) **(b)**

Figure 3.12: *2D and 3D perspectives of a multi-camera system,* 3.5 mm *focal length,* 18 mm *baseline and* 50 mm *radius*

Full coverage cannot be assumed and care must be taken to ensure this is achieved as when simulating the 8 mm focal length lens, full coverage of the laser ring and pipe wall is not achieved within this size pipe (50 mm radius) as shown in Figure 3.13.

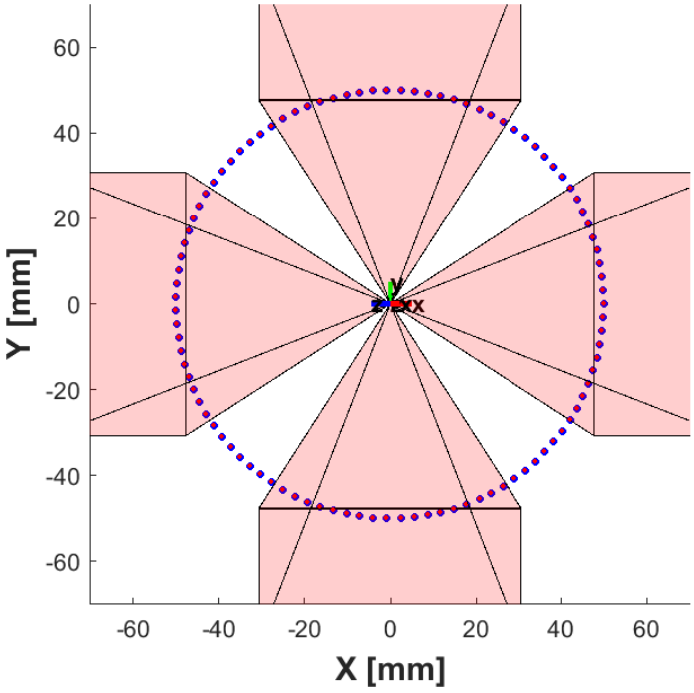

Figure 3.13: *2D perspectives of a multi-camera system,* 8 mm *focal length,* 18 mm *baseline and* 50 mm *radius*

The observed error curve is no longer linear in nature due to angular nature of the camera. The resulting error for the 3.5 mm & 8 mm focal length multi-camera arrangement is shown in Figure 3.14.

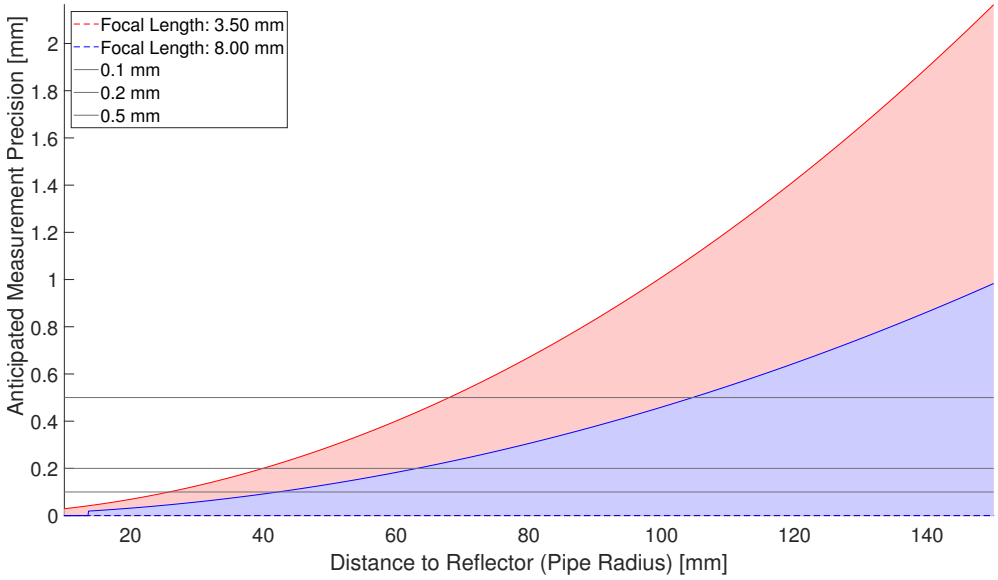

Figure 3.14: *Measured error due to a pixel extraction error of two pixels for radii of 10* - 150 mm *with a baseline of* 18 mm

Accuracy is increased significantly when compared to the original design with an extensive peak error reduction. The costs and difficulties associated with this camera array however, would be considerable. Therefore, for larger pipes it would be deemed most sensible to follow the examples set by industrial systems and use a wide-angle lens in combination with a larger baseline. This allows for high accuracies and with a larger baseline a significant range of pipe sizes may be inspected, allowing for inspection of up to 114 mm radii pipes. furthermore, increasing the baseline to 200 mm allows for an increased pipe size of 228 mm with an error of 0.38 mm.

3.3 Optimising Parameters for Inspection

3.3.1 Introduction

In order to obtain the best results for an inspection the parameters used must be considered, and will be discussed in this section.

These fall into three main categories:

1. Camera settings:
    - Image Resolution
    - Exposure Time
    - Frame Rate
2. Deployment speed
3. SIFT parameters for feature extraction

Each of these are inter-linked and impact on the results in unison. They will for practical reasons however, each be individually explored in the following section with references made to the other parameters throughout. This allows perspective to be maintained and keeps the optimisation reasonably constrained. With the aim of the optimisation is to provide consistent and high-quality results in varying conditions, as well as minimising processing time to enable real-time inspection.

All of the studies were carried out within a 45 mm stainless pipe section with no external lighting, the lighting conditions were determined by the LED illumination array onboard the probe. The sample pipe used was representative in both diameter and surface finish as those the inspection was targeted for. The experimental set up used for the study is shown in Figure 3.15.

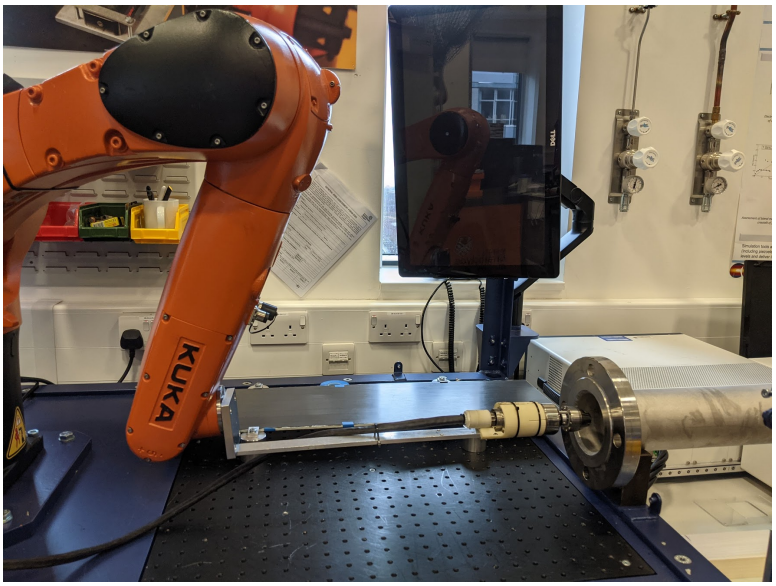

Figure 3.15: *Robotic manipulator, used to precisely control the deployment speed of the probe through a section of pipe*

Adjustments to the parameters will be required to account for changes in pipe diameter and surface finish in other inspection scenarios. The work presented in this section will act as a starting point and provide guidance on the outcome of varying each parameter to reduce the time taken to revise the settings into a new optimum.

3.3.2 Parameter Optimisation

The available parameters and descriptions are shown in Table 3.1.

		Description
Camera		
Exposure Time	Optimised	Amount of time sensor is exposed to the scene
Gain	Fixed	Amount of gain (multiplication) applied to the image
White Balance	Fixed	Adjustment of colour balance
Gamma	Fixed	Correction applied to pixel intensity
Resolution (scaling)	Optimised	Output image size
Deployment		
Speed	Optimised	Deployment speed of probe through pipe sample (assuming constant rate)
SIFT Extraction		
Contrast Threshold	Optimised	Threshold value to filter low contrast features
Edge Threshold	Optimised	Threshold value to remove features which are likely to be edges
Number of Octaves	Optimised	Number of octaves to process
Sigma	Optimised	Amount of blur between images in each set/octave
Scales	Fixed	Number of images within each set/octave

Table 3.1: *Parameters to be optimised and their description*

These were experimentally validated throughout the following three sections of this chapter:

1. The camera settings, here under static conditions the resolution (full or half) and exposure time was investigated. It was observed that using half resolution halved the number of detected matches, increasing the exposure time was observed to increase the number of matches up until a certain point

where the near linear relationship was observed to level off. The mean error in matches vs. exposure time was observed to reach a minimal value at a lower exposure time sooner than for half resolution. Furthermore, the error did not reduce further once the total number of matches reached around 150 at 15 ms for full resolution and a similar number of matches at 20 ms for half resolution.

2. The determination of the ideal deployment speed, carried with a fixed exposure time of 10 ms (with just a focus on matching error i.e. no consideration given to laser ring spacing). The deployment speed was varied from 0.5 metres per minute to 10 metres per minute, the error was observed to remain acceptably low until around 3 metres per minute where it began to reduce after the next measurement of 5 metres per minute it was observed to break down and produce near maximum error. The percentage of matching features was also observed to reduce as the speed increased, this will be due to a combination of reduced image over lap and increasing image blur. The optimal results are therefore obtained at as slow a speed as possible but the system is observed to remain reliable until around 2-3 metres per minute.

3. The SIFT (see Chapter 2 Section 2.3.6 for an overview) parameters were investigated in turn varying from the standard value set of:

Contrast Threshold: 0.0075

Edge Threshold: 3.5

Number of Octaves: 3

Sigma: 1.5

The thresholding values performed as expected with the edge threshold increasing, leading to an increased number of matches, once the number of matches reached around 20 at a threshold value of 1.5 the error remained stable while the number of matching features rose to 300. A similar result was observed for the contrast threshold, although it is noted that this was seen to be dependent on the exposure time (higher exposure time moved the point at which the error would rise to a higher contrast threshold value) as expected and that the threshold is raised to minimise the number of matches while keeping the error minimal. Sigma was noted to reduce the number of matching features with an increase of value, further investigation of the effect of separation in the scale space and the impact on the Difference of Gaussian (DoG) would likely be required to fully benefit from making changes to this parameter, when compared to the value given by Lowe in [72]. Finally, the last point to note is that increasing the number of octaves had little effect on the error. A larger number of keypoints were detected but a smaller percentage of these were matched as the number of octaves increased, this suggests that much of the reliable feature descriptors are contained within the first octave.

Each of these three areas of optimisation are covered in greater detail in the following sections.

3.3.3 Camera Settings

The BFLY-PGE-50A2C camera [113] used in this work allows many different parameters to be set but the focus will remain on two key settings, all others will remain constant. Firstly, the resolution, it is possible to down sample the images, which decreases the storage required and processing cost per image. However, it comes at the clear expense of image quality. The second setting which can be adjusted is the exposure time, where a lower exposure time will decrease the motion blur but the images may become too dark for feature extraction/analysis of defects. The speed of the system is not only dictated by the motion blur but also the frame rate of the camera as this will determine the spacing between consecutive frames and thus the spacing of the captured laser rings. A study of these two parameters was undertaken with the camera moved 12.5 mm between frames, the purpose of this was to quantify the accuracy of the visual odometry in calculating the movement while adjusting these parameters. Such a study will mainly infer the amount of well matching image features, it will not provide insight into the amount of motion blur which would occur at those exposure times, this will be covered when considering the deployment speed.

For extracting and matching the features an OpenCV[117] implementation of SIFT was used.

The parameters used for extraction were fixed as follows:

Contrast Threshold: 0.0075

Edge Threshold: 3.5

Number of Octaves: 3

Sigma: 1.5

The first subject to cover is that as mentioned previously with increasing features and matches comes increased processing time as shown in Figure 3.16. In order to develop a real-time system, the time to process an LED image must be less than the inter frame time provided by the camera as not to build up a delay. A real-time system developed by the author which accomplishes this is shown in Chapter 5. The numeric values given for this study should be taken in a relative sense. For reference the calculations were performed on a Dell XPS 9550 laptop with an Intel Core i7-6700HQ (Quad Core 3.1 GHz).

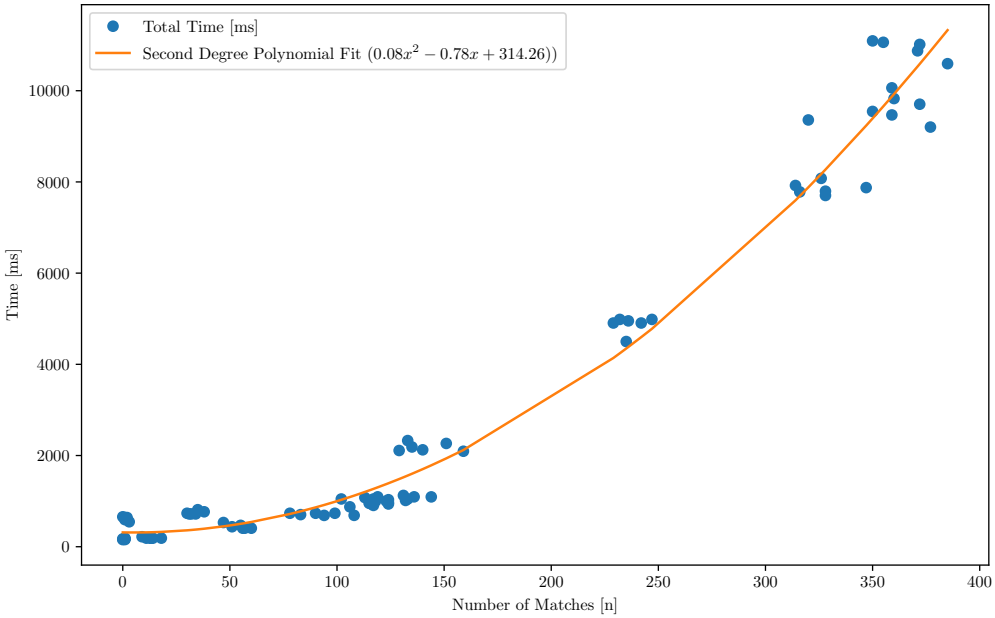

Figure 3.16: *Time taken to process matches vs number of matches*

For all variations of the parameters, the impact of halving the resolution was that it generally lowers the number of matched features and is observed to have an upper matching feature limit of around half that of the full resolution images. This is detailed in a histogram plot for all variations of parameters grouped into full and half resolution as shown in Figure 3.17.

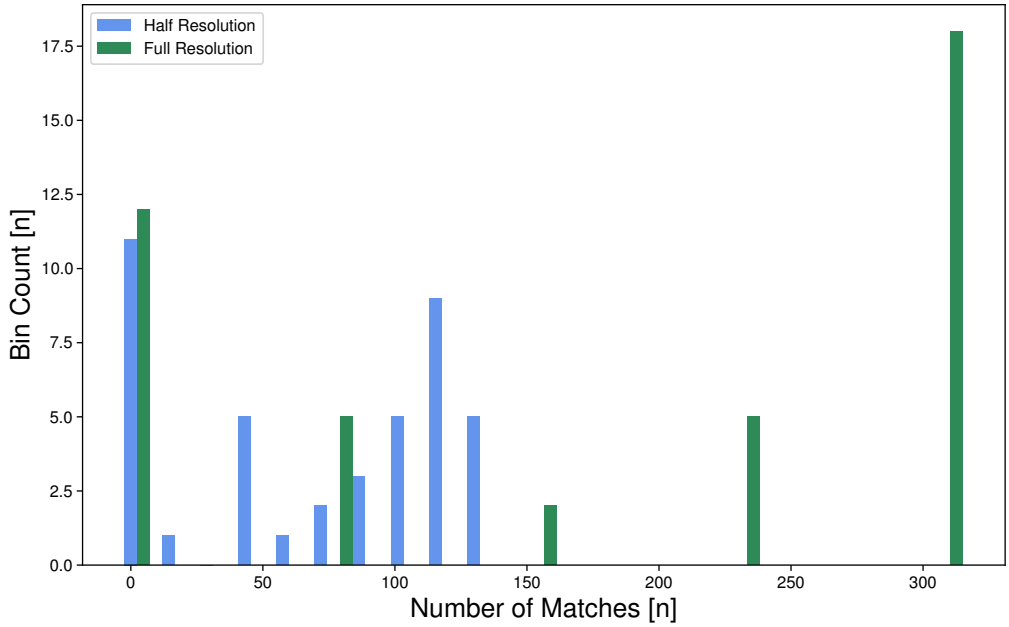

Figure 3.17: *Histograms showing the spread across various settings for full and half resolution*

To determine the exposure time at which there were enough valid matches extracted, a study was taken noting the total number of matches and the mean error between these matches and the ground truth. It is noted as that these experiments were performed in a static manner and motion blur was not yet considered. The total number of matches for various exposure times is shown in Figure 3.18a and the mean error in the matches based on the known ground truth between image pairs is shown in Figure 3.18b. It can be observed that at around 10 - 20 ms there the error significantly drops off and this is deemed a feasible starting exposure time. It is ideal to minimise this value to reduce the effects of motion blur which will be covered in the following section.

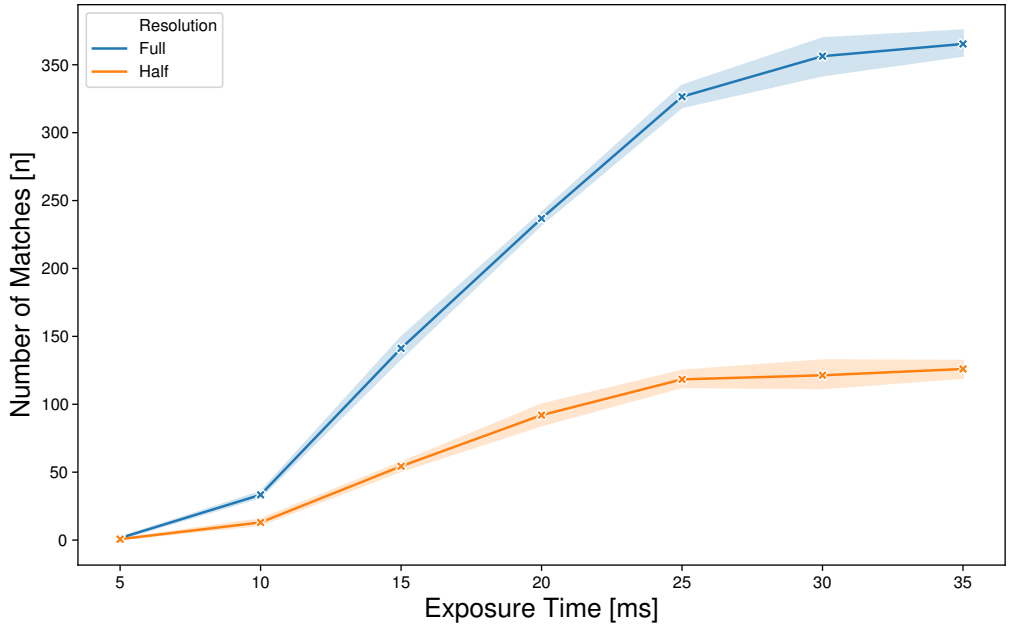

(a)

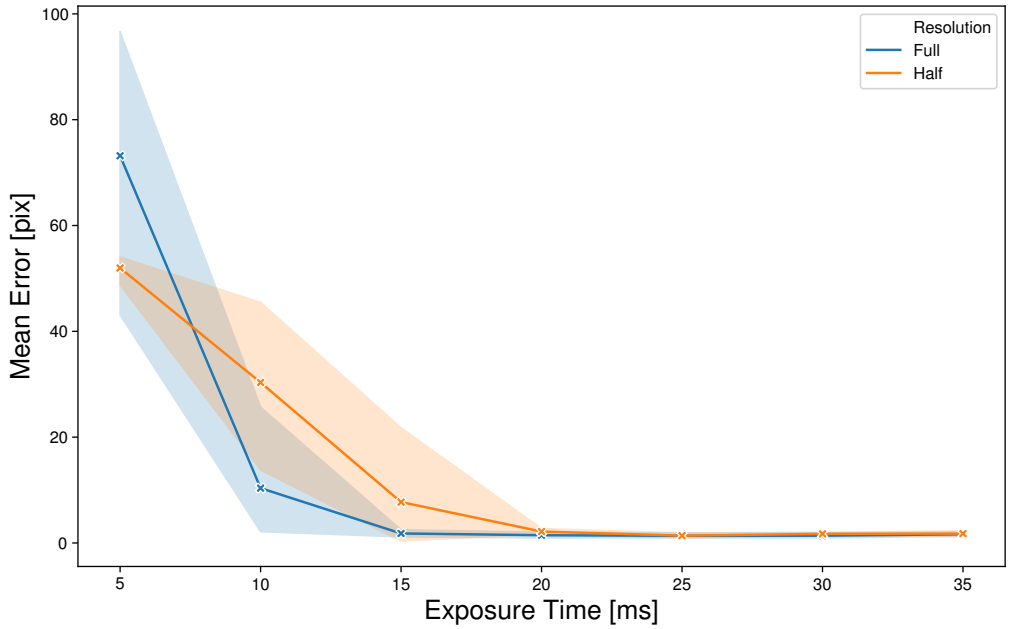

(b)

Figure 3.18: *(a) total number of matches between image pairs vs exposure time, (b) mean error in matches between image pairs vs exposure time*

3.3.4 Deployment Speeds

To obtain the range of deployment speeds that feature matching will successfully operate within, a section of pipe was repeatedly scanned using a robotic manipulator to precisely control the speed, this is shown in Figure 3.15.

The median change between frames is taken and subtracted from the previous change. This resulting difference should be 0 as the robot velocity is assumed to be fixed. The speed was varied between 0.5 metres per minute to 10 metres per minute, with a fixed exposure time of 10 ms and frame rate of 20 fps at full resolution. The mean number of matches and mean variation are shown in Figure 3.19a. It can be observed that as the speed increased the number of matches decreased and the variance of the difference between image pairs increases significantly. To further investigate the impact of the velocity the number of keypoints extracted is plotted alongside the percentage of matched keypoints. This is to separate the fact that as the velocity increases the number of matches would decrease as each image pair would have less overlap. Shown in Figure 3.19b it is observed that at 1 metre per minute the number of matches increases against the trend but the percentage of these points which are matched is reduced as expected. Variance in the number of keypoints and percentage matched is observed to increase slightly at higher speeds, this can however be attributed to a smaller dataset, at 0.5 metres per minute the section of pipe scanned consisted of 235 image pairs and at 10 metres per minute the same section was covered by just 10 image pairs. It is also noted that the spacing between images will have also increased, as features move towards the outer edges of the image they may no longer undergo a non-affine

transformation which SIFT is not invariant too. However, although the mean error was observed to increase drastically and break down beyond 5 ms it is not a conclusive result as there are no intermediate points between the measurement taken at 5 ms and 10 ms.

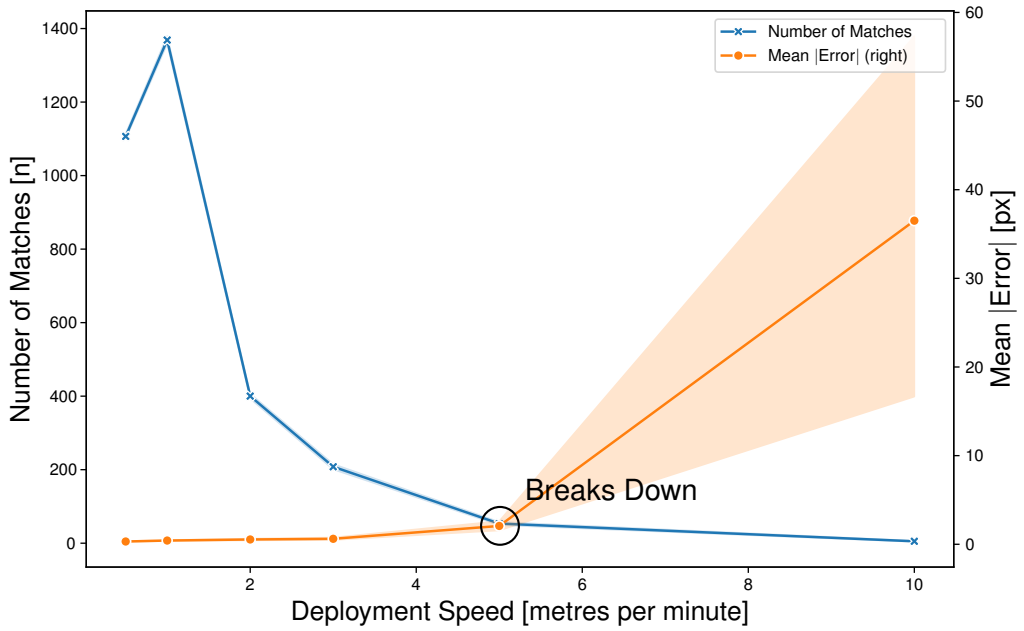

(a)

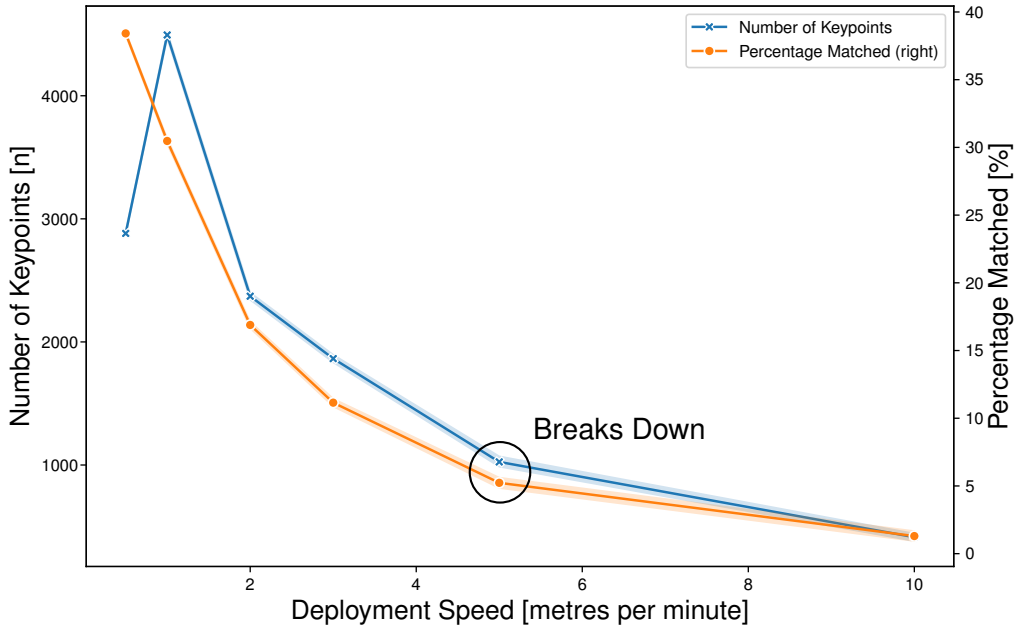

(b)

Figure 3.19: *(a) mean inter frame difference in matches between image pairs vs deployment speed, (b) number of extracted keypoints and percentage of those keypoints which were successfully matched vs deployment speed*

3.3.5 Feature Extraction

A study was conducted on varying the SIFT[72] feature parameters, only one variable was varied at a time. However, care was taken not to apply high thresholds which would limit the number of features prior to studying each independently. This iterative approach proved effective but it may be worth considering an expansion of the study to simultaneous variation of multiple parameters.

As with the previous study on the camera parameters the "standard" values were kept at:

Contrast Threshold: 0.0075

Edge Threshold: 3.5

Number of Octaves: 3

Sigma: 1.5

The exposure time was tested at both 15 & 20 ms to divulge the impact of the image intensity on the choice of the threshold values.

Each of the parameters listed prior were then adjusted to determine the change in number of matches and the quality of the match provided.

The camera was moved a fixed distance between frames a number of times. Between these image pairs, the median change in pixels of the matching features in the Y-Axis was calculated. The difference between this and the known pixel change is given as a mean error. The known pixel changes were determ-

ined by the set of pixel changes which resulted in no perceivable misalignment between stitched image frames. These initial reference values were obtained from the experiment carried out with the standard parameter set detailed prior.

The effect of the contrast threshold is shown in Figure 3.20. It is observed with a exposure time of 20 ms that up until a threshold value of 0.018 is reached the increase in the threshold value has minimal effect on the error but reduces the number of matches and therefore the computation time as observed in Figure 3.16. This value is further reduced to around 0.014 for the image pairs taken with a 15 ms exposure time. After these values are reached, the variation and error both sharply rise. The contrast threshold was the only parameter that had significant dependence on the exposure time, the remainder of the parameters will be shown for 20 ms only to aid the legibility of the plots.

Figure 3.21 shows a similar relationship but in inverse, the error reduces and the matches increase as the edge threshold is raised. Sigma as shown in Figure 3.22 removes a number of matching features while keeping the error relatively low for low sigma values at a value of around four the variation greatly increases and past this point as does the overall error. The final parameter to be adjusted was the number of octaves as shown in Figure 3.23a, again it is observed for the use of a single octave the variation in error is marginally larger. From two octaves onwards, there is insignificant change at the cost of increased memory usage for each octave and computation time for the number of matches. These results have shown that the contrast and edge threshold had the most significant result in terms of reducing the number of matches which was to be expected as they are as suggested by their names parameters which perform thresholding duties.

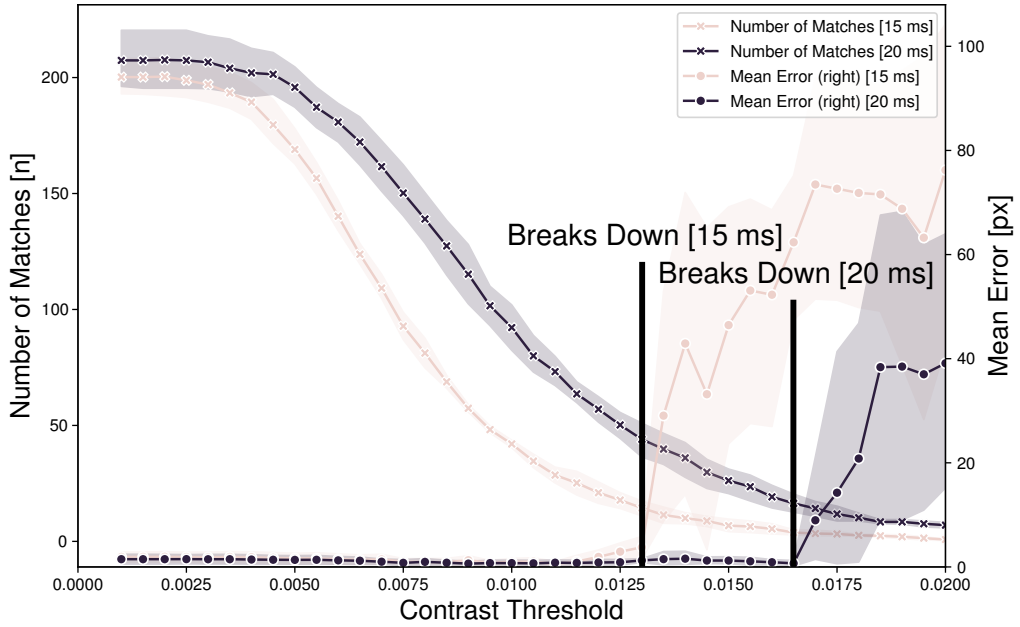

Figure 3.20: *Mean error and number of matches between image pairs vs contrast threshold*

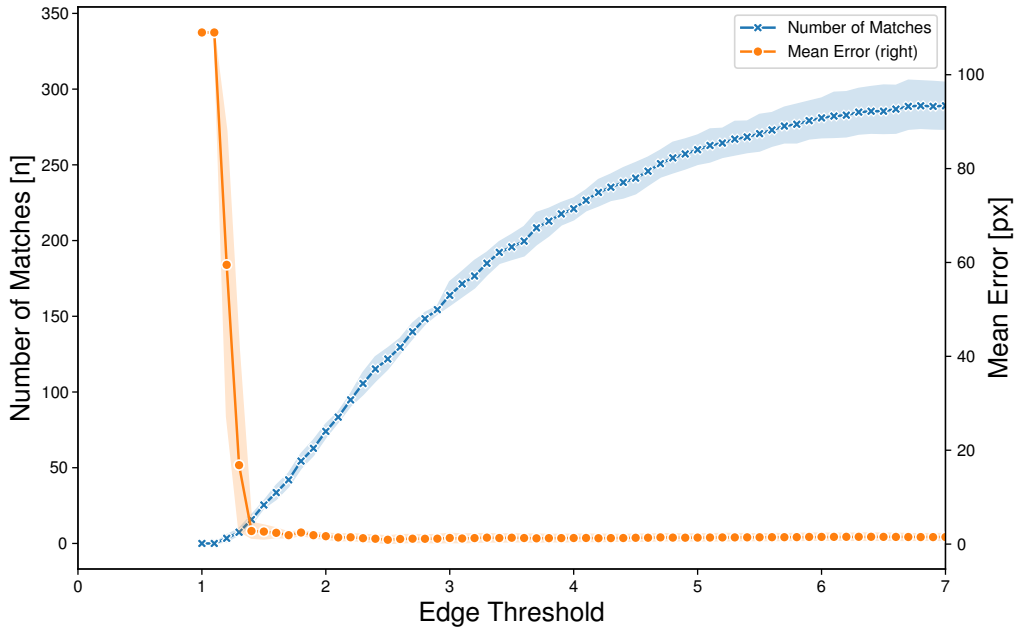

Figure 3.21: *Mean error and number of matches between image pairs vs edge threshold*

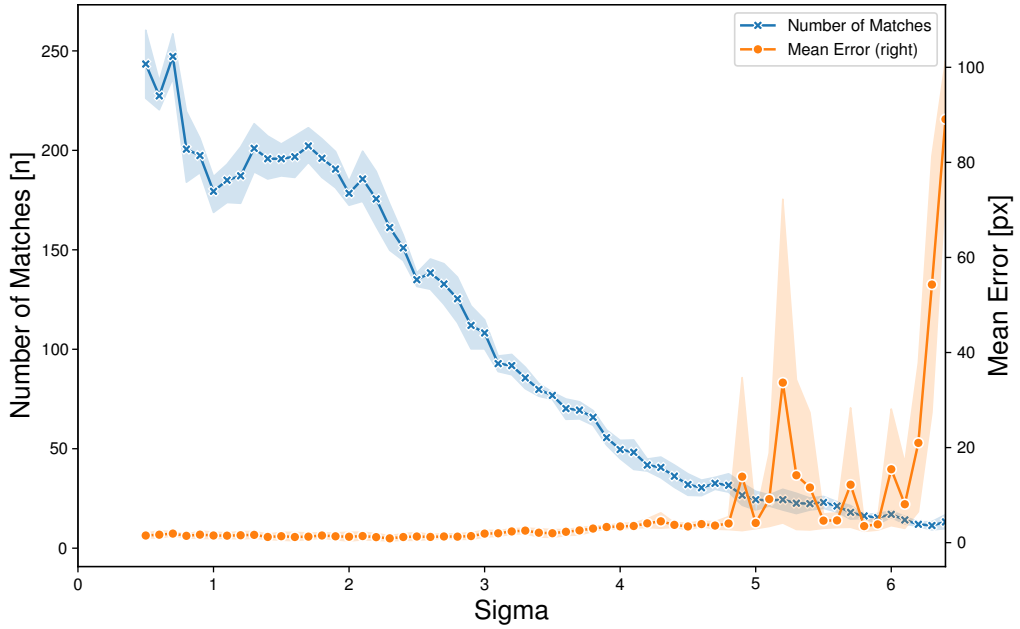

Figure 3.22: *Mean error and number of matches between image pairs vs sigma value*

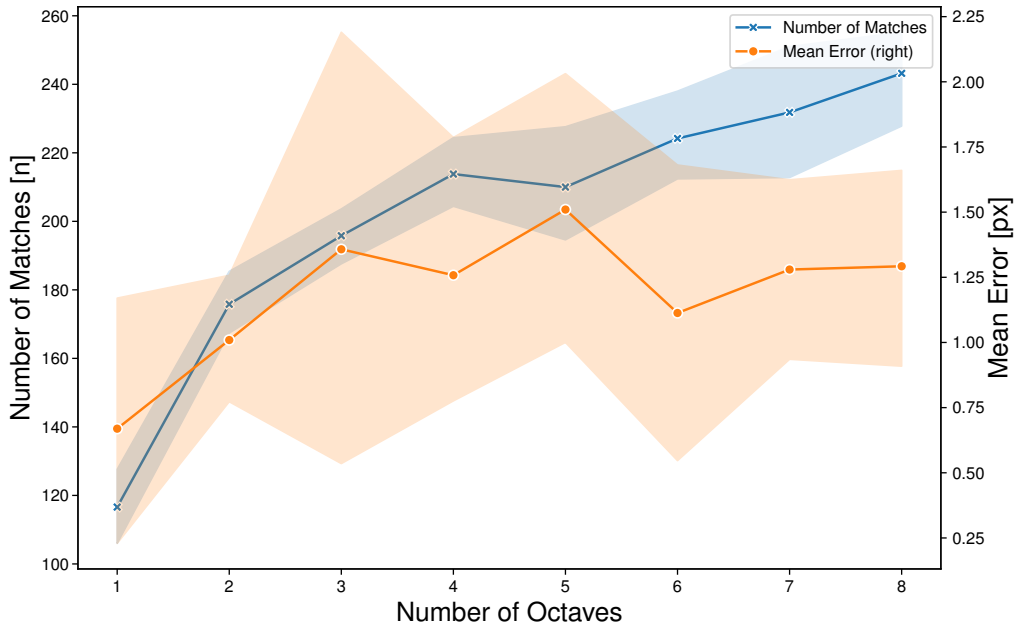

(a)

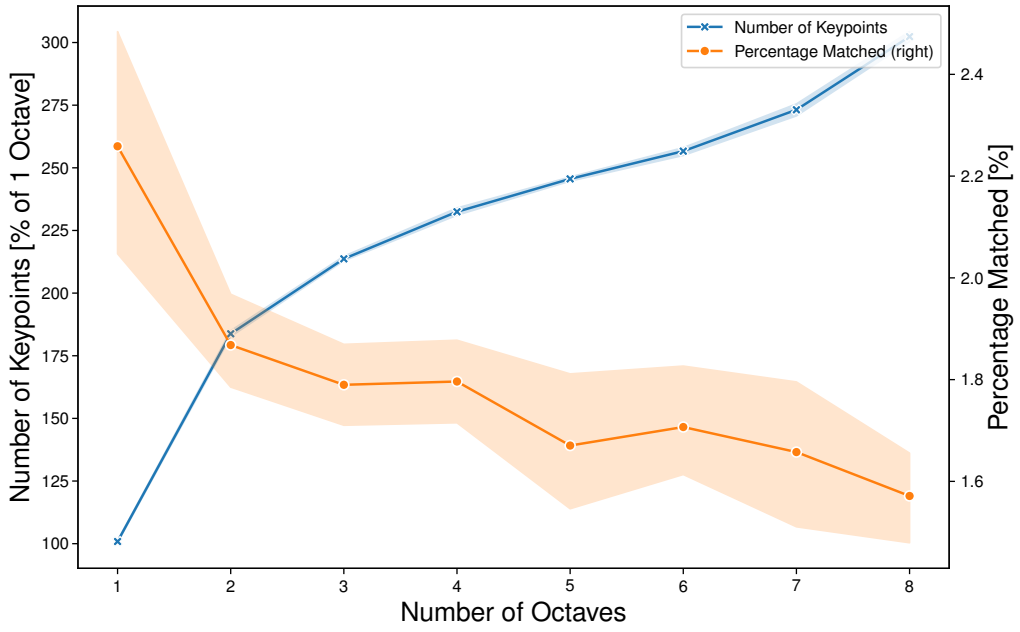

(b)

Figure 3.23: *(a) mean error and number of matches between image pairs vs number of octaves, (b) keypoints per frame and percentage matched vs number of octaves*

3.3.6 Parameter Optimisation Summary

A summary of the parameters and outcomes are given in Table 3.2. This is given as a guide to the reader, where we have focussed on optimising for efficiency while utilising the thresholding parameters to remove potentially weak features. Other use cases may not require this such as offline-processing. Furthermore, it may be valid to simply discard features if in a feature rich environment with high quality matches in abundance.

As a rule of thumb for the SIFT parameters, the numbers used were relatively conservative in reducing the number of features, placing the value just after the turning point of each curve before matches sharply reduce for each graph shown throughout this section.

Contrast Threshold: 0.0075
Edge Threshold: 3.5
Number of Octaves: 2
Sigma: 1.5

With the most significant change to the norms given by Lowe [72] being the removal of an Octave, this was shown as a valid decision experimentally in Figure 3.23b that the percentage of matches reduced per octave.

For the deployment speed the recommendation would be to maintain 1 metre per minute for two reasons, this lower speed adds more tolerance to variation in the speed during manual deployment. Also considering the laser spacing at 20 frames

per second, with each other frame being a laser image, the spacing between them would be 1.7 mm, in scenarios where accuracy is paramount it may be necessary to move at a rate determined by the minimum defect size sizing required.

Therefore, if starting with deployment speed as the first parameter, the exposure time could be adjusted until the images are of an acceptable brightness while keeping the value sufficiently low as to not induce motion blur. At this point it may be necessary to introduce gain into the system to reach the required brightness for visual inspection (i.e. the surface quality can sufficiently be inspected), this comes at the cost of introducing noise into the image. At this point the SIFT parameters can be adjusted in a similar manner as shown in Section 3.3.5. In terms of resolution, the author found operating with full resolution to be optimal, especially in practical cases where the number of reliably matching features fell towards the threshold for operation. However, it may be an option to consider for other applications with perhaps surfaces finishes which produce more robustly matching features, the live operation could utilise downscaled images while recording the full resolution images for post processing. There could also be a hybrid regime where downscaled images are used to calculate the movement of the probe and the full resolution images for stitching in display, this could be explored further in future work.

Lastly, as noted in the deployment speed testing the exposure time was reduced to around 10 ms with a multiplication factor of around 1.5 dependent on the pipe diameter and surface finish applied to the image in post processing to compensate for the reduction in image brightness. This reduction in exposure time was ne-

cessary for the feature matching to remain within acceptable error bounds while also increasing the systems robustness in response to the variations due to manual deployment as mentioned previously.

		Increase	
		Pro	**Con**
Camera			
Exposure Time	Optimised	Increased light, more information in the images	Increased risk of motion blur & saturation
Gain	Fixed	NA	NA
White Balance	Fixed	NA	NA
Gamma	Fixed	NA	NA
Resolution (scaling)	Optimised	Larger number of features & resolution for image stitching	Increased processing time
Deployment			
Speed	Optimised	Quicker inspections	Greater risk of motion blur & separation between laser ring extractions
SIFT Extraction			
Contrast Threshold	Optimised	Reduced number of matching features	Increased processing time, minimal filtering of features which may be of low quality adding to the processing time with no benefit
Edge Threshold	Optimised	Minimal filtering of features which may be of low quality adding to the processing time with no benefit	Reduced number of matching features
Number of Octaves	Optimised	Increased number of features	Increased memory and processing (scale space not a big factor in this data)
Sigma	Optimised	Increasing sigma will increase scale space separation this optimisation value provided the most successful matching criteria	
Scales	Fixed		

Table 3.2: *Parameters optimised for optimisation and expected pros and cons of increasing the value*

3.4 Summary

This chapter presented the laser pipe profiler used by the author and their associates. Firstly, an overview of the system was presented detailing the components which form together to create the probe: the laser projector & fisheye camera. A description of the operation and benefits that this method provides was given, i.e. the combination of laser profiling and image stitching to create a detailed description of the pipe under inspection which can easily be interrogated for defects. The laser profiling was described and will be presented fully in the following Chapter 4.

Following on from the overview of the system, a simulation environment was presented which enables detailed study of various probe parameters. A study of the impact a two-pixel error has on the re-projection of the laser was shown with a varying distance of the laser projector and camera sensor (baseline) for varying pipe radii (reflector distance). It was observed that as the distance to the reflector increased the error in measurement rose exponentially. The rate of this increase was reduced with an increased baseline. This increase in baseline was not without cost to the system due to two main drawbacks: the initial error was larger although still less than 0.5 mm for a 100 mm baseline and the increased length would reduce the deployment capability of the probe through pipes with bends at certain sizes and radii. Another approach was presented where instead of a fisheye camera, a standard pin hole camera model was used which kept the error constant as the distance to the reflector increased. This may not be the case in reality as the observed points were mapped precisely onto the sensor plane as

opposed to being imaged by a sensor. A drawback which was noted when using a pinhole camera was the reduced field of view. At 18 mm (current baseline used on the probe), the maximum radius of pipe where the full laser ring would be observable was around 20 mm, similarly at a baseline of 100 mm this increased to around 115 mm. To overcome this limitation a multi pinhole camera arrangement was presented to provide more coverage of the pipe under inspection, the accuracy achieved with this arrangement was much greater than that of the fisheye based system but the complexity and size would also increase greatly. This design could however prove to be very effective in pipes much larger than that studied within this body of work for future applications.

Finally, the camera parameters and SIFT feature parameters were studied. Through a series of lab-based experiments, the optimal camera settings and deployment speeds were investigated. These were judged by the number of keypoints detected in the images and the percentage of those which were successfully matched. To infer the optimal SIFT parameters a fixed data set was used which was captured at the optimal deployment speed and camera settings. For each pair of images, the correct pixel difference in the Y-Axis was known, this along with the number of matches per image was used to determine each of the parameters optimal value. The parameter values deemed to be optimal were that which minimised the number of matches to filter those with lower quality and thus improve computational efficiency while also minimising the mean pixel change error when compared to the ground truth. These parameters are those which will be used in the industrial deployment as detailed in Chapter 5.

Chapter 4

Novel Calibration Methods for a Laser Pipe Profiling Tool

4.1 Introduction

To ensure the dimensioning capabilities of the profiler presented in Chapter 3 are robust and accurate, a calibration procedure was created to ensure the correct alignment between the conical mirror and camera centre. This new calibration procedure allows for adjustments to be made to the mirror in a quantitative manner as well as providing a method for correcting for known misalignment which can be measured during the calibration procedure. The benefit of this is that the technique is suitable for production probes without finite adjustment available to the conical mirror. In lab-based trials, the calibration technique reduced peak sizing errors from 2.7 mm to 0.14 mm in 120 mm diameter pipes.

4.2 Comparison to Methods in the Literature

When reviewing methods of calibration for monocular laser profilers in the available literature, the majority assume alignment and no calibration procedure therefore is defined. There are however some examples such as, Zhu et al. [118] which details a calibration technique for a similar system to that used by the author. It is however not suitable due to requiring the laser ring to be projected in front of the camera onto a target as opposed to that used throughout this thesis, which is orthogonal to the camera. Another method is shown by He et al. [106], a benefit of this calibration method is that it corrects for distortion caused by the supporting glass tube linking the camera to the laser projector. A downside to this is that it requires an additional camera for the process.

A method of calibration which could be implemented is that demonstrated by Buschinelli et al. [102]. In the procedure presented, the profiler is mounted upon stages inside a highly accurate calibration artefact. The artefact consists of a series of known step sizes in a cone like geometry, a polynomial is calculated for each angle of the imaged laser ring from images taken at each step of the calibration artefact and interpolated for the full sizing range of camera. This provides a function for each pixel in the image mapping to a certain radius.

This chapter introduces a new technique for alignment of the camera and laser module allowing for correction of angular misalignment as well as translation with manual adjustment of the laser profiler. The procedure allows for correction of angular error without manual adjustment, making it suitable for production ready systems.

An advantage of the proposed technique when compared to [102] is that the calibration is performed with a single capture vs approximately 30 images with the use of an arguably simpler set-up and calibration object than that used by Buschinelli et al which is shown in Figure 4.1a. When compared to [106] there is no need for an additional camera and the complexities this adds to the calibration, the experimental set up used in [106] is shown in Figure 4.1b. Furthermore, the calibration method presented by He et al. required 29 images to be taken of a chequerboard in various positions increasing the time and effort required whereas the calibration method which will be presented in this chapter only requires a single image with no additional camera. He et al. report an error of 0.23 mm when measuring a 288 mm pipe, Buschinelli et al. report an error of 0.2 mm on 100 mm diameter pipe sections. These values can be compared to the error of the authors system of 0.14 mm in a 120 mm diameter pipe.

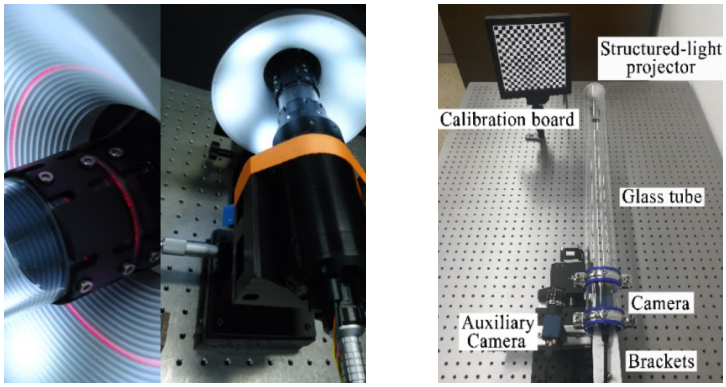

(a) (b)

Figure 4.1: *Alternative calibration set-ups: (a) shows that used by Buschinelli et al. [102] and (b) shows that of He et al. [106]*

4.3 Alignment Error

For reference the current hardware prototype is shown in Figure 4.2. A model detailing the geometry of the laser profiler is shown in Figure 4.3.

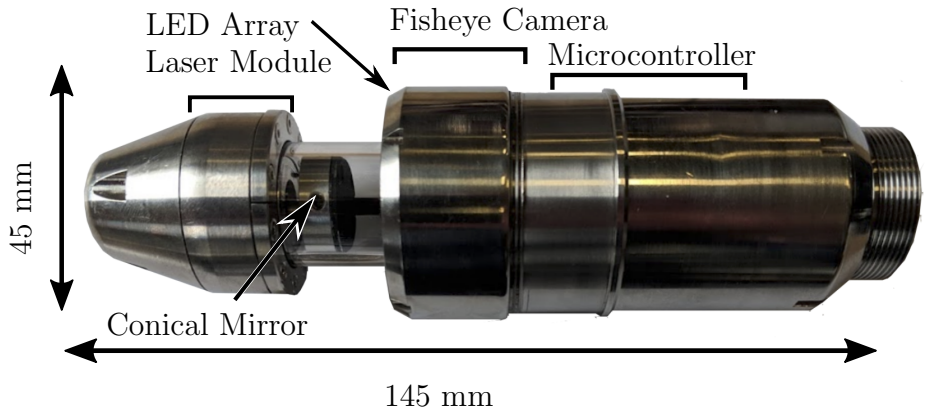

Figure 4.2: *Camera and laser profiler with subsystems highlighted (repeated from page 104)*

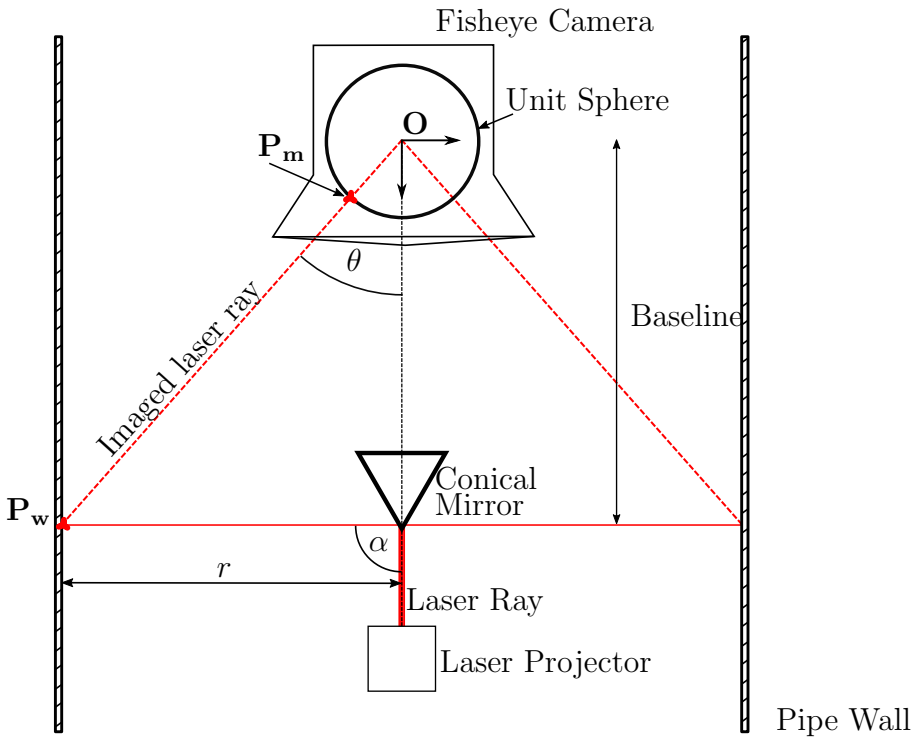

Figure 4.3: *Camera and laser profiler geometry*

The accuracy of the re-projected laser point is determined by a number of different sources which are summarised as follows:

1. Systematic Error
   (a) Misalignment — manufacturing tolerances, optical axis and laser misalignment
   (b) Opening angle (α)
   (c) Baseline length
   (d) Intrinsic camera properties

2. Sampling Error

    (a) Variable laser line width

    (b) Photo-sensor noise

The systematic errors listed occur due to differences between the model given in Figure 4.3 and the manufactured probe. These differences have a direct impact on the accuracy of the measured diametric information of the sample under inspection. It was previously assumed in the model that the laser plane is parallel to the image plane i.e. constant α of 90° revolved around the model. Due to manufacturing tolerances, angular misalignment may be introduced into the system removing this parallel constraint in the model thus resulting in sizing errors.

To illustrate this a diagram detailing how these errors arise due to misalignment is shown in Figure 4.4. In this case the probe is assumed to be centred within the pipe and the only source of error is due to angular misalignment of the conical mirror.

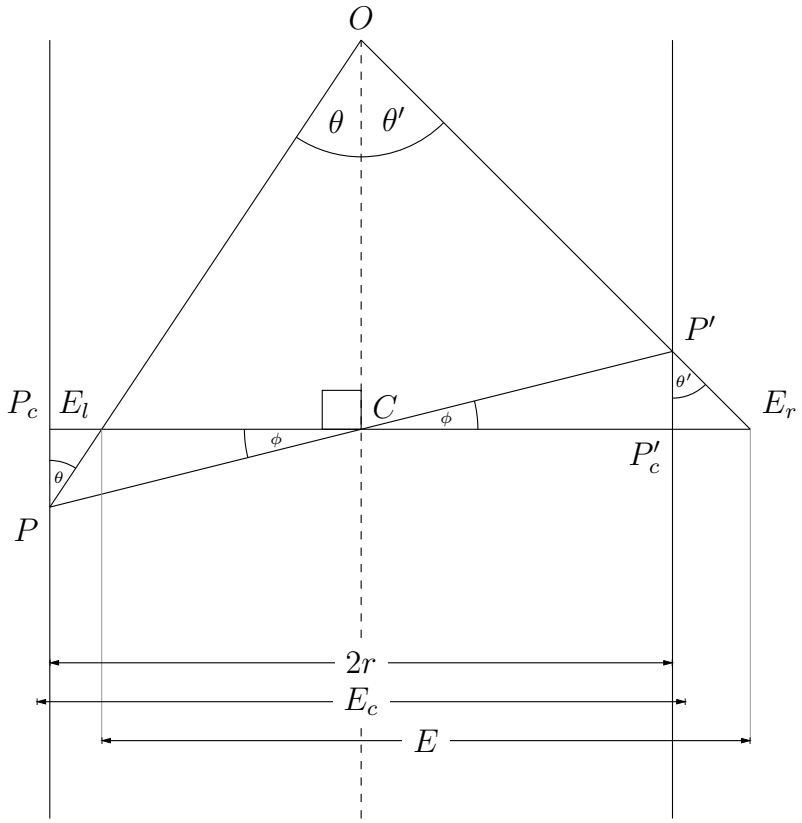

Figure 4.4: *Illustration detailing error in sizing of pipe radius (r) due to misalignment angle ϕ*

The diagram shows the expected laser line given as the vertex between P_c and P'_c and the actual laser line (P - P') resulting from the angular error (ϕ) of the conical mirror. The assumed opening angle is 90°, shown in the diagram as $\angle OCP_c$. The angles θ and θ' are the angles from the respective imaged points P and P' to the camera centre. In the case where the opening angle is assumed to be 90°, the re-projected points will be calculated as the point of intersection between a pair of rays drawn from O at angles θ and θ' and their intersect points on the line $Pc - P'_c$. These points of intersection are labelled as E_l and E_r and represent

the mis-measured points due to an angular misalignment of ϕ. The resulting diameter from this mis-measurement is shown as the dimension E, it is noted that there is a considerable translation error introduced as well as a sizing error shown more clearly by the dimension E_c which represents E with a translation to be in line with the central axis (shown as the dashed line).

4.4 Alignment Procedure

As described previously, alignment of the laser and camera are of critical importance for accurate laser measurements. When the laser and image plane are misaligned, the radial distance observed by the camera is not its true value. An overview of the alignment procedure to ensure alignment is detailed below:

1. Align camera to calibration block
2. Align laser ring within calibration block
3. Align laser centre within calibration block

To align the laser profiler and camera they are both referenced to the same calibration object shown in Figure 4.5.

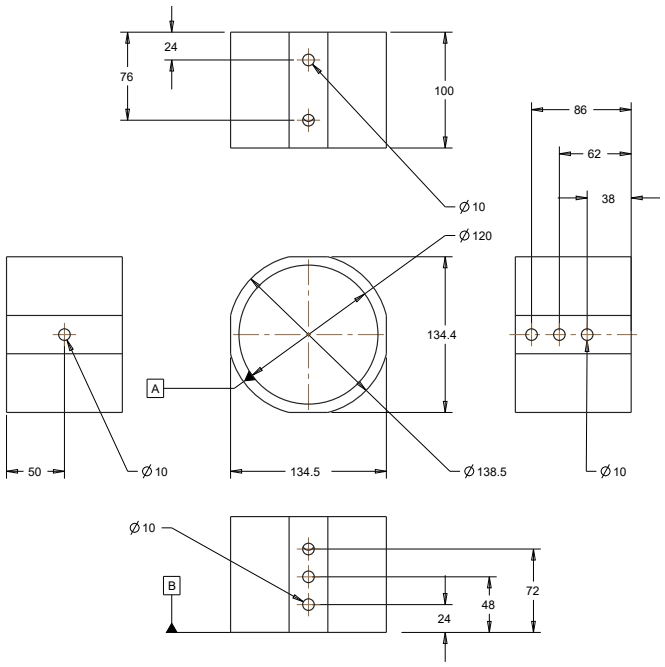

Figure 4.5: *Technical drawing of calibration block used for alignment of camera and laser profiler*

The calibration object consists of an accurately machined block of aluminium with nine flat-bottomed holes each with a point marker in the centre. These centre targets were extracted and used to align the camera relative to the block. Features within the block were recessed to allow accurate scanning of their relative centre points with a Faro Arm portable co-ordinate measurement machine. A ball-end probe was traced around each of the inside diameters of the flat-bottomed holes gathering a set of points representing the location of the features in 3D. A circle was then fitted to these points, the centre point of these circles would then serve as the ground truth for the 3D position of each feature point in space. To allow accurate positioning of the camera relative to the block a series of three stages (two translation and one tip-tilt) were used to give the camera the four degrees

of freedom required for alignment within the calibration block. Roll around the camera axis and travel along this axis are not required. A further tip-tilt stage is integrated with the laser projector of the probe to allow adjustment of the laser.

This tip-tilt stage is mounted on a slotted fixture to allow horizontal translation and shims were used to allow for vertical displacement, providing the same degrees of freedom as the camera unit allowing the laser projector to be aligned with the calibration block. The probe and stages are detailed in Figure 4.6.

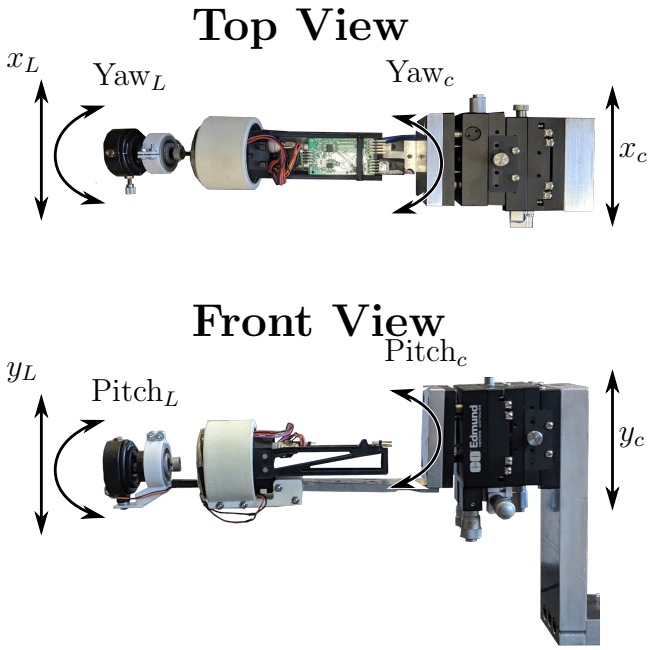

Figure 4.6: *Fisheye camera and laser profiler mounted to adjustment stages for alignment within calibration block with each stage's degree of freedom labelled*

The method used to position the camera in 3D space within the calibration block is the Perspective N-Points (PnP) algorithm, specifically developed by Urban et al. [119]. As the points of the test block are captured arbitrarily in space they

need to be transformed into a relative co-ordinate frame. This co-ordinate frame is based on the centre and axis vector of a fitted cylinder through the gathered points. To calculate the parameters of the cylinder, one must be fitted to the nine points this is achieved through use of the PROTO toolbox [120]. The main parameter of interest is the axis of the cylinder which fits these points as it will be used as the Z-Axis in the new co-ordinate system. This along with a chosen point on the cylinder (in this case the point which is the lone feature on one side of the test block detailed in Figure 4.5) is the basis of a co-ordinate system which will be used for positioning the camera. The origin is to be described as the point of intersection between a perpendicular line from the selected point and the axis of the cylinder. The vector describing this line is to be the X-Axis and is described by the following Equation (4.1):

$$\vec{x} = (\vec{PA}) - ((\vec{PA})\vec{C})\vec{C} \tag{4.1}$$

Where $\vec{PA}$ is the vector between point P_{xyz} as the selected point on the pipe, A_{xyz} is the origin of the fitted cylinder and $\vec{C}$ is the vector describing the cylinder axis. The point of intersection and thereby the origin of the system is given by Equation (4.2).

$$O_{xyz} = \vec{x} + P_{xyz} \tag{4.2}$$

The Y-Axis is the cross product of the Z and X-Axis vectors. A co-ordinate system has now been described by the cylinder, however it would be more desirable for the origin to be at $0, 0, 0$ and the Z-Axis to be equal to $[0, 0, 1]$. To achieve

this a basis transformation is performed, a homogeneous translation matrix based upon the axis of the system as shown in Equation (4.3) is created. This is then applied to the captured points denoted as D in Equation (4.4).

$$T = \begin{bmatrix} x_0 & y_0 & z_0 & O_0 \\ x_1 & y_1 & z_1 & O_1 \\ x_2 & y_2 & z_2 & O_2 \\ 0 & 0 & 0 & 1 \end{bmatrix} \tag{4.3}$$

$$\text{Points} = T^{-1} \begin{bmatrix} D_{00} & D_{10} & D_{20} & \dots & D_{n0} \\ D_{01} & D_{11} & D_{21} & \dots & D_{n1} \\ D_{02} & D_{12} & D_{22} & \dots & D_{n2} \\ 1 & 1 & 1 & \dots & 1 \end{bmatrix} \tag{4.4}$$

After this operation the points and fitted cylinder are observed as shown in Figure 4.7. These points and relative co-ordinate frame may now be used as a reference to position the probe co-linearly with the calibration block.

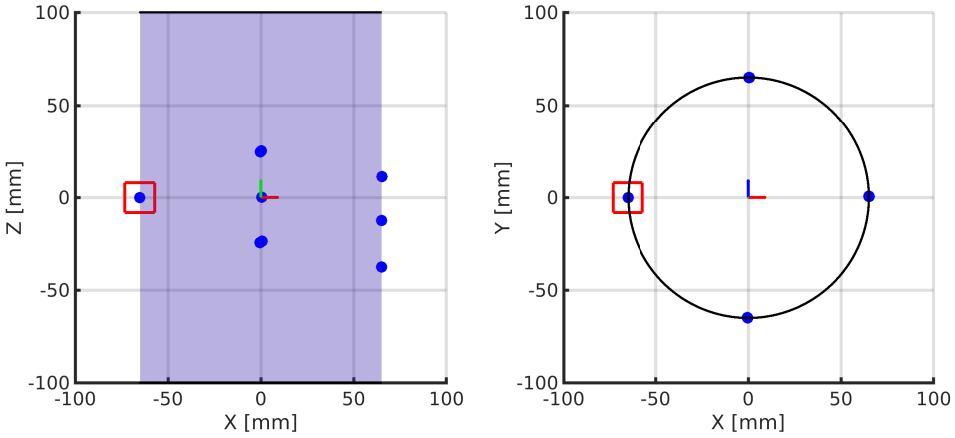

Figure 4.7: *Feature points with respect to the co-ordinate frame used for determining the relative position of the probe within the calibration block, the selected point for positioning the co-ordinate frame is highlighted*

To extract the centre point of the features for input into the PnP algorithm, targets were located centrally within each recession of calibration block. An example image taken within the calibration block is shown in Figure 4.8.

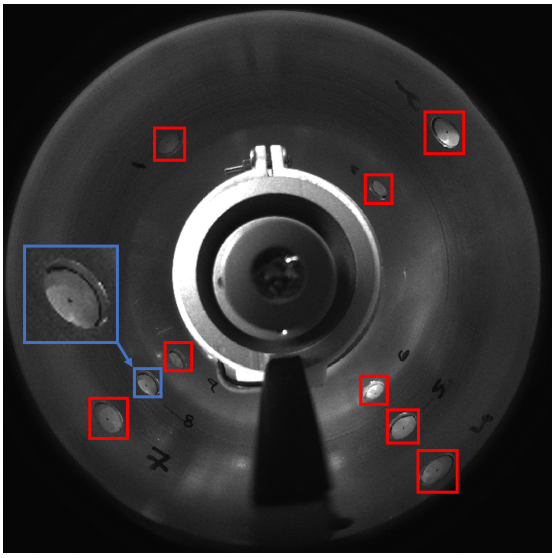

Figure 4.8: *Image taken by probe within calibration block, showing the nine features (highlighted) used to centre the probe within the block using the PnP algorithm*

For extracting the centre of these targets, a pattern was required, two main patterns were investigated, a central dot and a chequerboard which are widely used in literature for camera calibration. Three targets were trialled as shown in Figure 4.9a, two dot markers were tested as well as a single chequerboard target. To extract the centre point of each target the corner detector developed by Shi and Tomasi [121] was implemented. Responses of the corner detector for each pattern are shown in Figure 4.9b. A threshold was then applied to the image, the value of which was experimentally obtained as 70 % to effectively highlight the marker locations with the lighting and camera settings used during experimentation. The resulting binary output is shown in Figure 4.9c. To determine the centre of the target, the central region of connected pixels was then extracted and the centre of this region was deemed to be the centre of the target. It is noted with

a different processing technique the chequerboard example may have provided more compelling results. However, due to the simplicity of the method and with the accuracy criteria already met with the small dot target this was not pursued. An example of the extraction is shown with feature point as marked by a cross in Figure 4.10.

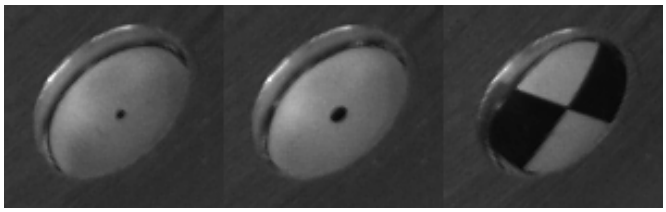

(a)

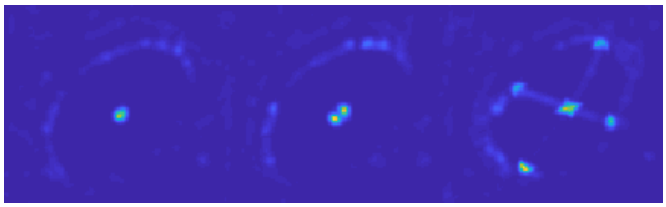

(b)

(c)

Figure 4.9: *Corner detector response for varying patterns, (a) shows the input image patterns (small dot, large dot and chequerboard), (b) shows the corner response for each and (c) shows the corner response with a threshold of* 70 % *applied*

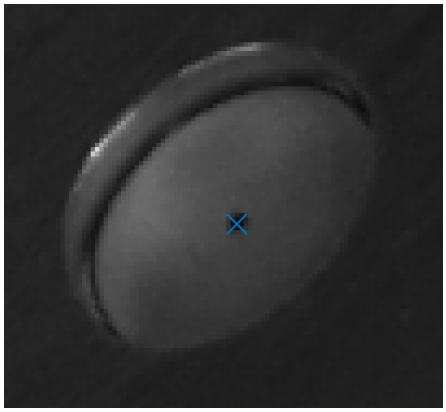

Figure 4.10: *Example extraction of the region of interest around a localising feature of the calibration block*

With the pixel/world point coordinate relations now known for each feature of the calibration block, the camera may be aligned. The process for this is shown in Figure 4.11, the camera is deemed to be aligned when the observed X & Y values were in oscillation around 0. In translation the camera was positioned within 0.1 mm with a standard deviation of 0.03 mm in X and Y over 100 repetitions of acquisition and processing.

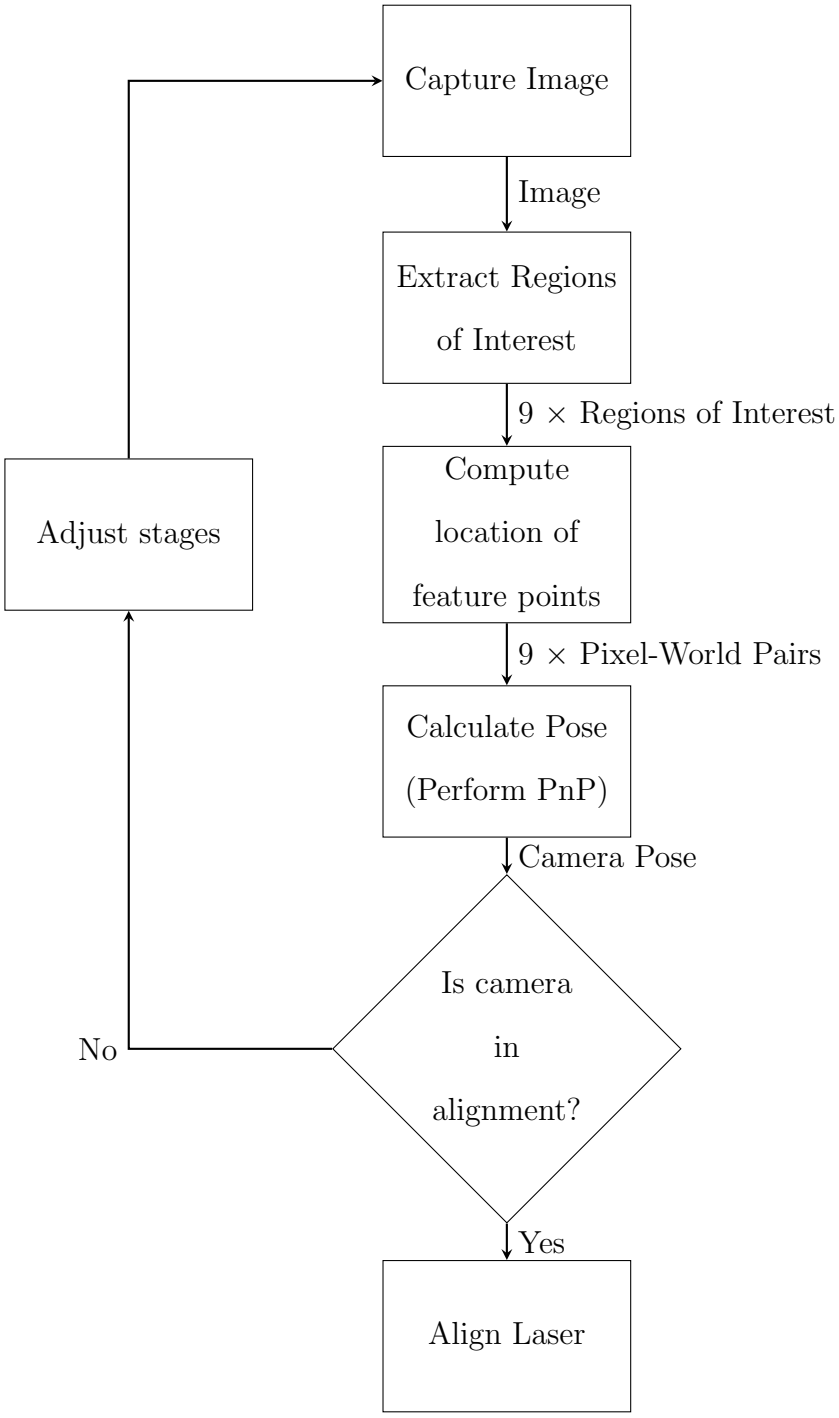

Figure 4.11: *Procedure for aligning camera within calibration pipe*

4.5 Laser Alignment

With the camera and pipe in alignment, the laser was aligned to the common calibration block. The first step in this process is extracting the projected laser ring from the image, this is achieved through the following steps (steps 2 & 3 are repeated for multiple lines of extraction):

1. Define a discrete circle whose diameter is equal to that of the image width.
2. Obtain the intensity values along a line from the image centre to each point on the circle.
3. Extract the peak intensity value along this line.
4. Fit a circle to the pixel locations of the collection of extracted points.

Lines of extraction between the two points are shown in Figure 4.12, the intensity along an example line is plotted in Figure 4.13 and an image showing the fitted circle in Figure 4.14.

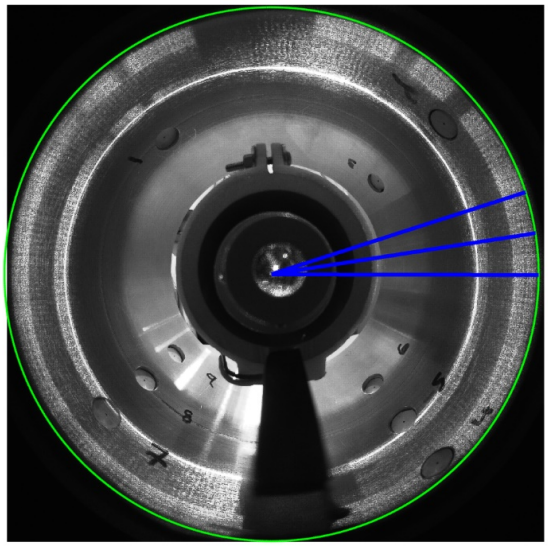

Figure 4.12: *Image detailing extraction of the projected laser ring, the green circle illustrates the extents of extraction, the blue lines show example extractions of intensity going around the full circumference*

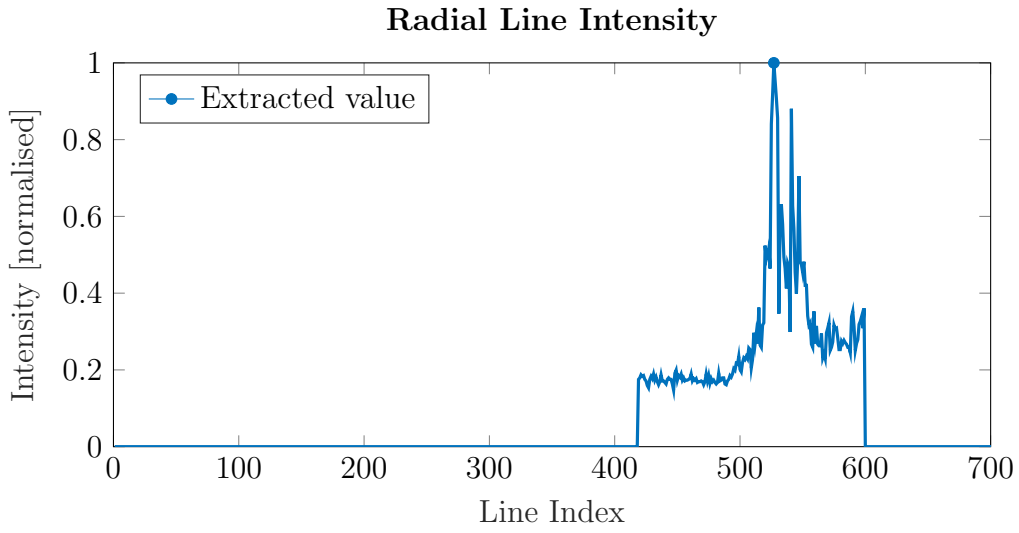

Figure 4.13: *Extracted intensity line (threshold on index applied), the circle at the peak intensity value marks the line index at which the laser ring is deemed to be located along the line of extraction*

The laser alignment is completed in two steps, the first is to align the laser plane. Alignment of the laser plane is achieved by adjusting the angular stages of the laser module as shown in Figure 4.6. For a measure of angular alignment to use during the process which was relatable to the adjustment of the stages, a circle was fitted to the extracted laser ring. The centre of this circle could be used as a reference for alignment with the error being the distance from the image centre. The yaw adjustment allowed adjustment in X and the pitch adjustment allowed for adjustment in Y. The stages were adjusted until the fitted circle had a centre equal to the camera centre. When this occurs the laser plane is orthogonal to the pipe axis and parallel to the camera plane. This can be further confirmed by calculating the bearing vector at each point of the circle and ensuring they are equal. In the example aligned image shown in Figure 4.14, the extracted circle shown in red has an error from camera centre of 0.44 pixels in X and -0.20 pixels in Y.

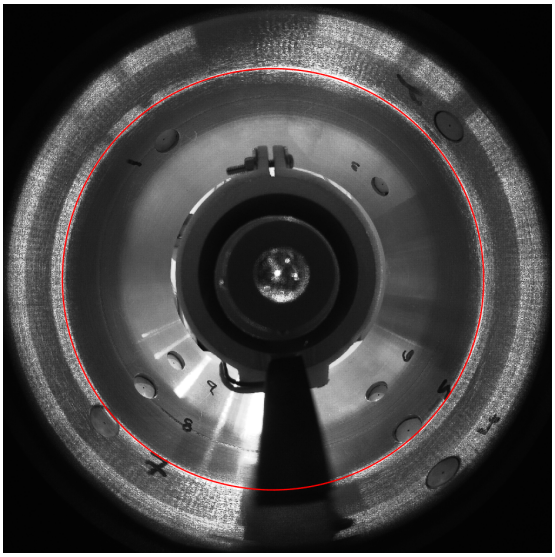

Figure 4.14: *Aligned laser, circle fit of laser shown in red*

This slight error can be seen in the aforementioned bearing vector calculation. Across 2000 points of the laser circle the mean angle was 69.9° with a maximum deviation of 0.09°. This can be compared to a deviation of four degrees in both axis of adjustment in the laser stage, the resulting circle centre was located at 19.1 in X and 24.3 in Y. The mean bearing vector value was 70.4°, the maximum deviation was noted as 4.34°. The bearing vector calculated at each extraction point around the laser ring is plotted in Figure 4.15 showing both the aligned data and the four-degree misalignment data for reference.

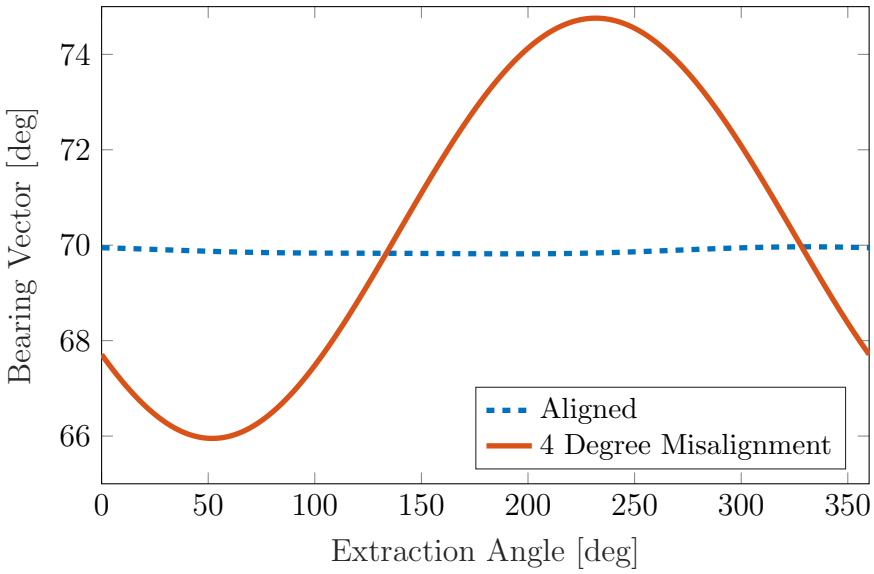

Figure 4.15: *Calculated bearing vector at each point in laser circle for aligned and misaligned conical mirror*

The laser plane can now be assumed to be aligned with an opening angle of 90° at all points around the image.

In this configuration, the laser's angular alignment is correct. However, there still exists an error in translation. As this body of work is focusing on the error due to angular misalignment this translation error must be corrected so as not to have an impact on the results. To position the laser correctly an external feature is used, this is due to the fact once aligned the source could be placed anywhere within the calibration block and produce the same image due to the planar nature of the projection. The outline of the housing of the conical mirror is visible from the camera's perspective, this gives an accurate reference to position the conical mirror in translation. As there is a large contrast difference between this area and the outer housing it can be extracted using a circular Hough transform [122] localised within the region. An example image showing the extracted circle highlighted in blue is shown in Figure 4.16. The centre of this extracted circle is compared to the camera centre as performed previously with the angular misalignment. Translation according to Figure 4.6 in Y was achieved using shims beneath the module and in X by the virtue of the module being mounted on a slotted plate. Centring of the extracted circle was repeatable to within a pixel of the camera centre. The variation in extraction due to lighting and other factors caused a deviation of ± 3 pixels over multiple images. Once this procedure is complete the laser is known to be aligned in both orientation and translation with reference to the camera central axis, which itself is aligned to the calibration block.

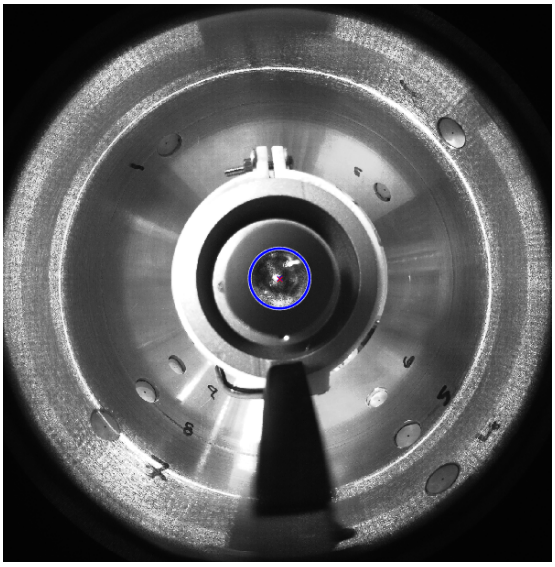

Figure 4.16: *Centring of conical mirror using circular Hough transform on the mirror outline*

4.6 Laser Misalignment

With the laser in alignment it is possible to study the angular error in a controlled manner utilising the angular stages housing the laser module. From the aligned position the stage was adjusted to a maximum of 5.5° in each axis in steps of 0.35°. At each position, a laser image was captured, a circle was then fitted to the data to remove any noise in the extraction. Each point of the circle was projected into 3D space with an assumption that the opening angle was 90°. Two error values are then calculated, the radius error i.e. the error of the projected circle vs the calibration block and the positional error given as the distance from the origin to the centre of the projected circle. The radius error is shown in Figure 4.17 with a max/min error of: 1.5 / 0.05 mm. The positional error in Figure 4.18 has a

max/min error of: 15.8 / 0.12 mm. These results reflect that the error has a much greater impact on the position as opposed to the radius as detailed in Figure 4.4. The errors of the system with respect to a known angular misalignment are now deemed to be well understood and it would be advantageous to correct for them without manual adjustment, a method for this will be introduced in the following section.

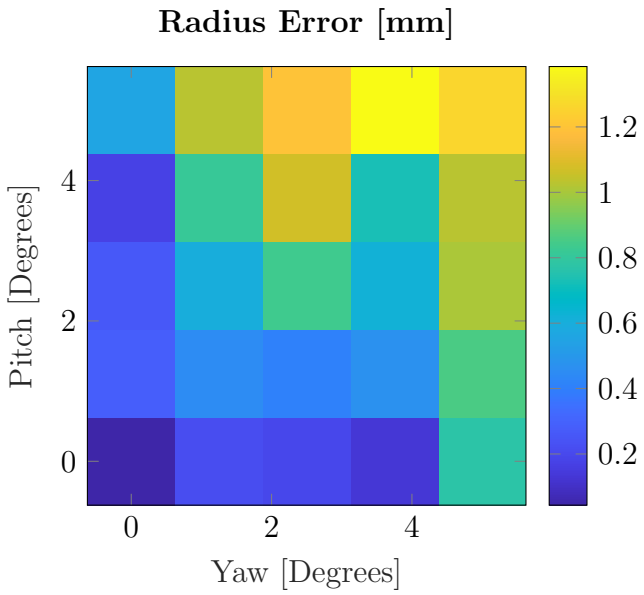

Figure 4.17: *Radius error across 0–5° of angular misalignment*

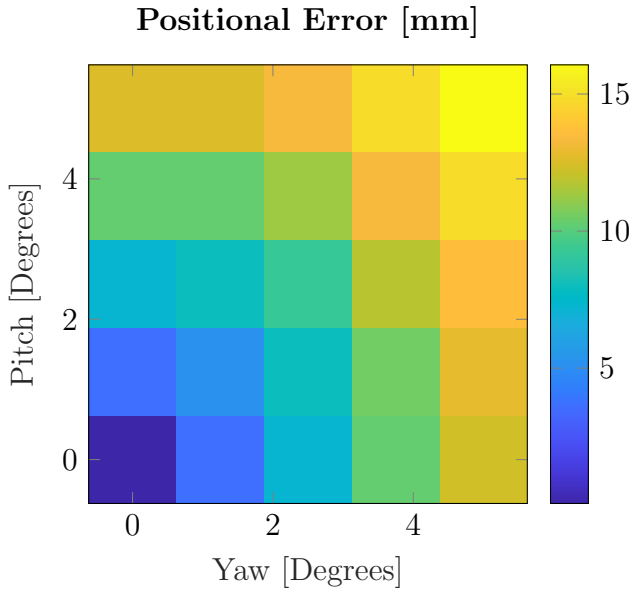

Figure 4.18: *Positional error across 0–5° of angular misalignment*

4.7 Laser Correction

Prior to the completion of this work the previous method used to calibrate the laser profiler was to estimate the opening angle and baseline using a series of known radii calibration samples. A minimising function was utilised to calculate the opening angle and baseline, these values were assumed to be equal around the entirety of the image leading to the errors shown previously where misalignment was present. With the profiler co-linear with the calibration block a more comprehensive calibration can be performed, correcting for angular misalignment at discreet points through the entire 360° of the profiler. When centred the origin to each point of extraction on the calibration block is at a known distance and the

conical mirror can be assumed to be machined highly accurately to a 45° angle. Using this information, a two-step calibration procedure can be performed. This is summarised in the following sequence:

1. Extract laser ring.
2. Calculate bearing vector for opposite points on ring and average (opening angle known to be 90 degrees).
3. Derive baseline from these values.
4. Calculate unique opening angles with baseline.

The first step in this correction process as with previous examples is to capture an image of the laser ring and fit a circle to the data. Following this the baseline can be calculated for two opposing points on the laser ring for example 0° & 180°. Between these two points the opening angle of the laser can be assumed to be a combined value of 180° due to the known geometry of the conical mirror. For the two extracted points the bearing vector ($\mathbf{P}_\mathrm{m}$) was acquired using the camera model, θ as denoted in Figure 4.3 can then be calculated (Equation (4.5)) where $\mathbf{C}$ denotes the camera axis $[0, 0, -1]$.

$$\theta = \arccos\left(\frac{\mathbf{P}_\mathrm{m} \cdot \mathbf{C}}{\|\mathbf{P}_\mathrm{m}\| \, \|\mathbf{C}\|}\right) \tag{4.5}$$

By calculating theta for both extraction points and taking the average a synthetic point is created with an effective opening angle of 90° this can then be used to calculate the baseline length (B) for these two points using the known radius of

the calibration block (R).

$$B = \frac{R}{\tan \theta_{\text{avg}}} \tag{4.6}$$

For all extraction points of the laser ring a baseline is now known and unique opening angles (α) can be calculated (in the following theta is calculated for each point independently).

$$\alpha = \pi - \theta - \arcsin\left(\frac{B \sin \theta}{R}\right) \tag{4.7}$$

There now exists n baseline (B) values and n α values for each angle of extraction around the laser image. Calculating a world point ($\mathbf{P_w}$) from a given mirror point ($\mathbf{P_m}$) and its associated θ value at extraction index i is given by Equation (4.8).

$$\mathbf{P}_{\text{w}} = \mathbf{P}_{\text{m}} \frac{B[i] \sin(\alpha[i])}{\sin(\pi - \theta - \alpha[i])} \tag{4.8}$$

The effect of this calibration method is illustrated in Figure 4.19 where the laser profiler was set to have a four degrees angular error, the left images denoted as Global Angle shows the large positional error as first shown in Figure 4.18 and the laser being projected parallel to the calibration block ends (marked as black rings in the figure). On the right side of the image labelled as Multi Angle the positional error has been corrected and the laser is projected at the true angle.

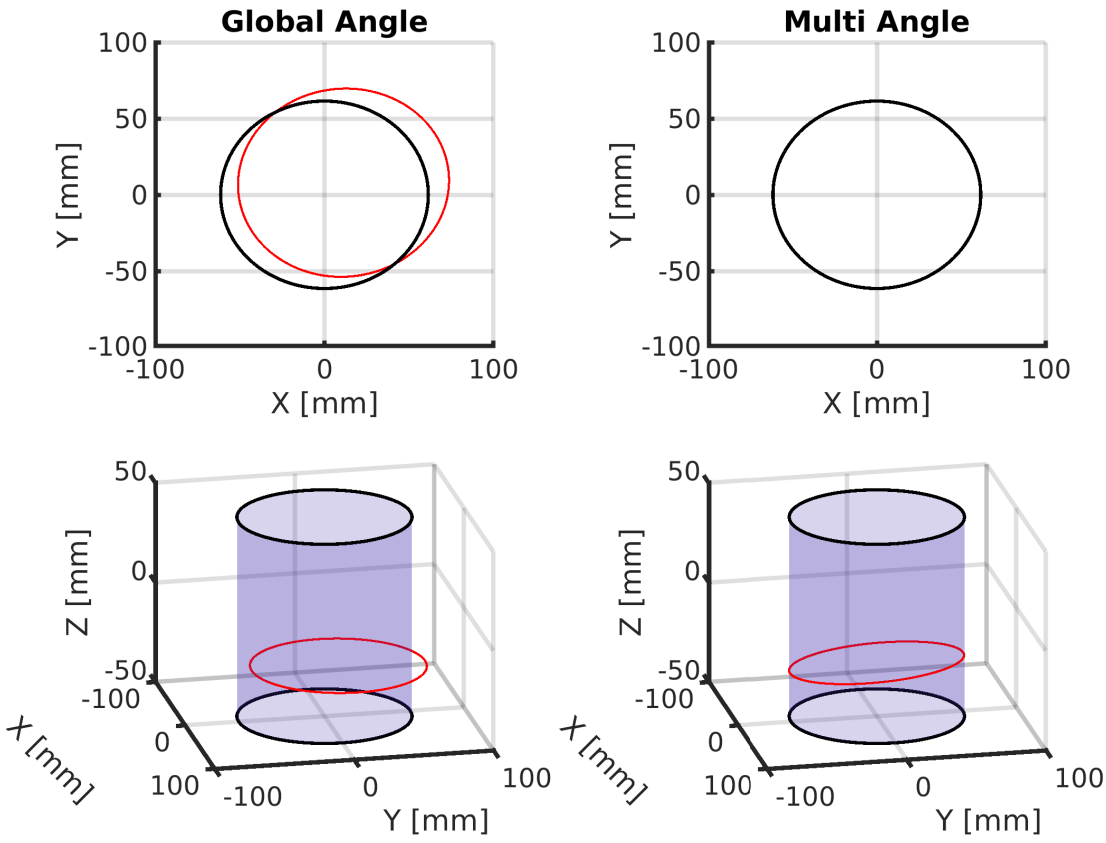

Figure 4.19: *Calibrated and un-calibrated laser extraction at 4° misalignment within calibration block*

As the profiler is calibrated against the current calibration block to be able to compare its performance with the previous method of calibration it was tested across a series of pipes with radii: 37.41 mm, 50.90 mm, 57.20 mm, and 63.43 mm. Each pipe and angle combination consisted of 10 sample images with the probe repositioned within the pipe between each frame. Due to not knowing the precise position of the profiler within the pipes only the radius error was be measured. The resulting errors for both the Multi Angle or calibrated and Global Angle are detailed in Figure 4.20.

Average error with Multi angle (corrected): $-0.29\,\mathrm{mm}$

Average error with global angle (uncorrected): $2.19\,\mathrm{mm}$

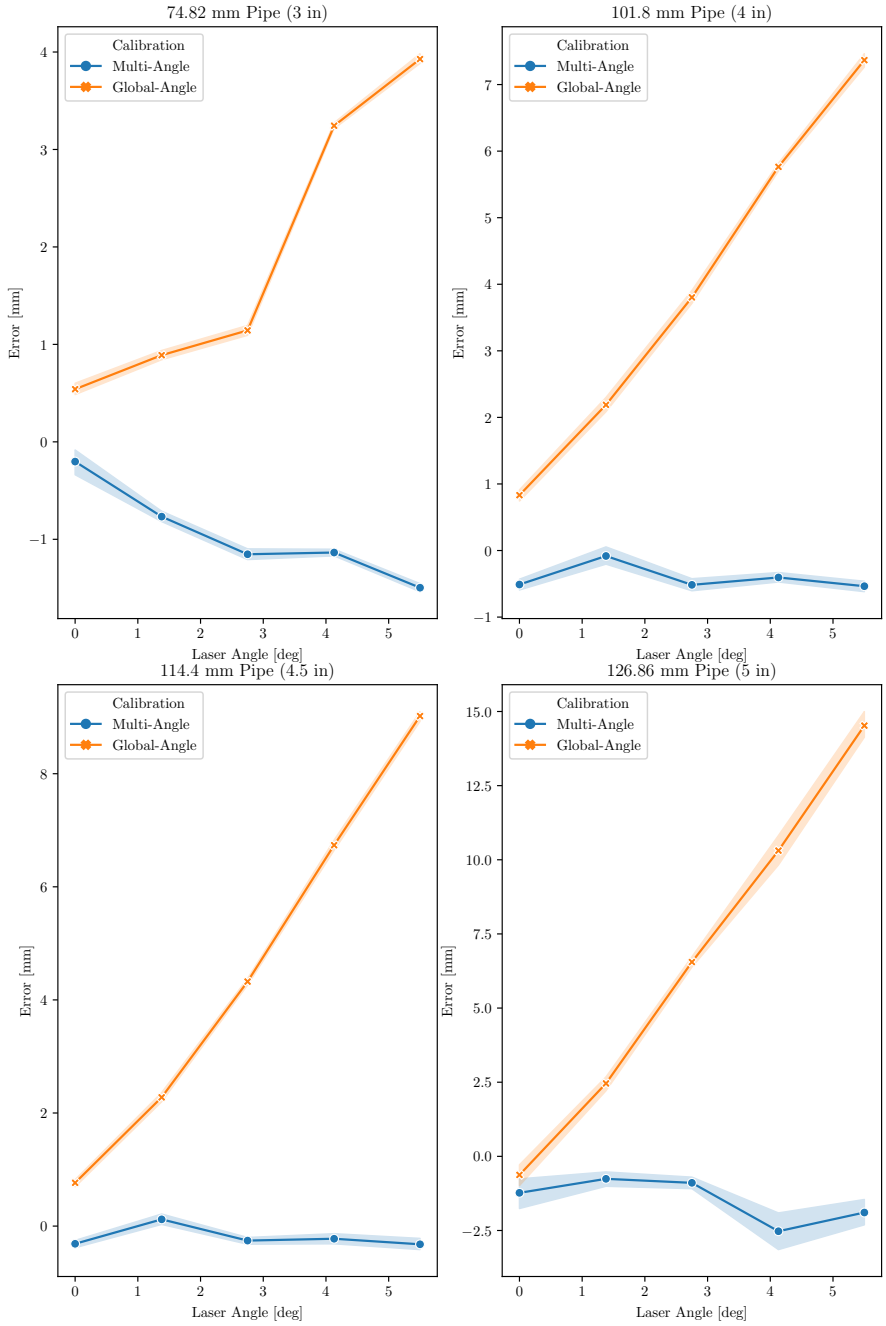

Figure 4.20: *Grouped error plots of pipe diameter sizing for increasing misalignment angles of laser profiler*

4.8 Comparison to Ground Truth Model

To determine the suitability of the calibration method and laser profiler for practical applications, a controlled scan was performed over a split pipe test sample with flat bottom hole defects as shown in Figure 4.21.

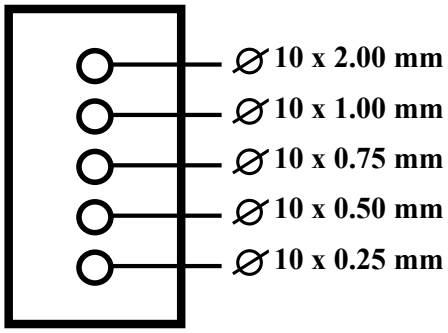

Figure 4.21: *Technical drawing of split pipe sample*

The reference scan which the results will be compared to was generated by a GOM ATOS Triple Scan structured light metrology system, capable of providing accuracy of 20 µm [123]. The probe shown in Figure 4.6 was mounted onto a robotic end effector and driven centrally through the split pipe recording alternating LED and laser images to simulate manual deployment in a repeatable fashion.

The LED images were processed to provide the positioning of the laser scanner within the pipe using feature-based matching [124], it has been previously shown that this technique is capable of providing positional feedback accurately to 0.01 mm per mm travelled [109]. Each laser image from the recording had the laser line projected into 3D space using both the Global and Multi Angle calibra-

tion methods, this process produced a series of rings which were then translated in space using the corresponding positional information obtained from the LED image set.

Comparison with the GOM model was made possible by meshing the extracted points utilising the algorithm detailed in [125]. This meshing algorithm remains true to the original data as each point directly becomes a vertex on the mesh. A drawback of meshing the data is that error is introduced around the edges of the holes due to the steps between consecutive rings creating a slope into the hole as opposed to a discrete change. Resulting deviation maps are shown in Figure 4.22, these deviation maps are created by GOM Inspect Software which was also used to align the ground truth and laser scan mesh prior to calculating the deviation. A full set of results is appended as Chapter A.

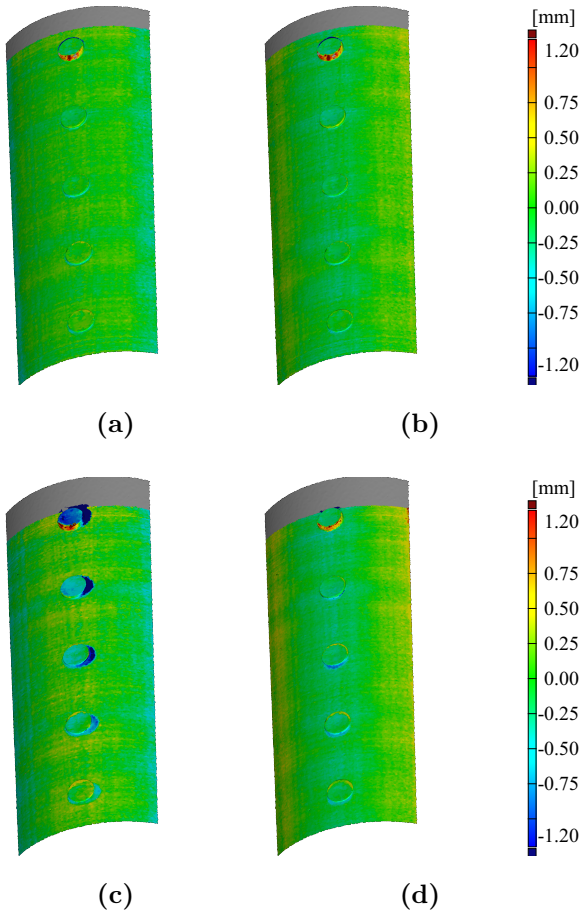

Figure 4.22: *Deviation maps showing error between generated mesh and ground truth scan (a) shows the Global Angle calibration error at 0 degrees misalignment and (b) shows the Multi Angle, (c) shows the Global Angle calibration error at 5.5 degrees and (d) shows the equivalent using Multi Angle calibration*

From the deviation maps it is clear that in conditions of misalignment the correct aspect ratio of the flat bottom holes is lost with an over-sizing of diameter in the horizontal dimension. The accuracy of the axial dimension is determined by that of the visual odometry in both cases of aligned and misaligned. In depth sizing the largest errors were observed on the 10 x 2 mm flat bottom hole this data is presented in Table 4.1. In the table where 'All' refers to the mean and standard

deviation error of the entirety of the sample, the error for the flat bottom holes consists of the mean error and standard deviation for a patch of selected points centred in the hole as shown in Figure 4.23. It is observed that under maximum misalignment the calibration approach proposed reduces diameter errors of a 10 mm hole from 2.50 mm to 0.27 mm and depth measurements of a 2 mm deep hole from −0.96 mm to −0.21 mm.

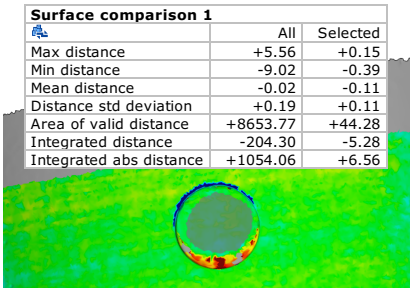

Figure 4.23: *Example measurement of the mean error and std. deviation for a patch centred on the 10 × 2 mm diameter hole*

Diametric error was calculated by observing the error along a plane that intersected the widest section of the hole with the error points taken at the upper edge of the flat bottom hole prior, shown graphically in Figure 4.24.

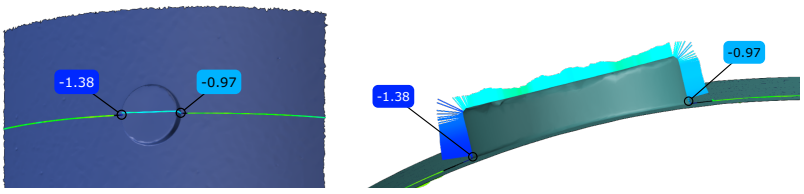

(a) **(b)**

Figure 4.24: *Example measurement of diameter error along a plane intersection through the midpoint of the 10 × 2 mm diameter hole, (a) shows the front view, (b) shows the top view*

Table 4.1: *Split pipe error for laser profiler measurements compared to GOM scan*

	Global Angle				
	All		10 × 2 mm Hole		
Misalignment [deg]	Mean [mm]	SD. [mm]	Mean [mm]	SD. [mm]	Diam. Err. [mm]
0	-0.02	0.19	-0.11	0.11	0.20
1.4	-0.04	0.26	-0.32	0.09	0.77
2.8	-0.04	0.26	-0.51	0.11	1.46
4.1	-0.05	0.40	-0.72	0.08	2.28
5.5	-0.04	0.49	-0.96	0.12	2.50

	Multi Angle				
	All		10 × 2 mm Hole		
Misalignment [deg]	Mean [mm]	SD. [mm]	Mean [mm]	SD. [mm]	Diam. Err. [mm]
0	0.02	0.22	-0.16	0.08	0.16
1.4	0.01	0.22	-0.19	0.07	0.22
2.8	0.03	0.19	-0.20	0.12	0.20
4.1	0.04	0.30	-0.21	0.06	0.17
5.5	0.05	0.38	-0.21	0.06	0.27

4.9 Summary

A calibration and accuracy study of a pipe laser profiler was carried out, this was performed in relation to systematic errors arising from tolerances encountered during assembly of the optical elements. The specific tolerance that was investig-

ated was the angular misalignment of the conical mirror which projects the laser onto the circumference of the pipework under inspection. A process for aligning the optical elements in translation and orientation was presented which allowed for the angular error to be studied at known points of misalignment. This confirmed the theoretical understanding that the error would manifest itself as a significant translation (15.8 mm at 5° within a 120 mm diameter sample) of the imaged specimen as well as a radius mismeasurement (1.5 mm). When comparing the results to a ground truth model the calibration algorithm on 5° misalignment reduced the diameter errors observed for a 10 mm hole from 2.50 mm to 0.27 mm. The depth measurement error for a 2 mm deep hole was reduced from −0.96 mm to −0.21 mm. These results highlighted the need for a method to align the optical elements within the profiler to ensure the high levels of accuracy demanded of such systems.

Once aligned using the procedure given, this error was reduced to 0.12 mm in positional error and 0.05 mm in radius error. In practice it is not always possible to manually adjust the optical elements within a laser profiler. Due to this, a calibration procedure has been developed by taking advantage of the precisely known location of the profiler within the calibration artefact. By knowing the location of the profiler and assuming the conical mirror is accurately machined, model parameters can be calculated at a finite number of steps around the laser profile image. It is feasible that this process could be integrated into the production work flow of the laser profiler, with each device paired with a unique calibration data file.

At 4° of misalignment this calibration procedure was shown to correctly re-project the laser ring within the calibration artefact and when tested on pipe samples with radii ranging from 37.41 mm, to 63.43 mm reduced the error on average from 2.19 mm to 0.29 mm. This new software-based calibration approach will be integrated into the deployment system providing accurate dimensioning capability for future industrial internal pipework inspections.

Chapter 5

Industrial Demonstrator

5.1 Introduction

In this chapter the pipe profiler's performance was verified and the software and hardware package being trialled in industry will be presented. The performance of the probe was verified using a split-pipe sample fabricated by National Nuclear Laboratory (NNL). The sample contained a range of defects which allowed for verification of the laser-profiler's accuracy. The split-pipe was manufactured out of a representative grade of stainless steel as used frequently around nuclear plants, allowing for the visual odometry to be tested as well. The defects were chosen and manufactured by NNL to be representative of typical defects to be found within the target pipework. Following on from this the hardware and software will be presented. The software is capable of processing the incoming images in real-time, the LED images are unwrapped and stitched together - providing the operator with a clear overview of the pipe internals. Laser images are processed in two ways, the laser is extracted, unwrapped and overlaid onto the image providing and intuitive depth reading. In addition to this using the methodology presented in Chapter 4 the laser is ring is projected into world coordinates and

displayed alongside the stitched image. A method for correcting for distortion in the case where the probe is not central within the pipe is also presented, this allows for the creation of stitched image results in a wider range of scenarios where the probe may deviate from the centre of the pipe.

5.2 Case Study: Split Pipe

To validate the systems performance a mock inspection of a split pipe sample was undertaken. On one half the pipe defects consisted of flat bottom holes and slots. The opposing side the sample consists of more realistic defects such as containing pitting and light corrosion. A schematic of the sample is shown in Figure 5.1. In the initial trials the probe was deployed down the pipe in controlled 0.5 mm steps taking an LED and laser image at each location. A log polar unwrapping of each of the images was performed and these were then stitched together using Scale-Invariant Feature Transform (SIFT) matches to determine the Y pixel change between them. With each consecutive image appended to the previous image set at a distance equal to the aforementioned Y pixel change. Forming a stitched image of the internal pipe bore. As the probe was kept central within the pipe this resulted in a high-quality result, under normal operation any movement from the centre would distort these images. Using the laser images, a point cloud was also constructed for each side of the split pipe, this was achieved by extracting the laser ring for each image and projecting into 3D space as described in Chapter 4, each image resulted in a single laser ring. These rings were spaced 0.5 mm apart

but they could have also been positioned using the SIFT data as the pixel to mm relationship was well established within the pipe as shown in the following section testing the system with manual.

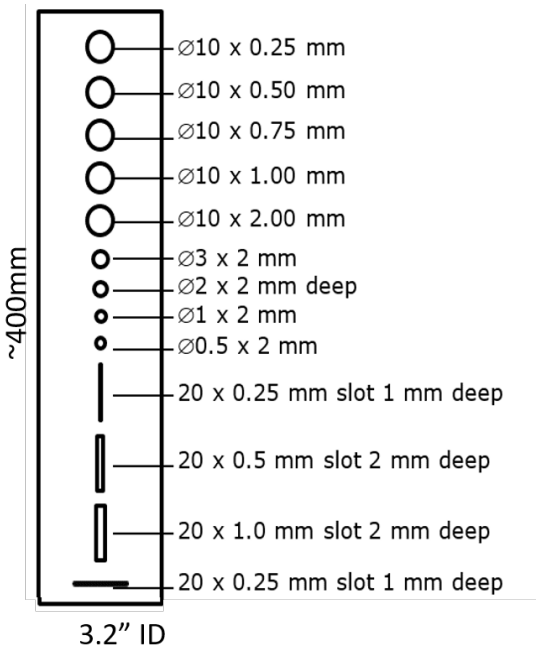

Figure 5.1: *Schematic detailing the defects machined on the split pipe sample*

A top down photo as well as the stitched image result for the artificial defect side of the split pipe is shown in Figure 5.2. Table 5.1 shows the defect descriptions and the measurements for each of these taken manually from the point cloud. The GOM measurements were also taken from the STL model manually, this leads to some variation in the readings, the errors given in Table 4.1 from Chapter 4 are therefore a better representation of system accuracy when compared to the GOM. The stitched image and point cloud are split into groups of defects and are shown in Figures [5.5 – 5.9].

In addition to this a set of measurements were taken with a probe rated to IP67 [107] as shown in as shown in Figure 5.3, this was deployed manually through the pipe in a realistic scenario. However, the quality of the stitched images is reduced due to aberrations through the sapphire as well as reflections from both the LED and the laser projector. The measurements from the point cloud showed a consistent under-sizing of defects due to a lack of accurate calibration, future work will address such issues. The stitched image and complete point cloud are shown in Figure 5.4.

(a) **(b)**

Figure 5.2: *(a) Shows a top down photo of the split pipe taken with a standard camera, (b) shows the unwrapped and stitched images taken from the inside of the pipe*

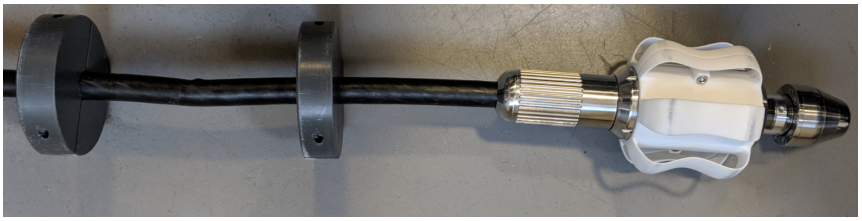

Figure 5.3: *Probe with sapphire window as deployed through split pipe test specimen*

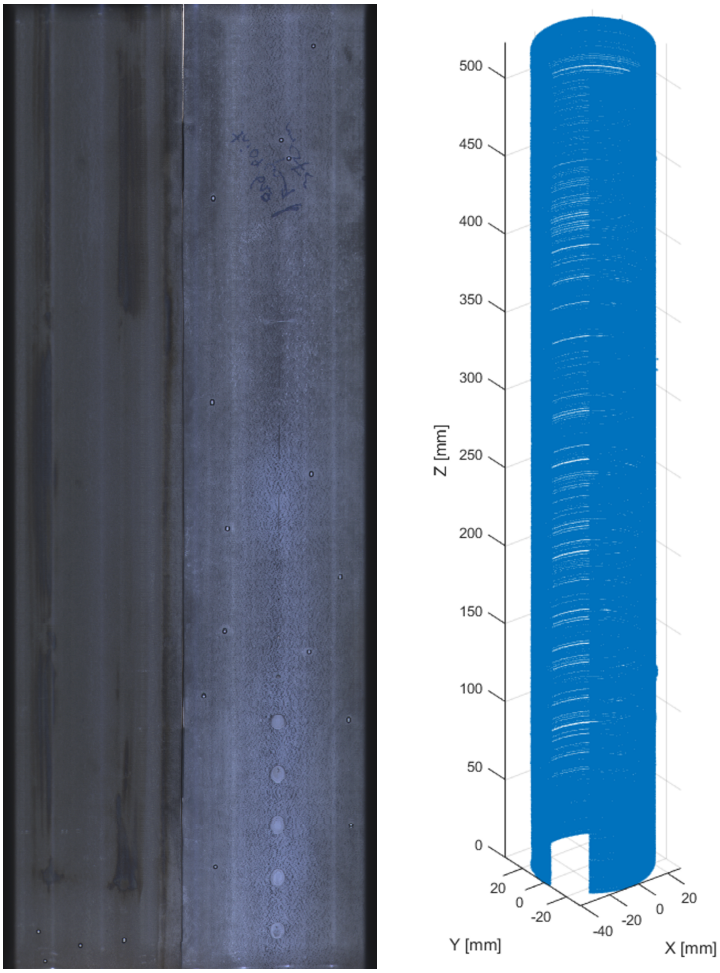

(a) **(b)**

Figure 5.4: *Results of manually deployed probe with sapphire window (a) shows the stitched image section of the split pipe sample, (b) shows the point cloud*

Table 5.1: *Point cloud measurements of split pipe machined defects*

Defect ID	Design Size	GOM Measurement	Measurement from Point Cloud
1	Circumferential Slot (20 x 0.25 x 1 mm)	19.52 x 0.52 x (Can't Size) mm	18.4 x 0.5 x (Can't Size) mm
2	Axial Slot (20 x 1 x 2 mm)	20.02 x 1.01 x 1.81 mm	19.5 x 0.81 x 1 mm
3	Axial Slot (20 x 0.5 x 2 mm)	20.07 x 0.56 x (Can't Size) mm	19.5 x 0.64 x 2 mm
4	Axial Slot (20 x 0.25 x 1 mm)	19.78 x (Can't Size) mm	19.5 x 0.36 x 0.74 mm
5	Flat Bottom Hole (0.5 OD x 2 mm)	Can't Size	Can't Size[1]
6	Flat Bottom Hole (1 OD x 2 mm)	Can't Size	0.85 OD x 0.4 mm
7	Flat Bottom Hole (2 OD x 2 mm)	1.8 OD x (Can't Size)	1.8 OD x 1.9 mm
8	Flat Bottom Hole (3 OD x 2 mm)	3.17 OD x 1.98 mm	2.79 OD x 1.9 mm
9	Flat Bottom Hole (10 OD x 2 mm)	9.74 OD x 2.17 mm	9.7 OD x 2 mm
10	Flat Bottom Hole (10 OD x 1 mm)	9.80 OD x 1.06 mm	9.6 OD x 1.01 mm
11	Flat Bottom Hole (10 OD x 0.75 mm)	9.91 OD x 0.86 mm	9.48 OD x 0.78 mm
12	Flat Bottom Hole (10 OD x 0.5 mm)	9.78 OD x 0.64 mm	9.72 OD x 0.57 mm
13	Flat Bottom Hole (10 OD x 0.25 mm)	9.81 OD x 0.42 mm	9.66 OD x 0.63 mm

[1]The defect was below the resolution of the laser scan and was unable to be sized, the defect is however visible in the high resolution stitch as observed in Figure 5.7a

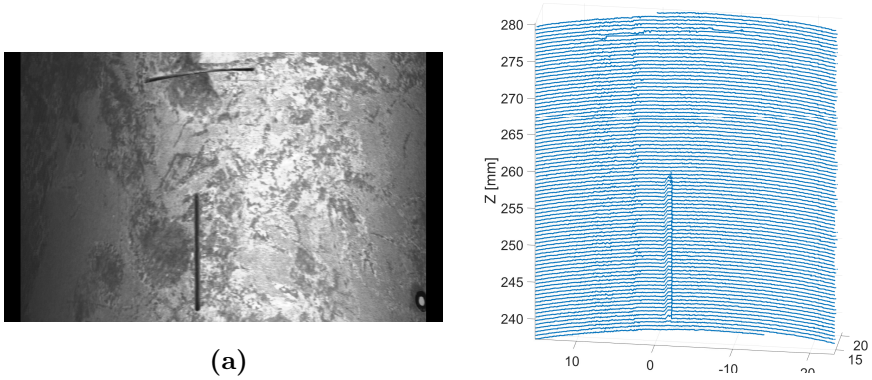

(a) **(b)**

Figure 5.5: *(a) Shows the stitched image section detailing defects 1 & 2, (b) shows the point cloud for defects 1 & 2*

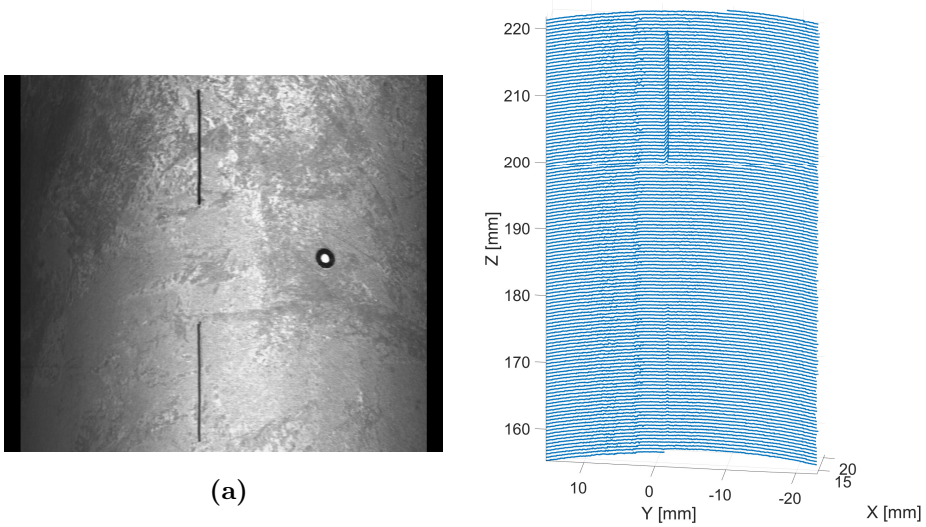

(a) **(b)**

Figure 5.6: *(a) Shows the stitched image section detailing defects 3 & 4, (b) shows the point cloud for defects 3 & 4*

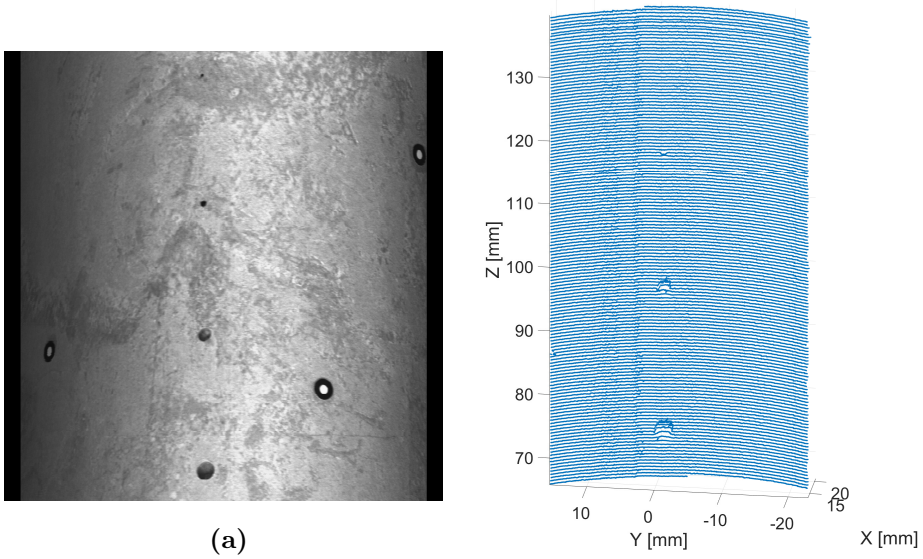

(a) **(b)**

Figure 5.7: *(a) Shows the stitched image section detailing defects 5, 6, 7 & 8, (b) shows the point cloud for defects 5, 6, 7 & 8*

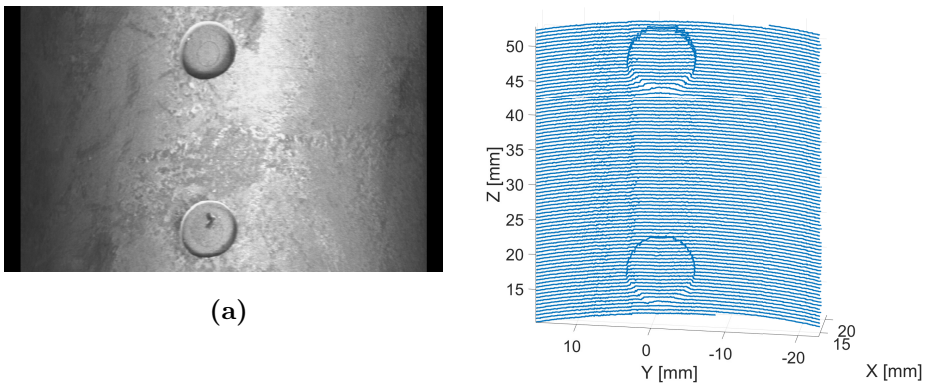

(a) **(b)**

Figure 5.8: *(a) Shows the stitched image section detailing defects 9 & 10, (b) shows the point cloud for defects 9 & 10*

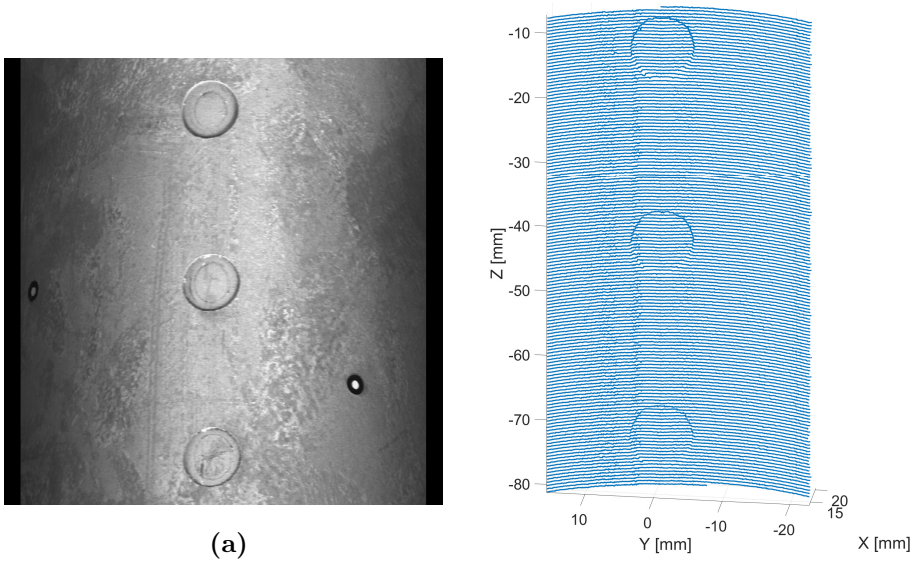

(a) **(b)**

Figure 5.9: *(a) Shows the stitched image section detailing defects 11, 12 & 13, (b) shows the point cloud for defects 11, 12 & 13*

The defects on the opposing side of the pipe were created with chemical methods as opposed to being machined, and as such precise geometry to draw comparisons to was not available. They do however indicate that the system is capable of detecting realistic defects. A top down image of the corroded side of the pipe and the corresponding stitched result is shown in Figure 5.10. A close up of the corrosion above defect 1 as indicated by Figure 5.10 is shown in Figure 5.11. No discernible wall thickness loss was detected for this region. A summary of the three defects is given in Table 5.2. The stitched image sections and point clouds are shown in Figures [5.12–5.14] for these defects.

Table 5.2: *Point cloud measurements of split pipe "natural" defects*

Defect ID	Description	Measurement from Point Cloud
1	Pitting	2.8 x 0.48 mm
2	Pitting	1.5 x 0.36 mm
3	Pitting	3.2 x 0.51 mm

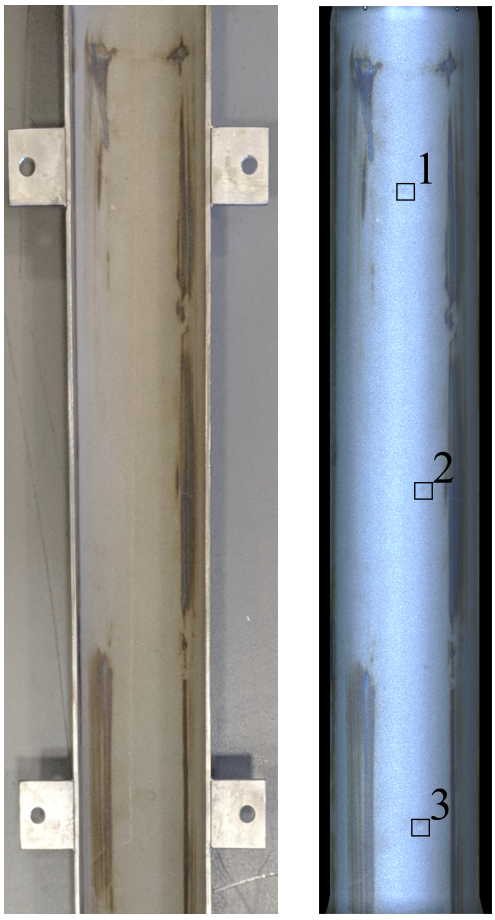

(a) **(b)**

Figure 5.10: *(a) Shows a top down photo of the split pipe taken with a standard camera, (b) shown the unwrapped and stitched images taken from the inside of the pipe*

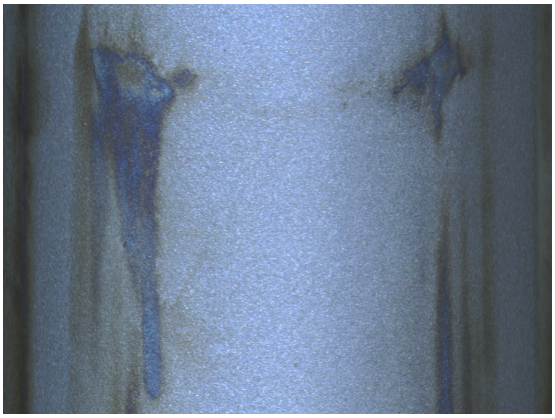

Figure 5.11: *Close up detail from stitch of corroded pipe section*

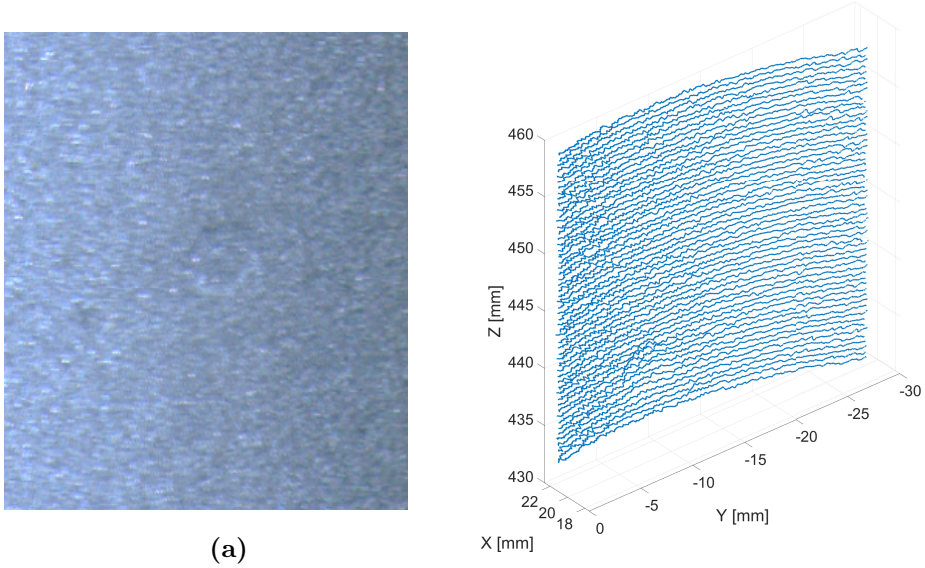

(a)

(b)

Figure 5.12: *(a) Shows the stitched image section detailing defect 1, (b) shows the point cloud for defect 1*

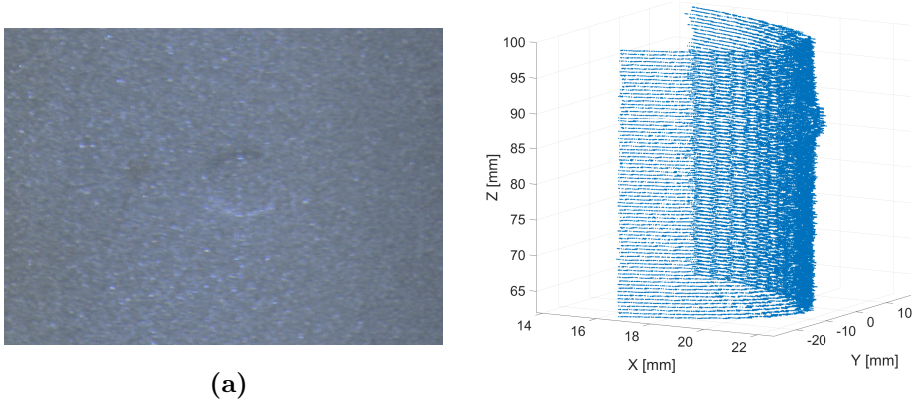

(a) **(b)**

Figure 5.13: *(a) Shows the stitched image section detailing defect 2, (b) shows the point cloud for defect 2*

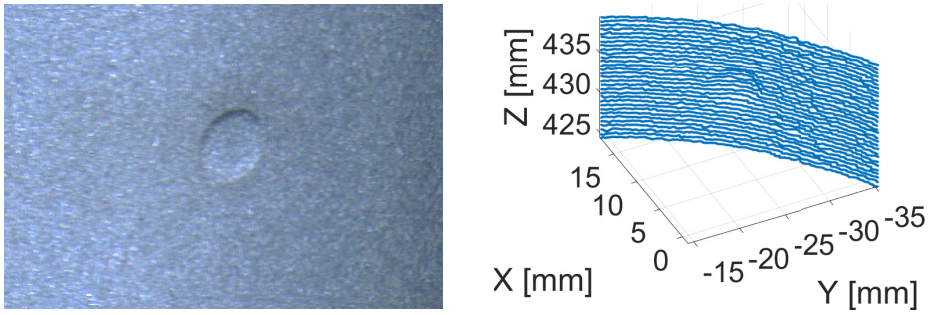

(a) **(b)**

Figure 5.14: *(a) Shows the stitched image section detailing defect 3, (b) shows the point cloud for defect 3*

5.2.1 Summary of Split Pipe Results

The results have shown the limitations of the system generally come down to two factors when sizing defects:

1. If a defect is less than the width of the laser such as the smallest flat bottom hole (0.5 OD x 2 mm id: 5) and the circumferential slot (20 x 0.25 x 1 mm id: 1) a depth measurement is not possible.

2. The axial resolution is largely determined by the step size between images in the case of the first set of experimental data this was fixed at 0.5 mm. In the manual deployment this value varied, therefore when performing inspections, the maximum speed of deployment will not only be determined by the image quality and feature matching requirements covered in Chapter 3 but the axial resolution desired.

It is also noted however, that the image quality when using the sapphire window is degraded when compared to the previous results, this also presented itself with an increase of stitching artefacts.

5.3 Real-Time Software

5.3.1 Overview

A software package for the system has been developed by the author for industrial usage. This provides a simple interface for using the pipe profiler presented in this thesis allowing for image stitching and laser profiling. The software can be broken down into its main components which are shown in the simplified flow diagram in Figure 5.16 a screen-capture of the software is shown in Figure 5.15. The central section of the software shows a continuous stitch of the pipework

under inspection, a green border is overlaid detailing the live region of the image. Furthermore, the laser line is also extracted and displayed onto the image. Axes are added to the image showing the scale of the stitched section on screen, the Y-Axis is given by visual odometry calculated from SIFT matches. The X-Axis is given by the circumference of a circle fitted to the laser ring when projected into 3D space. The left section of the interface shows a graphic of the probe within a pipe with the maximum positive and negative distance travelled within the pipework as well as a rectangle showing where within that section the current on-screen display is. In the top right an orientation display is shown showing information captured by the Inertial Measurement Unit (IMU). Below this are the basic controls for the software and adjustments to the camera centre to correct for offsets which may result in distorted images when applying the unwrapping. The laser data is also plotted here showing the laser line in X, Y in mm cartesian coordinates. Finally, a traffic light system is used to indicate to the user the number of SIFT matches between successive frames, this generally occurs when the movement is erratic or too fast. Alternatively, it may indicate the current region under inspection is sparse of reliable features.

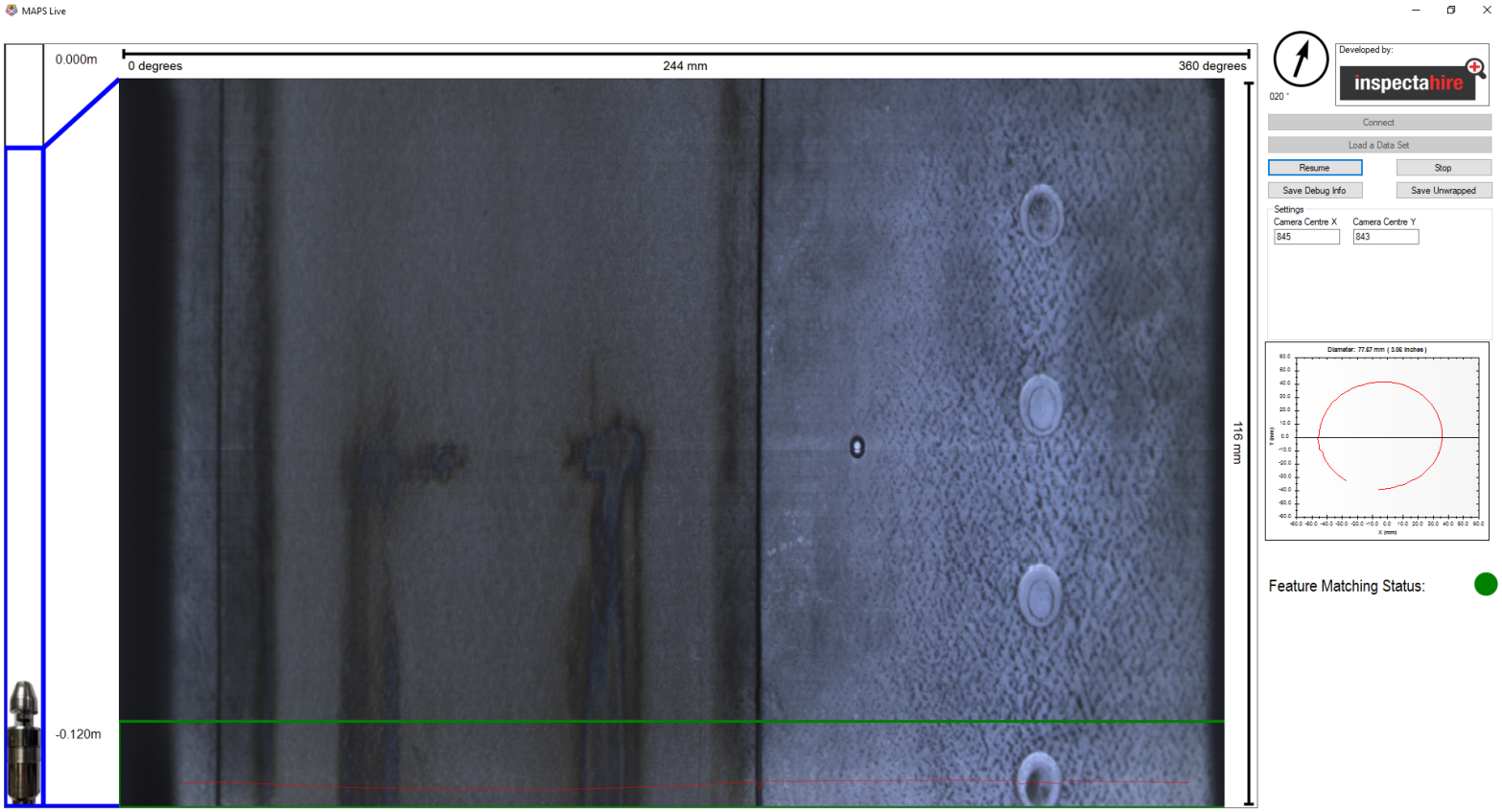

Figure 5.15: *Screenshot of the pipe profiling software interface*

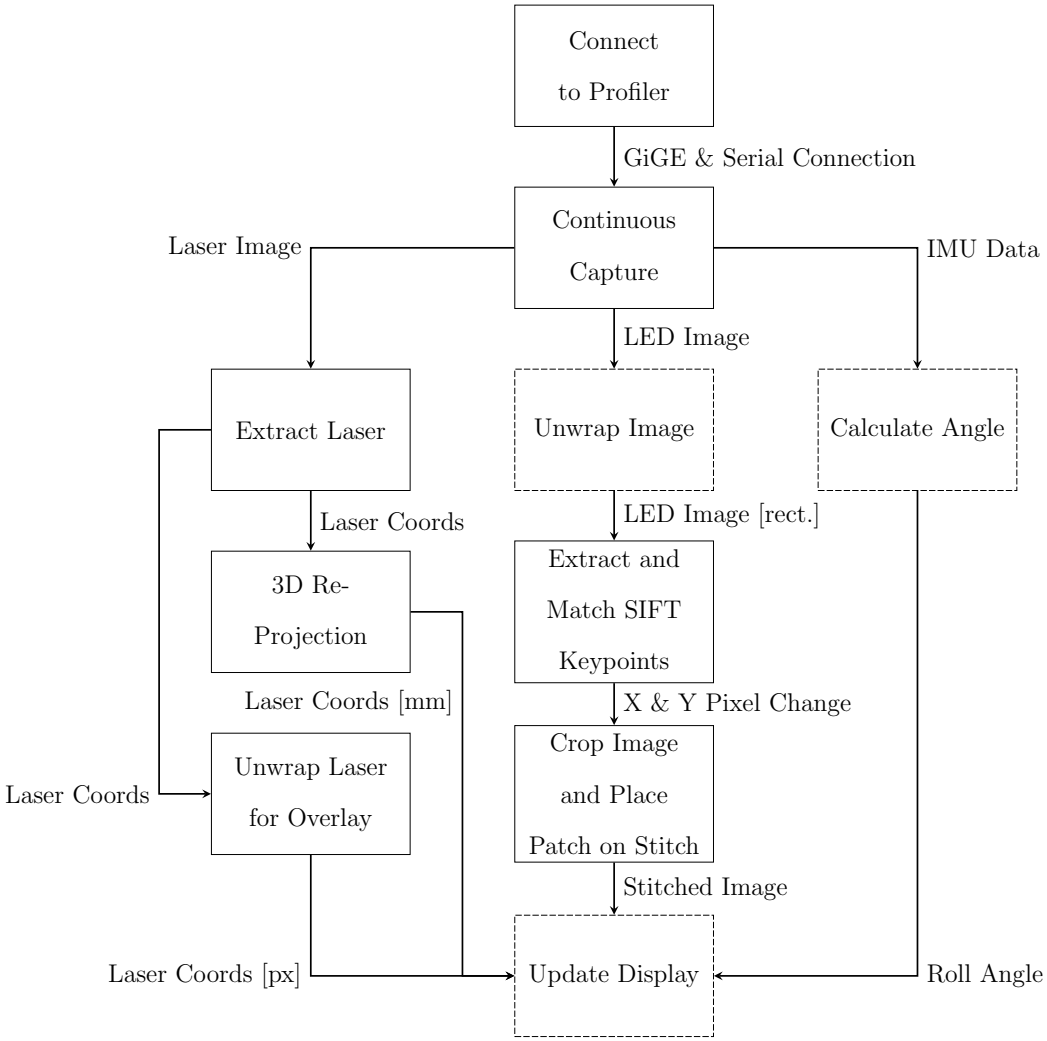

Figure 5.16: *Simplified operation of real time pipe-profiling software (dashed outline indicates modules resulting from significant collaborative work)*

5.3.2 Technical Overview

The software was written in a modular way with the frontend, data capture and storage handled using C# .Net 4.7. The image processing is handled by two Dynamic Link Libraries (DLL) written in C++ for computational efficiency.

Further to the use of C++ a CUDA [126] implementation of SIFT is used, CUDA is a parallel computing platform developed by NVIDIA for use on their GPU devices.

5.3.2.1 Laser Processing

Laser images as shown in Figure 5.16 are processed in two ways, the 3D re-projection is an implementation of the methodology shown in Chapter 4 in C++. Returning the diameter of the pipe bore as well as a series of X, Y coordinates in millimetres which are charted as shown in Figure 5.15. The second method is simpler and applies the log-polar unwrapping of the fisheye image upon the laser coordinates to allow them the be overlaid on the corresponding LED image.

5.3.2.2 Image Stitching

Image stitching with minor exceptions is completed on an image to image basis. Each image is first unwrapped using a log-polar unwrapping method to convert from the fisheye 'doughnut' image of the pipe to a rectangular form. SIFT feature extraction and matching is then performed on consecutive frames. This is handled by another C++ Dynamic Link Library (DLL). It contains a wrapper for a CUDA implementation of SIFT [127] which was configured using the parameters given in Chapter 3 as well as the logic and functionality for the stitching procedure. The matching process returns a series of X & Y pixel correspondences the median value for these was taken. As the probe was assumed to only be able to travel along its axis within the pipe (Y pixel change) and roll around this axis (X pixel

change), these two values could be used to create the high-quality results shown in Figure 5.15. The Y pixel change is incorporated into the stitch by cropping the middle section from the latest image and placing it at that distance from the current active edge. The X pixel change is applied as a circular shift to the image matrix. Utilising the CUDA implementation and leveraging the processing capabilities of consumer level GPUs allowed this image stitching process to perform in real-time which is a key selling point of the system.

5.3.3 Deployment

A long with the intuitive software allowing inspectors to collect data for post processing and analyse defects in real time, a robust package in-line with industry standards was created to allow Inspectahire to perform on-site deployments and demonstrations. This is illustrated in the following Figure 5.17. The package contained a pipe sample with flat-bottom hole defects, the pipe-profiler, flexible deployment cable, centralisers, V-Blocks, power supplies required for the equipment and a laptop with a CUDA capable graphics card.

(a)

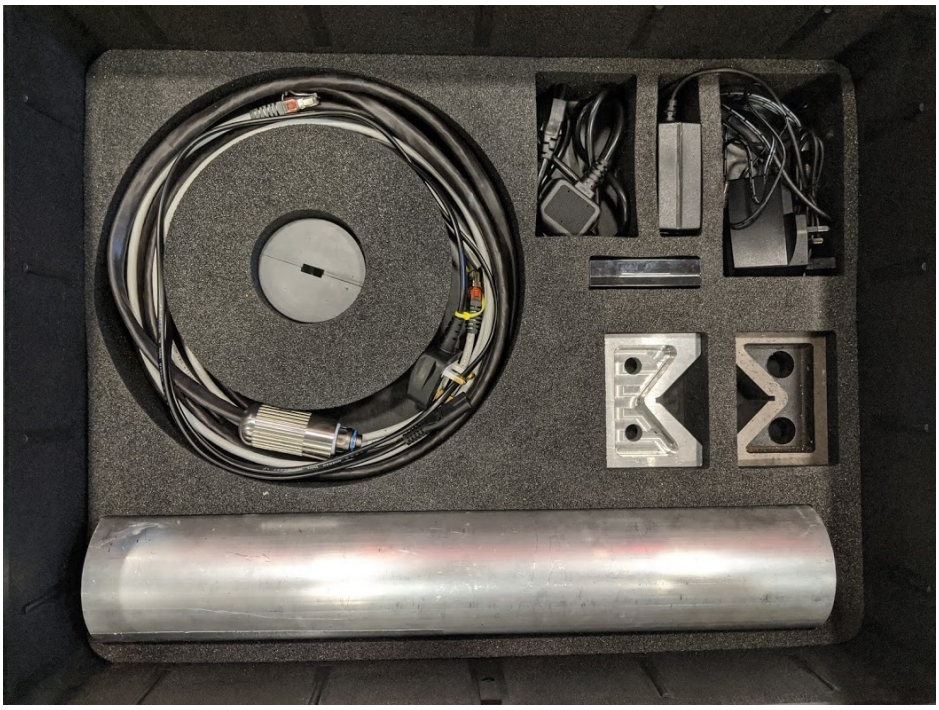

(b)

Figure 5.17: *Pipe-Profiler deployment case containing equipment for demonstration and inspection*

5.4 A Novel Centralisation Method for Pipe Image Stitching

In this section, a brief overview will be given of the collaborative work the author took part in [128]. The work created a method to unwrap images from a non-centralised view point with minimal distortion. The author provided support to all areas of the work contained within the paper as the resident expert on the system used, the key technical contributions were the sensitivity study completed and detailed in this section, and the data collection & experimentation. To achieve this the first step was determine to probe's orientation within the pipe was devised by utilising the extraction of the laser ring and an optimisation method. From the known orientation the image can be re-projected into a synthetic centralised view, from here the image can be unwrapped and stitched as done in the previous section.

To demonstrate the effects of distortion of unwrapping an image from a non-central perspective the following Figure 5.18 is shown, this is as if a grid pattern has been imaged on the inside and unwrapped from a centralised perspective (Figure 5.18a), a non-central perspective (Figure 5.18b) and finally the non-central perspective having been re-projected to a centralised perspective (Figure 5.18c).

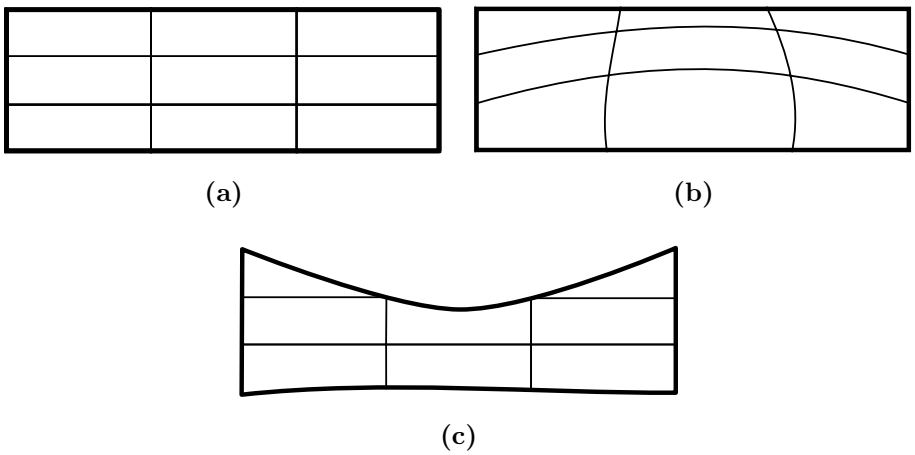

Figure 5.18: *Simplified cases of a grid like pattern being unwrapped, case (a) shows an image taken with the probe centralized, case (b) shows an expected result performing standard log polar unwrapping on a non-centralized probe without correcting for pose and case (c) shows the expected result when correcting for the pose*

The first step of the retrojection process is to determine the probe's orientation within the pipe of a known diameter. A 3D-schematic is shown in Figure 5.20 and a Simplified 2D-schematic in Figure 5.19. This is achieved through an optimisation process where the optimisation solves for the minimum difference between a simulated laser ring with the known camera model and profiler geometry and the extracted laser ring from the image. The solution is limited to x, y, and the rotation around these α and β respectively.

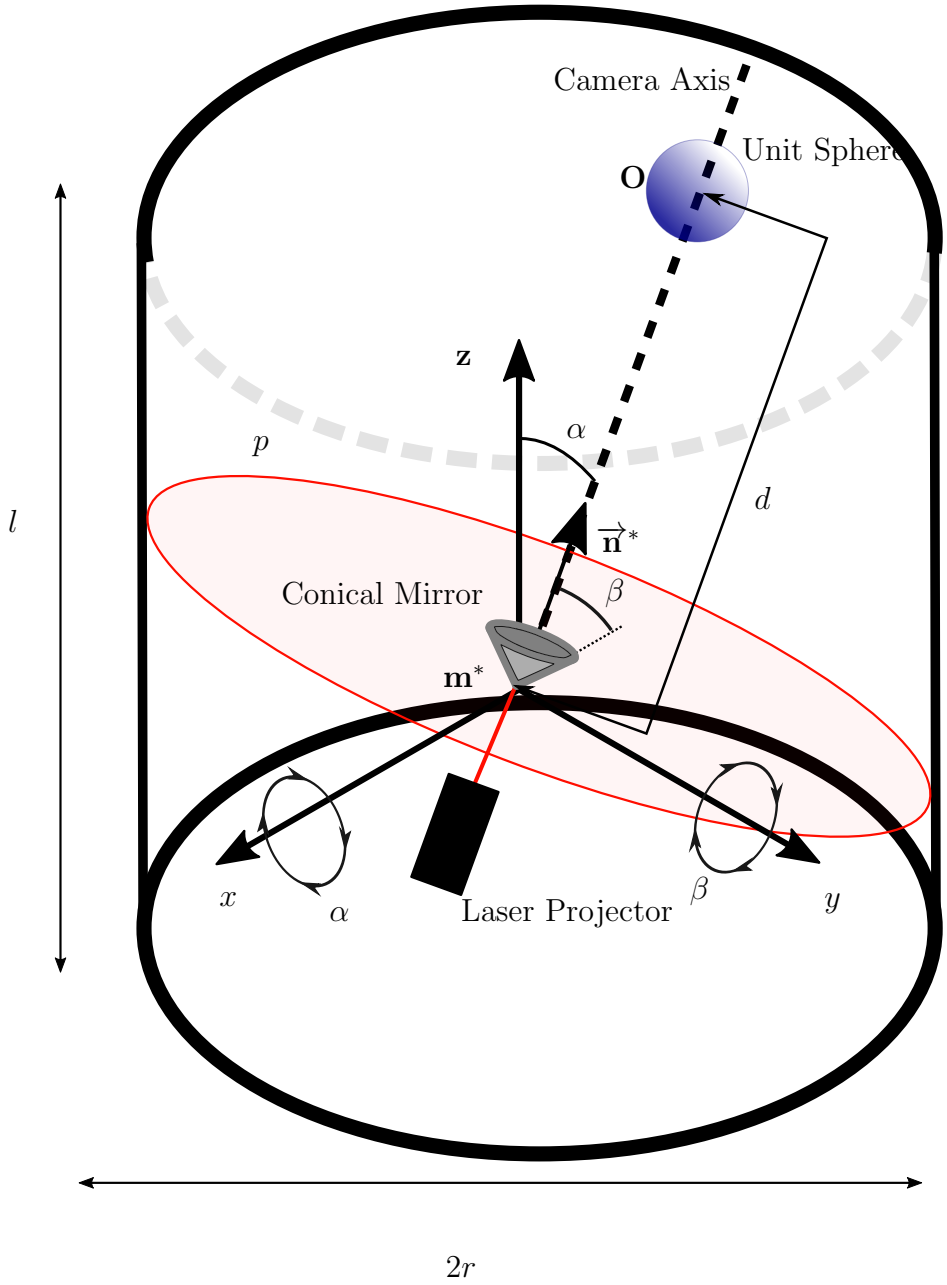

Figure 5.19: *Schematic detailing the camera system within a cylinder, d is the distance from the centre of the unit sphere as detailed in [18] to the point of reflection and origin of the laser plane* $\mathbf{m}$*,* α *is the rotation about the* x *axis and* β *the rotation around the* y *axis*

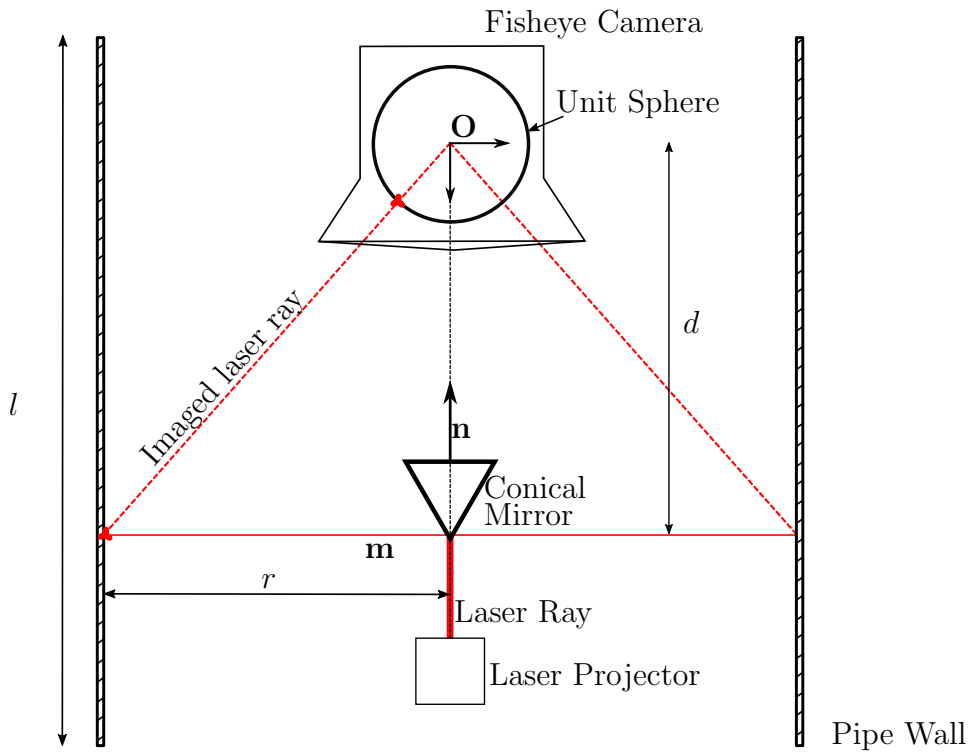

Figure 5.20: *Simplified two-dimensional schematic detailing the camera system centred within a pipe of diameter 2r. The dashed lines represent the rays of light observed by the camera at the intersection of the laser plane and pipe walls. The camera is represented by the omnidirectional camera model as detailed in [18].* **O** *is the camera origin located at the centre of the unit sphere, l is the length of the pipe,* **m** *is the origin of the laser plane at the point of reflection on the conical mirror and d is the distance between the camera origin and point of reflection*

A series of simulated laser rings with the various values of x, y, α and β is shown in Figure 5.21. The ability to determine the probe's pose is therefore a function of the change in the laser ring with respect to the parameters shown. To determine the sensitivity to change within a simulated environment the probe was moved in x and rotated around α, the laser ring was extracted in the centred and co-linear to the pipe within the environment, from here the maximum value

change at discrete points around the ring was noted to create a plot of pixel change ($\mathbf{\Delta PX}$) vs translation in x and rotation in α as shown in Figure 5.22. As observed the laser plane does not provide significant sensitivity to change for small pose changes, this is exaggerated when the translation and rotation oppose each other creating a region where they are effectively cancelled out. However, there is still a significant enough change for the optimisation to reach a solution to within 0.5 mm in translation for 90 % of cases with a simulated trial set of 300 poses.

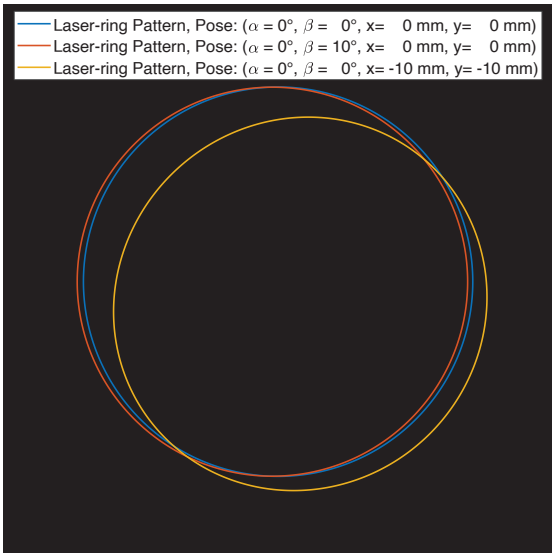

Figure 5.21: *Schematic detailing the camera system within a cylinder, d is th e distance from the centre of the unit sphere as detailed in [18] to the point of reflection and origin of the laser plane* $\mathbf{m}$*,* α *is the rotation about the* x *axis and* β *the rotation around the* y *axis*

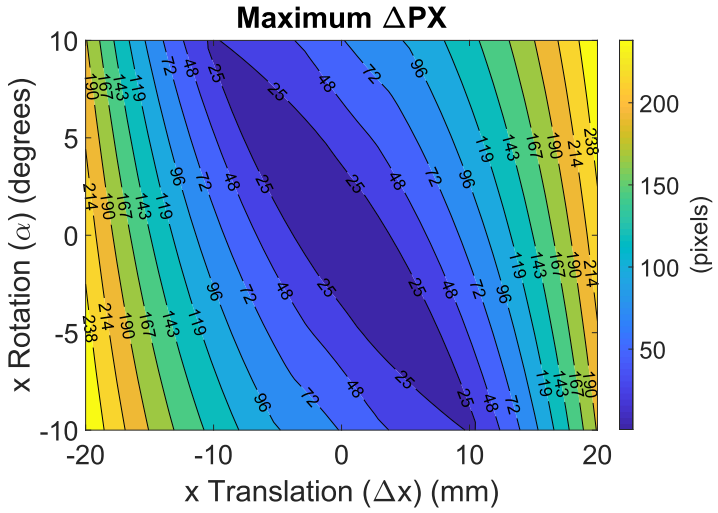

Figure 5.22: *Maximum* **ΔPX** *pixel changes within a* 65 mm *ID pipe for varying rotational and translational camera pose changes*

Once the pose is known, then the synthetic image for unwrapping can be created, this process is graphically in Figure 5.23.

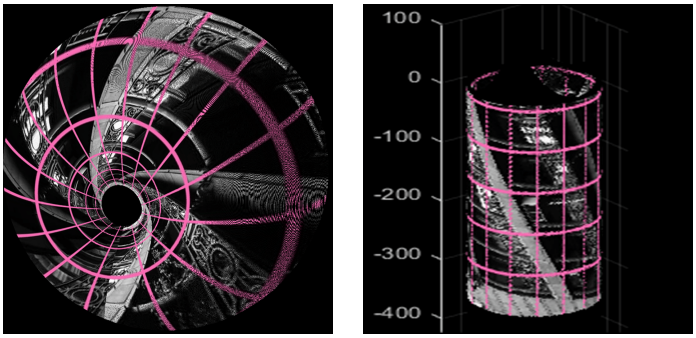

(a) **(b)**

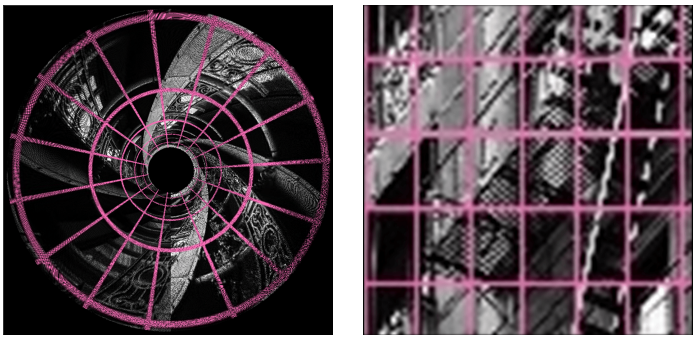

(c) **(d)**

Figure 5.23: *Unwrapping process diagram of non-centralized images. (a) is the input non-centralized raw image. (b) is the point cloud of the pipe created from the pose observed and the input image (a), (c) is the post-processed, centralized image using the point cloud (b). (d) is the unwrapped image resulting from (c)*

An example mock inspection of a pipe with a cross pattern off through holes was undertaken with the probe without a centraliser to create a dataset which was non-central, an example pair of images of the probe centralised and un-centralised within a pipe section are shown in Figure 5.24. The result of the image stitching from this data set without the re-projection applied to the images prior to stitching is shown in Figure 5.25a and the image with the re-projected centralisation applied is shown in Figure 5.25b

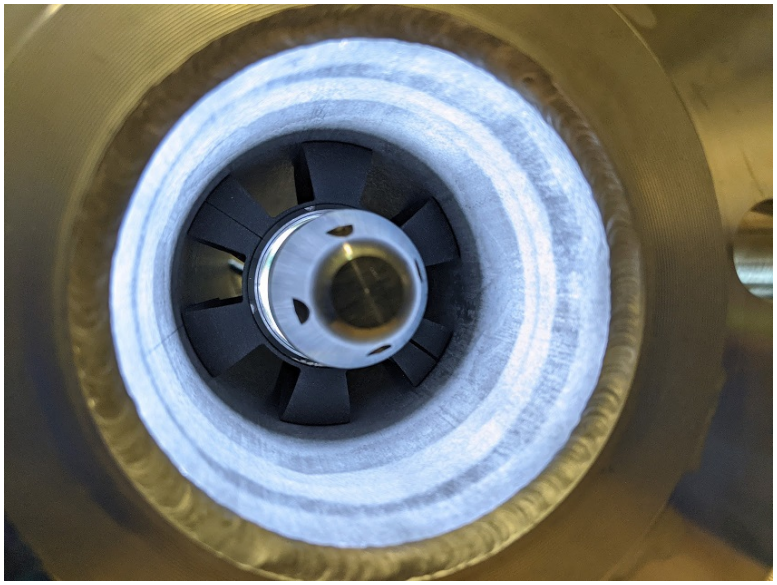

(a)

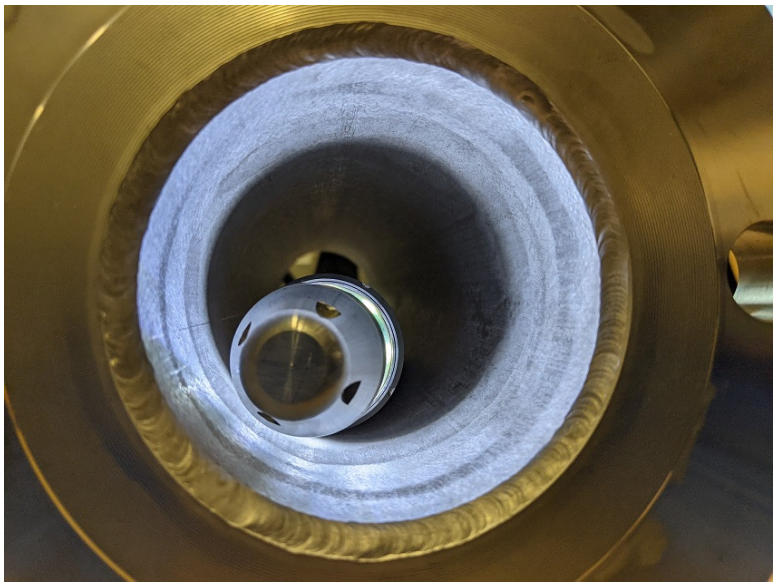

(b)

Figure 5.24: *(a) shows the probe with a centraliser within a section of pipe, (b) shows the probe without the centraliser demonstrating how the inspection data was captured*

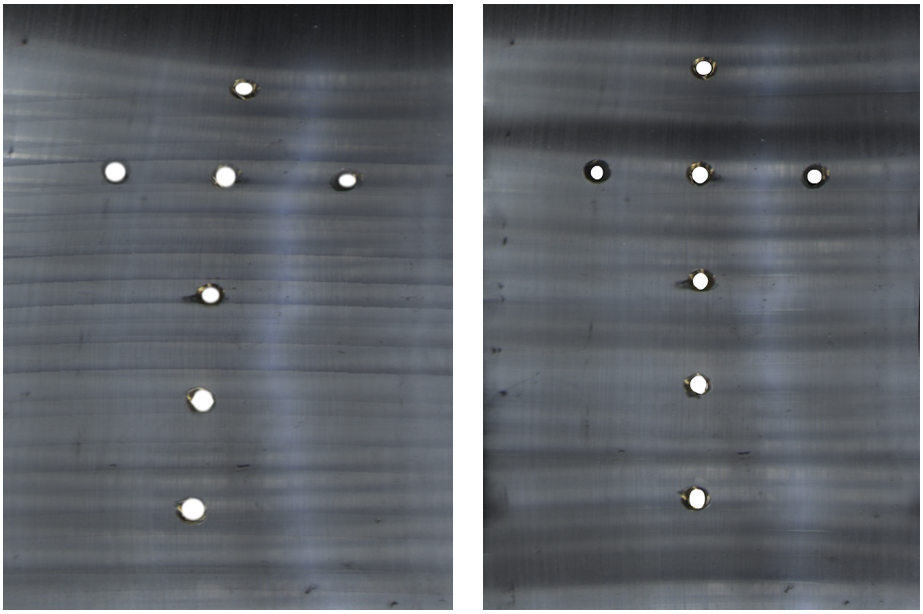

(a) (b)

Figure 5.25: *Image mosaic created from stitching 32 unwrapped images of 65 mm diameter pipe sections. (a) without centralisation (b) with post-inspection centralisation achieved through image re-projection prior to unwrapping*

5.5 Summary

In this chapter the practical aspects of the pipe profiler were investigated. In the first section the effectiveness of the image stitching and accuracy of the laser profiler was investigated with the use of a split-pipe sample. The image stitching was capable of providing high quality results with very few artefacts. The laser profiler was able to size most defects accurately within 0.5 mm. However, there were some key points to take note of, the axial accuracy was noted to be related directly to the deployment speed. Furthermore, small defects below the width

of the laser line as projected such as the circumferential slot and flat-bottomed holes with a diameter less than this could not accurately be sized in depth as the laser could not be accurately extracted from these regions. These defects were all imaged to a high resolution as shown in the images within the section. A deployment package and software solution were presented capable of providing, odometry information, stitched images and laser profiling to the operator in real time. Finally, a method for correcting the distortion due to non-centralised image unwrapping was shown which was capable of providing high quality stitched images in un-centralised mock inspection scenarios.

Chapter 6

Summary, Key Findings and Future Work

6.1 Summary

This thesis has presented an internal pipe-profiling system, the theory behind this & alternative methods of pipe inspection, an optimisation of the inspection parameters, and a calibration method and an industrial demonstration. The system has been designed to inspect pipes with a diameter of 50–150 mm. The system consists of a laser-profiler, providing diametric information and a fish-eye lens equipped camera, providing high resolution image stitches and odometry.

Chapter 1 began with an overview of the industrial motivation for such a system to be developed. The main point being made, that there is a large amount of pipework within critical infrastructure which will degrade over time, leading to corrosion, pitting, cracks and product build up. It was noted that these inspections are often carried out with traditional Remote Visual Inspection (RVI) which provides inspectors with a quick and easy screening method for providing an overview of the pipework's integrity. The advantages of the system presented

in this thesis to augment tradition RVI are then given such as the: unwrapped overview of the internal bore, diametric information and visual odometry data, allowing for quantitative comparisons with previous inspection data. Following this, the main aims, objectives and outline of the thesis were laid out, concluding with the contributions to academia & industry and the publications arising from this work.

Chapter 2 introduced the reader to the various methods of Non-Destructive Evaluation (NDE) available for the inspection of assets. A focus was then taken on visual inspection of pipework, with various diameter pipework considered in turn and the standard approaches to inspect them. This can be summarised in the following points:

- Below 50 mm diameter videoscope cameras may prove most effective.
- Medium bored pipes of 50 mm–250 mm diameter are best suited to a mix of push-rod cameras and crawlers.
- Larger than 250 mm usually require In-Line inspection & crawlers offering effective inspection deployment strategies.

Following on from this, the theory behind advanced methods of RVI was introduced, beginning with the camera model and calibration for both a pin-hole camera and omnidirectional camera. This led into epipolar geometry, which describes the projective geometry between two views. A section on 3D reconstruction was presented after this, with a key point being the uncertainty arising from parallel views which is largely the case for pipe inspection. Methods for creating 3D

reconstructions were then covered, this included stereo vision where correspondences between two views are used to triangulate a 3D point, and active stereo where the correspondence is simplified by replacing a second camera with a laser stripe for example. Time of flight systems were described; where these systems rely on the time taken for light to travel from the source or the phase to shift from emission through to reflection and detection to convey the depth of objects in the scene. Structure from Motion (SfM) was covered next, as the final 3D-reconstruction method to be presented. This technique allows for collections of unordered images of a scene to be processed into a model. The model may be scaled with the correct control points and calibrations in place. Visual Odometry was introduced at this point, as it is closely related to SfM, but where SfM takes unordered sets of images and computes the camera locations and scene, visual odometry focuses purely on calculating the motion of the camera along an ordered set of images. Many of these methods rely on feature descriptors to find correspondences between different views, and therefore, the topic of feature extraction was presented next in the chapter. The review of feature extraction had a strong focus on Scale-Invariant Feature Transform (SIFT) which is used throughout this body of work, due to its success with the images captured and prevalence throughout the literature. Alternative methods were also presented which tended to adjust the algorithm for speed and efficiency, a problem which was solved here in part by the advances in computation & programming methods since the time SIFT was released by Lowe et al. The chapter finishes off with a review of advanced methods for RVI related to the work presented in this thesis, with solutions presented in industry and academia. Industrial systems tended to focus on larger bore pipes, where there was a choice of laser-based

metrology inspection systems available. It was also noted that an increased adoption of post-processing data from traditional RVI with SfM is ongoing, although still at an early stage and not yet widely marketed. This however, has been in practice within academia for a number of years, as shown in the review of academic inspection systems. The review of research within academia begins with an overview of two projects producing high resolution panoramic images of the interior of pipework and mineshafts. These methods were both constrained to cylindrical inspections by design, but both produced not only high-quality images, the likes of which are capable of being produced with the system presented in this thesis with a single camera, but by their virtue of having multiple cameras imaging the same region. They were able to utilise multiple view geometry to infer 3D information. The next subtopic reviewed was the use of SfM, where the projects covered varied in the constraints applied, those such as that conducted by Hansen et. al [129] successfully constrained the geometry (assuming the images were inside cylindrical pipework with known geometries) to achieve highly-accurate results. Acosta et. al [99] however pointed out the challenges of relying on photogrammetry within challenging environments, their presentation of partial reconstructions (varying by the choice of feature detector as well as their own proposed reconstruction method) highlighted the difficulties in generating a complete model of the pipework under inspection. Laser profiling methods were then reviewed, and a number of systems for capturing the geometric information of the pipework under inspection were shown. These systems offer a solution to the challenges of obtaining accurate reconstructions with SfM, as they are generally very robust in providing an accurate reading in varying environments.

Chapter 3 introduced the pipe-profiler, beginning with an overview of the operation regarding the LED and laser images, followed by the hardware used to construct the profiler itself. A simulation environment was then shown, this was used to characterise the performance of the system in terms of laser accuracy while varying several parameters. It was shown that in the current configuration 0.5 mm accuracy is possible for the size of pipe it is designed for (80 mm diameter). Alternative designs were presented to achieve this accuracy in pipes up to around 210 mm diameter. The next section of the chapter focussed on optimising the configurable parameters of the pipe profiler, such as the deployment speed, camera settings and SIFT parameters used for feature extraction. This led to an optimal inspection configuration, which achieved a stable system for extracting features and matching them accurately to stitch images and provide odometry information.

Chapter 4 focused on the calibration of the laser profiler, it begins with a review of calibration methods in the literature for systems with a similar design. A detailed overview of the triangulation method used to determine the pipe geometry is then given, followed by an analysis of the errors which arise from misalignment of the laser profiler elements. These misalignments were studied in a controlled manner within a calibration rig designed for this purpose. The method used to study misalignment was also utilised to provide a method to physically align the profiler elements, in a highly accurate manner. Furthermore, a process was developed to capture discrete values for the baseline and angle of reflection around the 360° of the laser profiler, creating a calibration for each point around the laser ring. This was an improvement of the prior method of using a global value, thus allowing for

misalignment to be tolerated. The chapter was concluded by a study of the error in a series of calibration rings as well as a pipe segment with flat bottom holes. The calibration method was shown to greatly reduce the error, even with 5.5° misalignment of the profiler elements, these results are summarised in Table 4.1.

Chapter 5 showed an implementation of the work presented in chapters three and four, by demonstrating the performance of the pipe-profiler with a case study of a split pipe. The split-pipe contained a series of defects such as axial and circumferential slots as well as flat-bottomed holes. These defects were all clearly visible in the stitched image results however, the limitations of the laser system were highlighted. Defects with a with a dimension in the axial direction of less than 0.5 mm could not be sized as the width of the laser line was greater than the opening of the defect. Following on from the case study, a real-time software implementation of the laser profiling and image stitching was presented. Lastly, a method for creating non-distorted unwrapped images from non-centralised viewpoints within the pipe was shown which would enable the system to provide high quality results in more challenging inspection scenarios.

6.2 Key Findings

The parameters used for both the camera, and feature extraction have been studied and optimised. Their impacts on performance have been characterised, thus creating a starting point for future work in varying environments with differing hardware.

The accuracy of a pipe inspection system utilising a laser-profiler and fish eye camera has been well documented and understood. To ensure the accuracies are achieved as stated, a calibration procedure has been developed and presented, allowing for a method of aligning the elements of the system, as well as correcting for misalignments in software, thus making it more practical to utilise. Accuracies of 0.5 mm in 80 mm diameter pipe are to be expected, with the software calibration applied to a dataset captured with 5.5° of misalignment. A peak sizing error of diameter was reduced from 2.50 mm to 0.27 mm and depth error of −0.96 mm to 0.21 mm for measurements taken on a 1 x 2 mm hole.

A simulation tool was developed enabling the prediction of accuracy for various configurations of laser profiler and camera combinations within any pipe diameter.

Using the knowledge from the optimisation of the parameters, and the authors significant development of the software, the system was proven to be able to operate in real-time (20 frames per second).

6.3 Future Work

Synthesised Centralisation

A significant improvement which could be made to this system is the unwrapping process, as stated throughout the current method utilised is a log-polar unwrapping from the camera centre, in the case where the camera centre and pipe centre are not in alignment, large amounts of distortion to the image will occur. In the

work [128] which the author significantly contributed to, a method is presented for using the laser-profiler for determining the pose of the probe within the pipe. This can then be used to create an unwrapped image from a centralised perspective. Implementing this within the real-time software would be a significant improvement to the current system. Furthermore, the sensitivity of the pose estimation could be improved by using a non-planer laser projector to increase the accuracy with respect to small movements and opposing translation and rotations which the current system was shown to be insensitive too.

Further improvements could also be considered for the method for obtaining the pose, as shown in Figure 5.22, the probe is relatively insensitive to small changes in translation and rotation especially when these oppose each other. A future system could project a series of dots onto the pipe wall at unique angles relative to the camera axis, it is believed this system would be more sensitive to these small and opposing changes. However, it would come at the cost of requiring a more complicated hardware design and calibration.

Large and Small-Bore Spin-Offs

Developing the system to work in larger pipes would also increase the scope of the project, as shown in Section 3.2.1 the current system would not be suitable for pipes out with its design criteria. By creating a system with a longer distance between the camera & laser projector, or by utilising multiple cameras with a narrower field of view the current level of accuracy may be maintained across a larger range of pipe diameters.

It would also be desirable to have a system which could be utilised in smaller pipes, less than 50 mm with bends such as heat exchangers. Such pipework is currently inspected with videoscopes, a system could be developed as a software only approach, it has been shown in the literature [129] that by applying constraints to the inspection, very accurate results are possible from SfM techniques. A software only approach would also benefit from being applicable to many systems and enable wider usage through the lack of requirement of specific hardware.

Point Cloud Processing and Analysis

As each point in the point cloud relates to a point in the original laser image it would be possible to colour that point with the following or prior LED image taken by the probe, this method would allow for a simplistic way to provide more information.

A further advantage of having the point cloud data for the pipework which has also not been exploited within the work presented in this thesis is that of automated methods of defect inspection.

Automated methods which could highlight regions of concern to the inspector would enable very efficient screening of large areas of pipework.

Varying Pipe Material and Geometry

Throughout this body of work the system has been only shown to work effectively on stainless steel samples and aluminium, future work could include various materials and surface finishes to determine how well the visual odometry and laser profiling perform.

In addition to this the synthesised centralisation method should be tested in more challenging geometries such as bends which are often areas with significant areas of erosion, as the current approach relies on the assumption the probe is within a perfect cylinder the amount of error such geometry would introduce is of great interest.

Conforming to IP67

Revisiting the sapphire window as shown in Section 5.2 would be beneficial as to bring the probe back to the original specification of IP67 standards [107]. This would involve facing the challenges caused by the internal reflections of both the laser and LED array on the sapphire window, which cause issues with regards to image quality. Along with these challenges, it was noted in Chapter 5 that the laser profiler with the windows in place was providing systematic mismeasurements, the calibration of Chapter 4 should therefore be applied to the final probe. This would require a mounting solution within the calibration block,

but the software only approach would mean that access to the conical mirror would not be required. This is crucial as access would not be possible, with the probe assembled and sealed to meet the IP67 standard.

Additional Sensor Payloads

In a redesigned probe, it would be advantageous to provide additional measurements to provide a more complete picture of the pipework under inspection. These could be for example, ultrasonics to provide volumetric information to supplement the surface inspection. A measure of the ambient conditions within the pipework would be beneficial as well, such as measure of background radiation to detect highly radiated sections.

Study of Time Dependent Errors

In Section 4.3 a study of the errors impacting the result of the laser profiler's accuracy. This however did not study any time dependent errors such as changes in temperature along the pipework being inspected. Such changes could cause thermal expansion to occur and impact the alignment of the optical elements. A further study could be conducted to determine the relationship between probe temperature and error, if there was a clear between the error and temperature measured within the probe this could be incorporated into the calibration allowing for corrections to be made on the fly during inspections.

Furthermore, the effects of radiation exposure upon the probe are currently unknown, controlled trials would determine any error such exposure would bring to the system along with an understanding of how the system is expected to degrade and the amount of exposure it is capable of operating within.

Commercial Adoption

Industrial demonstration has been completed successfully with positive feedback from Inspectahire™ and multinational companies. The next step is to roll the system out into commercial deployment scenarios and talks are ongoing with several companies to achieve this.

Appendices

Appendix A

Deviation Maps of Split Pipe Scan

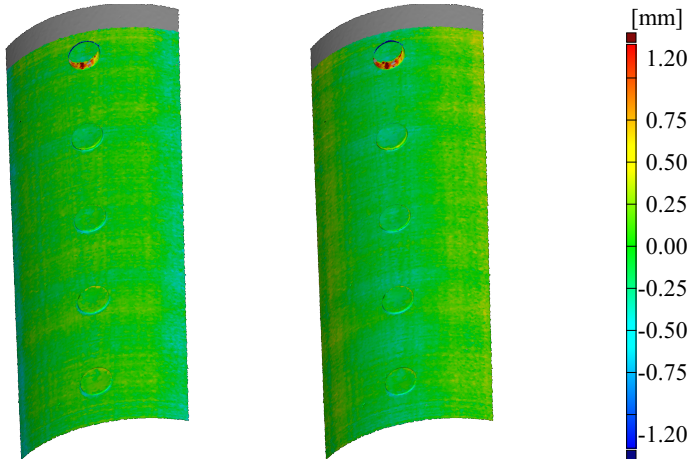

Figure A.1: *Deviation maps showing error between generated mesh and ground truth scan (a) shows the Global Angle calibration error at 0 degrees misalignment and (b) shows the Multi Angle*

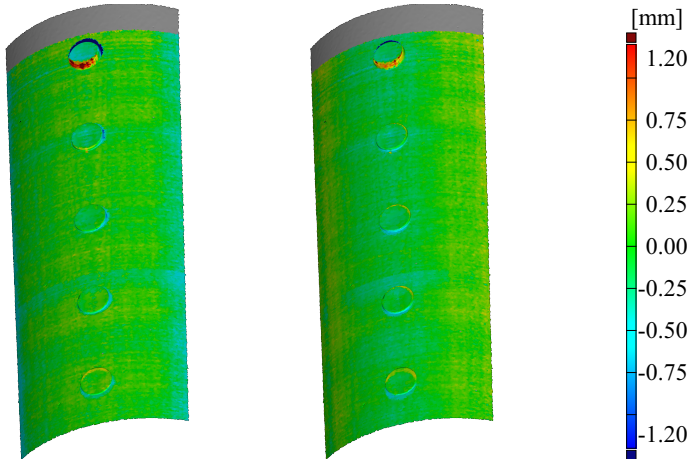

Figure A.2: *Deviation maps showing error between generated mesh and ground truth scan (a) shows the Global Angle calibration error at 1.4 degrees misalignment and (b) shows the Multi Angle*

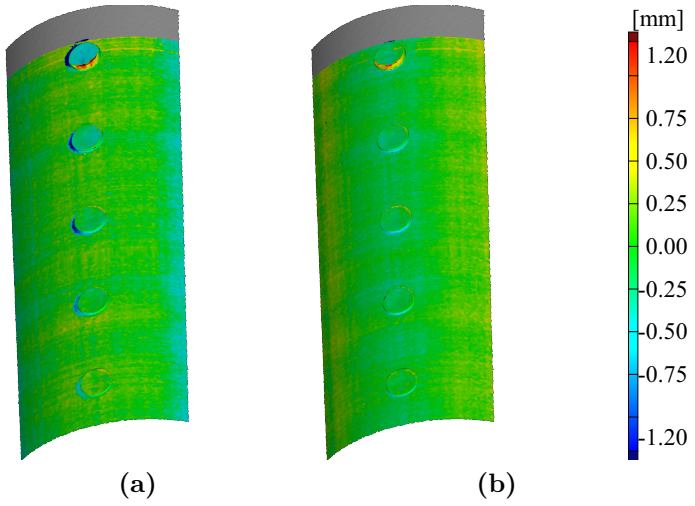

Figure A.3: *Deviation maps showing error between generated mesh and ground truth scan (a) shows the Global Angle calibration error at 2.8 degrees misalignment and (b) shows the Multi Angle*

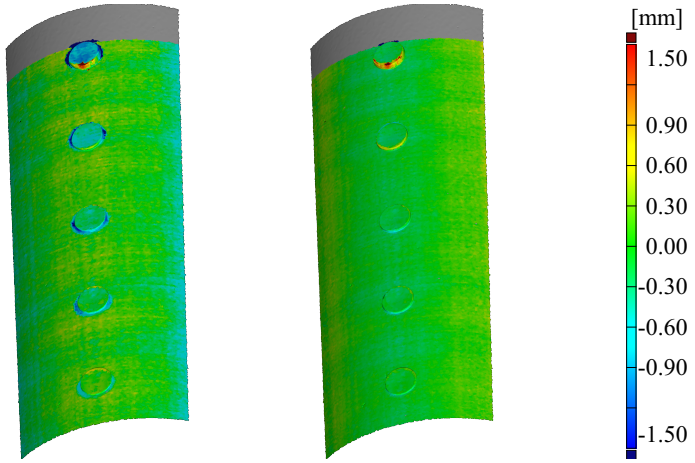

(a) (b)

Figure A.4: *Deviation maps showing error between generated mesh and ground truth scan (a) shows the Global Angle calibration error at 4.1 degrees misalignment and (b) shows the Multi Angle*

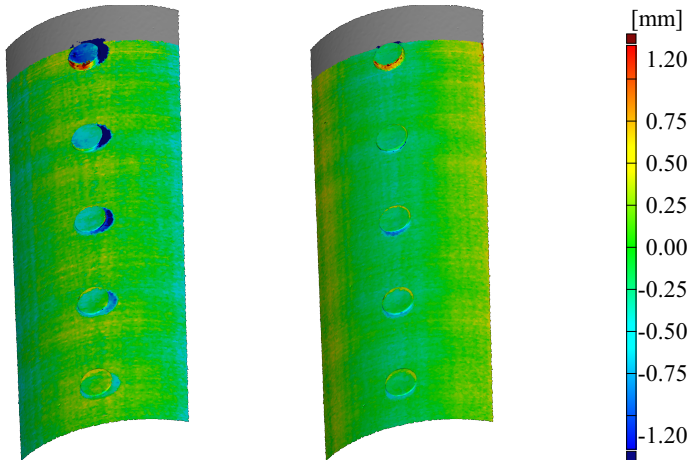

(a) (b)

Figure A.5: *Deviation maps showing error between generated mesh and ground truth scan (a) shows the Global Angle calibration error at 5.5 degrees misalignment and (b) shows the Multi Angle*

References

[1] Health and Safety Executive. (19th Feb. 2008). Use of pipeline standards and good practice guidance, [Online]. Available: https://www.hse.gov.uk/pipelines/resources/pipelinestandards.htm (accessed on 02/02/2021) (cit. on p. 1).

[2] L. J. Bond, P. Ramuhalli, M. S. Tawfik and N. J. Lybeck, 'Prognostics and life beyond 60 years for nuclear power plants', in *2011 IEEE Conference on Prognostics and Health Management*, Jun. 2011, pp. 1–7. DOI: 10.1109/ICPHM.2011.6024316 (cit. on p. 1).

[3] P. A. P. Ramírez and I. B. Utne, 'Challenges due to aging plants', *Process Safety Progress*, vol. 30, no. 2, pp. 196–199, 2011, ISSN: 1547-5913. DOI: 10.1002/prs.10453 (cit. on p. 1).

[4] K. Sieradzki and R. C. Newman, 'Stress-corrosion cracking', *Journal of Physics and Chemistry of Solids*, vol. 48, no. 11, pp. 1101–1113, 1st Jan. 1987, ISSN: 0022-3697. DOI: 10.1016/0022-3697(87)90120-X (cit. on pp. 1, 2).

[5] S. Suresh and R. O. Ritchie, 'Propagation of short fatigue cracks', *International Metals Reviews*, vol. 29, no. 1, pp. 445–475, 1st Jan. 1984, ISSN: 0308-4590. DOI: 10.1179/imtr.1984.29.1.445 (cit. on p. 1).

[6] B. N. Popov, 'Chapter 1 - Evaluation of Corrosion', in *Corrosion Engineering*, B. N. Popov, Ed., Amsterdam: Elsevier, 1st Jan. 2015, pp. 1–28, ISBN: 978-0-444-62722-3. DOI: 10.1016/B978-0-444-62722-3.00001-X (cit. on pp. 1, 2).

[7] B. N. Popov, 'Chapter 7 - Pitting and Crevice Corrosion', in *Corrosion Engineering*, B. N. Popov, Ed., Amsterdam: Elsevier, 1st Jan. 2015, pp. 289–325, ISBN: 978-0-444-62722-3. DOI: 10.1016/B978-0-444-62722-3.00007-0 (cit. on p. 2).

[8] G. T. Burstein, C. Liu, R. M. Souto and S. P. Vines, 'Origins of pitting corrosion', *Corrosion Engineering, Science and Technology*, vol. 39, no. 1, pp. 25–30, 1st Mar. 2004, ISSN: 1478-422X. DOI: 10.1179/147842204225016859 (cit. on p. 2).

[9] G01 Committee, 'Guide for Examination and Evaluation of Pitting Corrosion', ASTM International, 2018. DOI: 10.1520/G0046-94R18 (cit. on p. 2).

[10] K. L. Rens, T. J. Wipf and F. W. Klaiber, 'Review of Nondestructive Evaluation Techniques of Civil Infrastructure', *Journal of Performance of Constructed Facilities*, vol. 11, no. 4, pp. 152–160, 1st Nov. 1997, ISSN: 0887-3828. DOI: 10.1061/(ASCE)0887-3828(1997)11:4(152) (cit. on p. 10).

[11] TWI Ltd. (18th Feb. 21). What is Non-Destructive Testing (NDT)? Methods and Definition, [Online]. Available: https://www.twi-global.com/technical-knowledge/faqs/what-is-non-destructive-testing.aspx (accessed on 18/02/2021) (cit. on p. 10).

[12] Olympus. (). Small-Bore Inspection Camera - IPLEX TX — Videoscopes — Olympus, [Online]. Available: https://www.olympus-ims.com/en/rvi-products/iplex-tx/ (accessed on 08/07/2020) (cit. on p. 15).

[13] NKK Corporation. (). NKK Monthly Release: November 1997, [Online]. Available: https://www.nde-ed.org/AboutNDT/SelectedApplications/PipelineInspection/art02.html (accessed on 10/07/2020) (cit. on p. 20).

[14] R. I. Hartley and A. Zisserman, *Multiple View Geometry in Computer Vision*, 2nd ed. Cambridge University Press, ISBN: 0521540518, 2004 (cit. on pp. 24, 25, 30–32, 42, 45, 49, 50, 58).

[15] D. Scaramuzza and K. Ikeuchi, 'Omnidirectional camera', 2014 (cit. on pp. 34, 39).

[16] (). What Is Camera Calibration? - MATLAB & Simulink, [Online]. Available: https://www.mathworks.com/help/vision/ug/camera-calibration.html (accessed on 07/09/2020) (cit. on p. 34).

[17] D. Scaramuzza, A. Martinelli and R. Siegwart, 'A Flexible Technique for Accurate Omnidirectional Camera Calibration and Structure from Motion', in *Fourth IEEE International Conference on Computer Vision Systems (ICVS'06)*, Jan. 2006, pp. 45–45. DOI: 10.1109/ICVS.2006.3 (cit. on pp. 35, 36, 109, 110).

[18] D. Scaramuzza, A. Martinelli and R. Siegwart, 'A Toolbox for Easily Calibrating Omnidirectional Cameras', in *2006 IEEE/RSJ International Conference on Intelligent Robots and Systems*, Oct. 2006, pp. 5695–5701. DOI: 10.1109/IROS.2006.282372 (cit. on pp. 35, 39, 41, 110, 204–206).

[19] (). OCamCalib: Omnidirectional Camera Calibration Toolbox for Matlab - Davide Scaramuzza, [Online]. Available: https://sites.google.com/site/scarabotix/ocamcalib-toolbox (accessed on 05/09/2020) (cit. on pp. 36, 37, 39).

[20] X. Ying and Z. Hu, 'Can We Consider Central Catadioptric Cameras and Fisheye Cameras within a Unified Imaging Model', in *Computer Vision - ECCV 2004*, T. Pajdla and J. Matas, Eds., ser. Lecture Notes in Computer Science, Berlin, Heidelberg: Springer, 2004, pp. 442–455, ISBN: 978-3-540-24670-1. DOI: 10.1007/978-3-540-24670-1_34 (cit. on p. 39).

[21] J. Barreto and H. Araujo, 'Issues on the geometry of central catadioptric image formation', in *Proceedings of the 2001 IEEE Computer Society Conference on Computer Vision and Pattern Recognition. CVPR 2001*, vol. 2, Dec. 2001, pp. II–II. DOI: 10.1109/CVPR.2001.990992 (cit. on p. 39).

[22] C. Geyer and K. Daniilidis, 'A Unifying Theory for Central Panoramic Systems and Practical Implications', in *Computer Vision — ECCV 2000*, D. Vernon, Ed., ser. Lecture Notes in Computer Science, Berlin, Heidelberg: Springer, 2000, pp. 445–461, ISBN: 978-3-540-45053-5. DOI: 10.1007/3-540-45053-X_29 (cit. on p. 39).

[23] S. Baker and S. K. Nayar, 'A Theory of Single-Viewpoint Catadioptric Image Formation', *International Journal of Computer Vision*, vol. 35, no. 2, pp. 175–196, 1st Nov. 1999, ISSN: 1573-1405. DOI: 10.1023/A:1008128724364 (cit. on p. 39).

[24] S. Urban, J. Leitloff and S. Hinz, 'Improved wide-angle, fisheye and omnidirectional camera calibration', *ISPRS Journal of Photogrammetry and Remote Sensing*, vol. 108, pp. 72–79, 1st Oct. 2015, ISSN: 0924-2716. DOI: 10.1016/j.isprsjprs.2015.06.005 (cit. on p. 41).

[25] (). Single Camera Calibrator App - MATLAB & Simulink, [Online]. Available: https://www.mathworks.com/help/vision/ug/single-camera-calibrator-app.html (accessed on 09/09/2020) (cit. on p. 41).

[26] J. Heikkila and O. Silven, 'A four-step camera calibration procedure with implicit image correction', in *Proceedings of IEEE Computer Society Conference on Computer Vision and Pattern Recognition*, Jun. 1997, pp. 1106–1112. DOI: 10.1109/CVPR.1997.609468 (cit. on p. 41).

[27] Z. Zhang, 'A flexible new technique for camera calibration', *IEEE Transactions on Pattern Analysis and Machine Intelligence*, vol. 22, no. 11, pp. 1330–1334, Nov. 2000, ISSN: 1939-3539. DOI: 10.1109/34.888718 (cit. on p. 41).

[28] L. Puig, J. Bermúdez, P. Sturm and J. J. Guerrero, 'Calibration of omnidirectional cameras in practice: A comparison of methods', *Computer Vision and Image Understanding*, Virtual Representations and Modeling of Large-Scale Environments (VRML), vol. 116, no. 1, pp. 120–137, 1st Jan. 2012, ISSN: 1077-3142. DOI: 10.1016/j.cviu.2011.08.003 (cit. on p. 41).

[29] D. Scaramuzza, 'Tutorial on Visual Odometry', 18th Nov. 2013 (cit. on p. 45).

[30] (). Estimate fundamental matrix from corresponding points in stereo images - MATLAB estimateFundamentalMatrix, [Online]. Available: https://www.mathworks.com/help/vision/ref/estimatefundamentalmatrix.html (accessed on 17/11/2020) (cit. on p. 45).

[31] C. Loop and Zhengyou Zhang, 'Computing rectifying homographies for stereo vision', in *Proceedings. 1999 IEEE Computer Society Conference on Computer Vision and Pattern Recognition (Cat. No PR00149)*, vol. 1, Jun. 1999, 125–131 Vol. 1. DOI: 10.1109/CVPR.1999.786928 (cit. on p. 46).

[32] F.-F. Li, 'Stereo Vision', (Stanford Vision Lab), 21st Oct. 14 (cit. on p. 48).

[33] H. C. Longuet-Higgins, 'A computer algorithm for reconstructing a scene from two projections', *Nature*, vol. 293, no. 5828, pp. 133–135, 5828 Sep. 1981, ISSN: 1476-4687. DOI: 10.1038/293133a0 (cit. on p. 49).

[34] (20th Nov. 2020). Cnr-isti-vclab/meshlab, [Online]. Available: https://github.com/cnr-isti-vclab/meshlab (accessed on 21/11/2020) (cit. on p. 51).

[35] (). Agisoft Metashape, [Online]. Available: https://www.agisoft.com/ (accessed on 20/03/2020) (cit. on pp. 51, 59).

[36] R. I. Hartley and A. Zisserman, *Multiple View Geometry in Computer Vision*, 2nd ed. pp. 310-330: Cambridge University Press, ISBN: 0521540518, 2004 (cit. on pp. 51, 52).

[37] R. I. Hartley, 'Self-calibration from multiple views with a rotating camera', in *Computer Vision — ECCV '94*, J.-O. Eklundh, Ed., ser. Lecture Notes in Computer Science, Berlin, Heidelberg: Springer, 1994, pp. 471–478, ISBN: 978-3-540-48398-4. DOI: 10.1007/3-540-57956-7_52 (cit. on p. 52).

[38] M. Levoy, S. Rusinkiewicz, M. Ginzton, J. Ginsberg, K. Pulli, D. Koller, S. Anderson, J. Shade, B. Curless, L. Pereira, J. Davis and D. Fulk, 'The Digital Michelangelo Project: 3D Scanning of Large Statues', p. 14, 2000 (cit. on p. 54).

[39] L. Zhang, B. Cudess and S. M. Seitz, 'Rapid Shape Acquisition Using Color Structured Lightand Multi-pass Dynamic Programming', in *In The 1st IEEE International Symposium on 3D Data Processing, Visualization, and Transmission*, 2002, pp. 24–36 (cit. on pp. 54, 55).

[40] R. Knies. (2nd Oct. 2013). Collaboration, expertise produce enhanced sensing in Xbox One, [Online]. Available: https://docs.microsoft.com/en-us/archive/blogs/microsoft_blog/collaboration-expertise-produce-enhanced-sensing-in-xbox-one (accessed on 30/11/2020) (cit. on p. 55).

[41] T. Butkiewicz, 'Low-cost coastal mapping using Kinect v2 time-of-flight cameras', in *2014 Oceans - St. John's*, Sep. 2014, pp. 1–9. DOI: 10.1109/OCEANS.2014.7003084 (cit. on p. 55).

[42] L. Yang, L. Zhang, H. Dong, A. Alelaiwi and A. E. Saddik, 'Evaluating and Improving the Depth Accuracy of Kinect for Windows v2', *IEEE Sensors Journal*, vol. 15, no. 8, pp. 4275–4285, Aug. 2015, ISSN: 1558-1748. DOI: 10.1109/JSEN.2015.2416651 (cit. on p. 55).

[43] O. Wasenmüller, M. Meyer and D. Stricker, 'CoRBS: Comprehensive RGB-D benchmark for SLAM using Kinect v2', in *2016 IEEE Winter Conference on Applications of Computer Vision (WACV)*, Mar. 2016, pp. 1–7. DOI: 10.1109/WACV.2016.7477636 (cit. on p. 55).

[44] E. Lachat, H. Macher, T. Landes and P. Grussenmeyer, 'Assessment and Calibration of a RGB-D Camera (Kinect v2 Sensor) Towards a Potential Use for Close-Range 3D Modeling', *Remote Sensing*, vol. 7, no. 10, pp. 13 070–13 097, 10 Oct. 2015. DOI: 10.3390/rs71013070 (cit. on p. 55).

[45] P. Grussenmeyer, 'FIRST EXPERIENCES WITH KINECT V2 SENSOR FOR CLOSE RANGE 3D MODELLING', (cit. on p. 55).

[46] A. Corti, S. Giancola, G. Mainetti and R. Sala, 'A metrological characterization of the Kinect V2 time-of-flight camera', *Robotics and Autonomous Systems*, vol. 75, pp. 584–594, 1st Jan. 2016, ISSN: 0921-8890. DOI: 10.1016/j.robot.2015.09.024 (cit. on p. 55).

[47] P. Fankhauser, M. Bloesch, D. Rodriguez, R. Kaestner, M. Hutter and R. Siegwart, 'Kinect v2 for mobile robot navigation: Evaluation and modeling', in *2015 International Conference on Advanced Robotics (ICAR)*, Jul. 2015, pp. 388–394. DOI: 10.1109/ICAR.2015.7251485 (cit. on p. 55).

[48] M. Kowalski, J. Naruniec and M. Daniluk, 'Livescan3D: A Fast and Inexpensive 3D Data Acquisition System for Multiple Kinect v2 Sensors', in *2015 International Conference on 3D Vision*, Oct. 2015, pp. 318–325. DOI: 10.1109/3DV.2015.43 (cit. on p. 55).

[49] W. G. Aguilar and S. G. Morales, '3D Environment Mapping Using the Kinect V2 and Path Planning Based on RRT Algorithms', *Electronics*, vol. 5, no. 4, p. 70, 4 Dec. 2016. DOI: 10.3390/electronics5040070 (cit. on p. 55).

[50] C. S. Bamji, S. Mehta, B. Thompson, T. Elkhatib, S. Wurster, O. Akkaya, A. Payne, J. Godbaz, M. Fenton, V. Rajasekaran, L. Prather, S. Nagaraja, V. Mogallapu, D. Snow, R. McCauley, M. Mukadam, I. Agi, S. McCarthy, Z. Xu, T. Perry, W. Qian, V. Chan, P. Adepu, G. Ali, M. Ahmed, A. Mukherjee, S. Nayak, D. Gampell, S. Acharya, L. Kordus and P. O'Connor, 'IMpixel 65nm BSI 320MHz demodulated TOF Image sensor with 3 micrometres global shutter pixels and analog binning', in *2018 IEEE International Solid - State Circuits Conference - (ISSCC)*, Feb. 2018, pp. 94–96. DOI: 10.1109/ISSCC.2018.8310200 (cit. on p. 56).

[51] S. Ullman and S. Brenner, 'The interpretation of structure from motion', *Proceedings of the Royal Society of London. Series B. Biological Sciences*, vol. 203, no. 1153, pp. 405–426, 15th Jan. 1979. DOI: 10.1098/rspb.1979.0006 (cit. on p. 56).

[52] S. Agarwal, N. Snavely, I. Simon, S. M. Seitz and R. Szeliski, 'Building Rome in a Day', presented at the International Conference on Computer Vision, Kyoto, Japan, 2009 (cit. on p. 56).

[53] J. Heinly, J. L. Schonberger, E. Dunn and J.-M. Frahm, 'Reconstructing the world* in six days', in *2015 IEEE Conference on Computer Vision and Pattern Recognition (CVPR)*, Boston, MA, USA: IEEE, Jun. 2015, pp. 3287–3295, ISBN: 978-1-4673-6964-0. DOI: 10.1109/CVPR.2015.7298949 (cit. on pp. 56, 58).

[54] S. Agarwal, Y. Furukawa, I. Simon, R. Szeliski, S. M. Seitz, B. Curless and N. Snavely. (Oct. 2011). Building Rome in a Day, [Online]. Available: https://cacm.acm.org/magazines/2011/10/131417-building-rome-in-a-day/fulltext (accessed on 01/12/2020) (cit. on p. 57).

[55] J. L. Schonberger and J.-M. Frahm, 'Structure-from-Motion Revisited', in *2016 IEEE Conference on Computer Vision and Pattern Recognition (CVPR)*, Las Vegas, NV, USA: IEEE, Jun. 2016, pp. 4104–4113, ISBN: 978-1-4673-8851-1. DOI: 10.1109/CVPR.2016.445 (cit. on p. 57).

[56] N. Snavely, S. M. Seitz and R. Szeliski, 'Skeletal graphs for efficient structure from motion', in *2008 IEEE Conference on Computer Vision and Pattern Recognition*, Jun. 2008, pp. 1–8. DOI: 10.1109/CVPR.2008.4587678 (cit. on p. 58).

[57] Y. Lou, N. Snavely and J. Gehrke, 'MatchMiner: Efficient Spanning Structure Mining in Large Image Collections', in *Computer Vision – ECCV 2012*, A. Fitzgibbon, S. Lazebnik, P. Perona, Y. Sato and C. Schmid, Eds., ser. Lecture Notes in Computer Science, Berlin, Heidelberg: Springer, 2012, pp. 45–58, ISBN: 978-3-642-33709-3. DOI: 10.1007/978-3-642-33709-3_4 (cit. on p. 58).

[58] J. L. Schönberger, A. C. Berg and J.-M. Frahm, 'Efficient Two-View Geometry Classification', in *Pattern Recognition*, J. Gall, P. Gehler and B. Leibe, Eds., ser. Lecture Notes in Computer Science, Cham: Springer International Publishing, 2015, pp. 53–64, ISBN: 978-3-319-24947-6. DOI: 10.1007/978-3-319-24947-6_5 (cit. on pp. 58, 59).

[59] B. Triggs, P. F. McLauchlan, R. I. Hartley and A. W. Fitzgibbon, 'Bundle Adjustment — A Modern Synthesis', in *Vision Algorithms: Theory and Practice*, ser. Lecture Notes in Computer Science, B. Triggs, A. Zisserman and R. Szeliski, Eds., red. by G. Goos, J. Hartmanis and J. van Leeuwen, vol. 1883, Berlin, Heidelberg: Springer Berlin Heidelberg, 2000, pp. 298–372, ISBN: 978-3-540-67973-8 978-3-540-44480-0. DOI: 10.1007/3-540-44480-7_21 (cit. on p. 59).

[60] N. Snavely. (2008). Bundler - Structure from Motion (SfM) for Unordered Image Collections, [Online]. Available: https://www.cs.cornell.edu/~snavely/bundler/ (accessed on 04/12/2020) (cit. on p. 59).

[61] C. Wu, 'Towards Linear-Time Incremental Structure from Motion', in *2013 International Conference on 3D Vision - 3DV 2013*, Jun. 2013, pp. 127–134. DOI: 10.1109/3DV.2013.25 (cit. on p. 59).

[62] C. Wu. (2006–2012). VisualSFM : A Visual Structure from Motion System, [Online]. Available: http://ccwu.me/vsfm/ (accessed on 04/12/2020) (cit. on p. 59).

[63] C. Wu, S. Agarwal, B. Curless and S. M. Seitz, 'Multicore bundle adjustment', in *CVPR 2011*, Jun. 2011, pp. 3057–3064. DOI: 10.1109/CVPR.2011.5995552 (cit. on p. 59).

[64] D. Zhang, 'Autonomous Unmanned Aerial Vehicle for Non-Destructive Testing', p. 230, May 2019 (cit. on pp. 59, 92).

[65] Pix4D SA. (2020). Pix4D, Pix4D, [Online]. Available: https://www.pix4d.com/ (accessed on 04/12/2020) (cit. on p. 59).

[66] Autodesk. (2020). ReCap Pro — Reality Capture & 3D Scanning Software — Autodesk, [Online]. Available: https://www.autodesk.co.uk/products/recap/overview?plc=RECAP&term=1-YEAR&support=ADVANCED&quantity=1 (accessed on 04/12/2020) (cit. on p. 59).

[67] Capturing Reality s.r.o. (2020). RealityCapture: Mapping and 3D Modeling Photogrammetry Software - CapturingReality.com, [Online]. Available: https://www.capturingreality.com/ (accessed on 04/12/2020) (cit. on p. 59).

[68] M. S. Nixon and A. S. Aguado, '4 - Low-level feature extraction (including edge detection)', in *Feature Extraction and Image Processing for Computer Vision (Fourth Edition)*, M. S. Nixon and A. S. Aguado, Eds., Academic Press, 1st Jan. 2020, pp. 141–222, ISBN: 978-0-12-814976-8. DOI: 10.1016/B978-0-12-814976-8.00004-X (cit. on p. 61).

[69] J. Canny, 'A Computational Approach to Edge Detection', *IEEE Transactions on Pattern Analysis and Machine Intelligence*, vol. PAMI-8, no. 6, pp. 679–698, Nov. 1986, ISSN: 0162-8828. DOI: 10.1109/TPAMI.1986.4767851 (cit. on pp. 61, 62).

[70] L. J. van Vliet, I. T. Young and G. L. Beckers, 'A nonlinear laplace operator as edge detector in noisy images', *Computer Vision, Graphics, and Image Processing*, vol. 45, no. 2, pp. 167–195, 1st Feb. 1989, ISSN: 0734-189X. DOI: 10.1016/0734-189X(89)90131-X (cit. on p. 61).

[71] C. Harris and M. Stephens, 'A combined corner and edge detector', in *In Proc. Fourth Alvey Vision Conference*, 1988, pp. 147–152 (cit. on pp. 62, 66).

[72] D. G. Lowe, 'Distinctive Image Features from Scale-Invariant Keypoints', *International Journal of Computer Vision*, vol. 60, no. 2, pp. 91–110, Nov. 2004, ISSN: 0920-5691. DOI: 10.1023/B:VISI.0000029664.99615.94 (cit. on pp. 63–65, 70, 125, 134, 139).

[73] D. G. Lowe, 'Object recognition from local scale-invariant features', in *Proceedings of the Seventh IEEE International Conference on Computer Vision*, vol. 2, Sep. 1999, 1150–1157 vol.2. DOI: 10.1109/ICCV.1999.790410 (cit. on p. 63).

[74] T. Lindeberg, 'Scale-space theory: A basic tool for analyzing structures at different scales', *Journal of Applied Statistics*, vol. 21, no. 1-2, pp. 225–270, 1st Jan. 1994, ISSN: 0266-4763. DOI: 10.1080/757582976 (cit. on p. 63).

[75] M. Brown and D. Lowe, 'Invariant Features from Interest Point Groups', in *Procedings of the British Machine Vision Conference 2002*, Cardiff: British Machine Vision Association, 2002, pp. 23.1–23.10, ISBN: 978-1-901725-19-3. DOI: 10.5244/C.16.23 (cit. on p. 65).

[76] J. S. Beis and D. G. Lowe, 'Shape indexing using approximate nearest-neighbour search in high-dimensional spaces', in *Proceedings of IEEE Computer Society Conference on Computer Vision and Pattern Recognition*, Jun. 1997, pp. 1000–1006. DOI: 10.1109/CVPR.1997.609451 (cit. on p. 70).

[77] H. Bay, A. Ess, T. Tuytelaars and L. Van Gool, 'Speeded-Up Robust Features (SURF)', *Computer Vision and Image Understanding*, Similarity Matching in Computer Vision and Multimedia, vol. 110, no. 3, pp. 346–359, 1st Jun. 2008, ISSN: 1077-3142. DOI: 10.1016/j.cviu.2007.09.014 (cit. on pp. 71–75).

[78] H. Bay, T. Tuytelaars and L. Van Gool, 'SURF: Speeded Up Robust Features', in *Computer Vision – ECCV 2006*, A. Leonardis, H. Bischof and A. Pinz, Eds., ser. Lecture Notes in Computer Science, Berlin, Heidelberg: Springer, 2006, pp. 404–417, ISBN: 978-3-540-33833-8. DOI: 10.1007/11744023_32 (cit. on p. 71).

[79] A. Neubeck and L. V. Gool, 'Efficient Non-Maximum Suppression', in *18th International Conference on Pattern Recognition (ICPR'06)*, vol. 3, Aug. 2006, pp. 850–855. DOI: 10.1109/ICPR.2006.479 (cit. on p. 73).

[80] E. Rosten, R. Porter and T. Drummond, 'Faster and Better: A Machine Learning Approach to Corner Detection', *IEEE Transactions on Pattern Analysis and Machine Intelligence*, vol. 32, no. 1, pp. 105–119, Jan. 2010, ISSN: 1939-3539. DOI: 10.1109/TPAMI.2008.275 (cit. on p. 76).

[81] M. Calonder, V. Lepetit, C. Strecha and P. Fua, 'BRIEF: Binary Robust Independent Elementary Features', in *Computer Vision – ECCV 2010*, K. Daniilidis, P. Maragos and N. Paragios, Eds., ser. Lecture Notes in Computer Science, Berlin, Heidelberg: Springer, 2010, pp. 778–792, ISBN: 978-3-642-15561-1. DOI: 10.1007/978-3-642-15561-1_56 (cit. on p. 76).

[82] P. L. Rosin, 'Measuring Corner Properties', *Computer Vision and Image Understanding*, vol. 73, no. 2, pp. 291–307, Feb. 1999, ISSN: 10773142. DOI: 10.1006/cviu.1998.0719 (cit. on p. 77).

[83] E. Rublee, V. Rabaud, K. Konolige and G. Bradski, 'ORB: An efficient alternative to SIFT or SURF', in *2011 International Conference on Computer Vision*, Nov. 2011, pp. 2564–2571. DOI: 10.1109/ICCV.2011.6126544 (cit. on p. 77).

[84] K. Mikolajczyk and C. Schmid, 'A performance evaluation of local descriptors', *IEEE Transactions on Pattern Analysis and Machine Intelligence*, vol. 27, no. 10, pp. 1615–1630, Oct. 2005, ISSN: 1939-3539. DOI: 10.1109/TPAMI.2005.188 (cit. on p. 78).

[85] T. Tuytelaars and K. Mikolajczyk, 'Local Invariant Feature Detectors: A Survey', *Foundations and Trends in Computer Graphics and Vision*, vol. 3, no. 3, pp. 177–280, 2007, ISSN: 1572-2740, 1572-2759. DOI: 10.1561/0600000017 (cit. on p. 78).

[86] F. Bellavia and C. Colombo, 'Is There Anything New to Say About SIFT Matching?', *International Journal of Computer Vision*, vol. 128, no. 7, pp. 1847–1866, 1st Jul. 2020, ISSN: 1573-1405. DOI: 10.1007/s11263-020-01297-z (cit. on p. 78).

[87] (2019). RedZone® Robotics in Pittsburgh, PA — Wastewater & Sewer Asset Management, [Online]. Available: https://www.redzone.com/ (accessed on 17/09/2019) (cit. on pp. 80, 116).

[88] M. Johnson and G. S. Gupta, 'A robotic laser pipeline profiler', in *Proceedings of the 20th IEEE Instrumentation Technology Conference (Cat. No.03CH37412)*, vol. 2, May 2003, 1488–1491 vol.2. DOI: 10.1109/IMTC.2003.1207997 (cit. on pp. 82, 83).

[89] (2019). PureRobotics - Pipeline Inspection System, Pure Technologies, [Online]. Available: https://puretechltd.com/technology/purerobotics-pipeline-inspection-system/ (accessed on 17/09/2019) (cit. on p. 84).

[90] Inspector Systems. (1st Jan. 2020). Video/Laser robots, [Online]. Available: https://inspector-systems.com/pipe-crawler/robots-for-video-and-laser-inspection.html (accessed on 01/01/2021) (cit. on p. 85).

[91] G. West, P. Murray, S. Marshall and S. McArthur, 'Improved visual inspection of advanced gas-cooled reactor fuel channels', *International Journal of Prognostics and Health Management*, vol. 6, no. Specia, Specia 13th Jul. 2015, ISSN: 2153-2648 (cit. on pp. 86, 87, 98).

[92] J. König and P. O'Leary, 'Hyper resolution image mosaics with unbounded vertical field of view', *Computers in Industry*, vol. 122, p. 103 281, Nov. 2020, ISSN: 01663615. DOI: 10.1016/j.compind.2020.103281 (cit. on pp. 87, 98).

[93] B. Wijerathna, T. Vidal-Calleja, S. Kodagoda, Q. Zhang and J. V. Miro, 'Multiple defect interpretation based on Gaussian processes for MFL technology', in *Nondestructive Characterization for Composite Materials, Aerospace Engineering, Civil Infrastructure, and Homeland Security 2013*, vol. 8694, International Society for Optics and Photonics, 11th Apr. 2013, 86941Z. DOI: 10.1117/12.2009966 (cit. on p. 88).

[94] T. Vidal-Calleja, J. V. Miró, F. Martín, D. C. Lingnau and D. E. Russell, 'Automatic detection and verification of pipeline construction features with multi-modal data', in *2014 IEEE/RSJ International Conference on Intelligent Robots and Systems*, Sep. 2014, pp. 3116–3122. DOI: 10.1109/IROS.2014.6942993 (cit. on p. 88).

[95] N. Ulapane, A. Alempijevic, T. Vidal-Calleja, J. V. Miro, J. Rudd and M. Roubal, 'Gaussian process for interpreting pulsed eddy current signals for ferromagnetic pipe profiling', in *2014 9th IEEE Conference on Industrial Electronics and Applications*, Jun. 2014, pp. 1762–1767. DOI: 10.1109/ICIEA.2014.6931453 (cit. on p. 88).

[96] R. Falque, T. Vidal-Calleja, J. V. Miro, D. C. Lingnau and D. E. Russell, 'Background Segmentation to Enhance Remote Field Eddy Current Signals', p. 9, (cit. on p. 88).

[97] T. Vidal-Calleja, J. V. Miró, F. Martín, D. C. Lingnau and D. E. Russell, 'Automatic detection and verification of pipeline construction features with multi-modal data', in *2014 IEEE/RSJ International Conference on Intelligent Robots and Systems*, Sep. 2014, pp. 3116–3122. DOI: 10.1109/IROS.2014.6942993 (cit. on p. 88).

[98] P. Hansen, H. Alismail, P. Rander and B. Browning, 'Visual mapping for natural gas pipe inspection', *The International Journal of Robotics Research*, vol. 34, no. 4-5, pp. 532–558, 1st Apr. 2015, ISSN: 0278-3649. DOI: 10.1177/0278364914550133 (cit. on pp. 89–91, 98).

[99] A. V. Reyes-Acosta, I. Lopez-Juarez, R. Osorio-Comparan and G. Lefranc, '3D pipe reconstruction employing video information from mobile robots', *Applied Soft Computing*, vol. 75, pp. 562–574, 1st Feb. 2019, ISSN: 1568-4946. DOI: 10.1016/j.asoc.2018.11.016 (cit. on pp. 91–93, 98, 215).

[100] K. Matsui, A. Yamashita and T. Kaneko, '3-D shape measurement of pipe by range finder constructed with omni-directional laser and omni-directional camera', in *2010 IEEE International Conference on Robotics and Automation*, May 2010, pp. 2537–2542. DOI: 10.1109/ROBOT.2010.5509851 (cit. on p. 93).

[101] A. D. Tezerjani, M. Mehrandezh and R. Paranjape, 'Pose Estimation of a Dioptric Imaging Sensor with a Circle-Projecting Collimated Laser Moving Inside a Pipeline', in *Nonlinear Approaches in Engineering Applications*, L. Dai and R. N. Jazar, Eds., Cham: Springer International Publishing, 2015, pp. 281–298, ISBN: 978-3-319-09461-8 978-3-319-09462-5. DOI: 10.1007/978-3-319-09462-5_11 (cit. on p. 94).

[102] P. Buschinelli, T. Pinto, F. Silva, J. Santos and A. Albertazzi, 'Laser Triangulation Profilometer for Inner Surface Inspection of 100 millimeters (4") Nominal Diameter', *Journal of Physics: Conference Series*, vol. 648, no. 1, p. 012 010, 2015, ISSN: 1742-6596. DOI: 10.1088/1742-6596/648/1/012010 (cit. on pp. 94, 95, 146–148).

[103] N. Stanić, M. Lepot, M. Catieau, J. Langeveld and F. H. L. R. Clemens, 'A technology for sewer pipe inspection (part 1): Design, calibration, corrections and potential application of a laser profiler', *Automation in Construction*, vol. 75, pp. 91–107, 1st Mar. 2017, ISSN: 0926-5805. DOI: 10.1016/j.autcon.2016.12.005 (cit. on p. 95).

[104] M. Lepot, N. Stanić and F. H. L. R. Clemens, 'A technology for sewer pipe inspection (Part 2): Experimental assessment of a new laser profiler for sewer defect detection and quantification', *Automation in Construction*, vol. 73, pp. 1–11, 1st Jan. 2017, ISSN: 0926-5805. DOI: 10.1016/j.autcon.2016.10.010 (cit. on pp. 95, 96).

[105] L. Jin, N. Miyatsu, E. Kondoh, B. Gelloz, N. Kanazawa and T. Yoshizawa, 'Measurement of diameter of cylindrical openings using a disk beam probe', *Optical Review*, vol. 25, no. 6, pp. 656–662, 1st Dec. 2018, ISSN: 1349-9432. DOI: 10.1007/s10043-018-0459-7 (cit. on p. 96).

[106] R. He, C. Liu, Z. Zhang and J. Sun, 'Measurement model of the omnidirectional structured-light vision and its calibration method', *OSA Continuum*, vol. 2, no. 3, pp. 839–847, 15th Mar. 2019, ISSN: 2578-7519. DOI: 10.1364/OSAC.2.000839 (cit. on pp. 97, 146–148).

[107] Commission électrotechnique internationale, Commission électrotechnique internationale and Comité d'études 70 de la CEI : Degrés de protection procurés par les enveloppes, *Degrees of Protection Provided by Enclosures (IP Code)*. 2013, ISBN: 978-2-8322-1086-4 (cit. on pp. 105, 185, 221).

[108] (). Mosaicing for Automatic Pipe Scanning (MAPS) (CR&D) — University of Strathclyde, [Online]. Available: https://pureportal.strath.ac.uk/en/projects/mosaicing-for-automatic-pipe-scanning-maps-crd (accessed on 24/05/2019) (cit. on p. 105).

[109] R. Summan, G. Dobie, G. West, S. Marshall, C. MacLeod and S. G. Pierce, 'The Influence of the Spatial Distribution of 2-D Features on Pose Estimation for a Visual Pipe Mapping Sensor', *IEEE Sensors Journal*, vol. 17, no. 19, pp. 6312–6321, Oct. 2017, ISSN: 1530-437X. DOI: 10.1109/JSEN.2017.2723728 (cit. on pp. 105, 175).

[110] R. Summan, N. Mathur, G. Dobie, G. West, S. Marshall, C. Mineo, C. N. MacLeod, S. Pierce and W. Kerr, 'Mosaicing for automated pipe scanning', 24th Nov. 2016 (cit. on p. 105).

[111] R. Summan, W. Jackson, G. Dobie, C. N. MacLeod, C. Mineo, G. West, D. Offin, G. Bolton, S. Marshall and A. Lille, 'A novel visual pipework inspection system', 16th Jul. 2017 (cit. on p. 105).

[112] N. Mathur, R. Summan, G. Dobie, G. West and S. Marshall, 'Error model of misalignment error in a radial 3D scanner', in *2017 IEEE SENSORS*, Oct. 2017, pp. 1–3. DOI: 10.1109/ICSENS.2017.8234217 (cit. on p. 105).

[113] (). Blackfly GigE — FLIR Systems, [Online]. Available: https://www.flir.com/products/blackfly-gige/ (accessed on 26/03/2020) (cit. on pp. 107, 126).

[114] S. P. Dsl, 'DSL216 Specification Sheet', p. 3, (cit. on p. 107).

[115] Texas Instruments. (18th May 21). MSP430G2553 data sheet, product information and support — TI.com, [Online]. Available: https://www.ti.com/product/MSP430G2553 (accessed on 18/05/2021) (cit. on p. 108).

[116] MATLAB. (). Computer Vision Toolbox Documentation - MathWorks United Kingdom, [Online]. Available: https://uk.mathworks.com/help/vision/index.html?s_tid=CRUX_lftnav (accessed on 12/02/2020) (cit. on pp. 109, 115).

[117] (). OpenCV, [Online]. Available: https://opencv.org/ (accessed on 26/03/2020) (cit. on p. 126).

[118] Y. Zhu, Y. Gu, Y. Jin and C. Zhai, 'Flexible calibration method for an inner surface detector based on circle structured light', *Applied Optics*, vol. 55, no. 5, p. 1034, 10th Feb. 2016, ISSN: 0003-6935, 1539-4522. DOI: 10.1364/AO.55.001034 (cit. on p. 146).

[119] S. Urban, J. Leitloff and S. Hinz, 'MLPNP - A REAL-TIME MAXIMUM LIKELIHOOD SOLUTION TO THE PERSPECTIVE-N-POINT PROBLEM', *ISPRS Annals of Photogrammetry, Remote Sensing and Spatial Information Sciences*, vol. III-3, pp. 131–138, 3rd Jun. 2016, ISSN: 2194-9050. DOI: 10.5194/isprsannals-III-3-131-2016 (cit. on p. 154).

[120] T. Rabbani. (25th Oct. 5). PROTO toolbox, [Online]. Available: http://viztronics.com/tahir/data/PROTO/doc/menu.html (accessed on 26/03/2019) (cit. on p. 155).

[121] S. Jianbo and C. Tomasi, 'Good features to track', in *IEEE Computer Society Conference on Computer Vision and Pattern Recognition*, 1994, pp. 593–600 (cit. on p. 158).

[122] T. J. Atherton and D. J. Kerbyson, 'Size invariant circle detection', *Image and Vision Computing*, vol. 17, no. 11, pp. 795–803, 1st Sep. 1999, ISSN: 0262-8856. DOI: 10.1016/S0262-8856(98)00160-7 (cit. on p. 166).

[123] (). ATOS Triple Scan — GOM, [Online]. Available: https://www.gom.com/metrology-systems/atos/atos-triple-scan.html (accessed on 22/11/2019) (cit. on p. 175).

[124] A. Vedaldi and B. Fulkerson, 'VLFeat: An open and portable library of computer vision algorithms', 2008 (cit. on p. 175).

[125] C. Mineo, J. Riise, R. Summan, C. N. MacLeod and S. G. Pierce. (Apr. 2018). Index-based triangulation method for efficient generation of large three-dimensional ultrasonic C-scans, [Online]. Available: https://www.ingentaconnect.com/content/bindt/insight/2018/00000060/00000004/art00003 (accessed on 22/11/2019) (cit. on p. 176).

[126] NVIDIA. (2nd Jul. 2013). CUDA Toolkit, NVIDIA Developer, [Online]. Available: https://developer.nvidia.com/cuda-toolkit (accessed on 15/02/2021) (cit. on p. 199).

[127] M. Björkman, N. Bergström and D. Kragic, 'Detecting, segmenting and tracking unknown objects using multi-label MRF inference', *Computer Vision and Image Understanding*, vol. 118, pp. 111–127, 1st Jan. 2014, ISSN: 1077-3142. DOI: 10.1016/j.cviu.2013.10.007 (cit. on p. 199).

[128] S. Hosseinzadeh, W. Jackson, D. Zhang, L. McDonald, G. Dobie, G. West and C. MacLeod, 'A Novel Centralization Method for Pipe Image Stitching', *IEEE Sensors Journal*, pp. 1–1, 2020. DOI: 10.1109/JSEN.2020.3031637 (cit. on pp. 202, 219).

[129] P. Hansen, H. Alismail, P. Rander and B. Browning, 'Pipe mapping with monocular fisheye imagery', in *2013 IEEE/RSJ International Conference on Intelligent Robots and Systems*, Nov. 2013, pp. 5180–5185. DOI: 10.1109/IROS.2013.6697105 (cit. on pp. 215, 220).